# Realizing the Applications of Nonlinear Encoding in MRI

A THESIS

SUBMITTED TO THE FACULTY OF THE GRADUATE SCHOOL

OF THE UNIVERSITY OF MINNESOTA

BY

Taylor William Froelich

IN PARTIAL FULFILLMENT OF THE REQUIREMENTS

FOR THE DEGREE OF

DOCTOR OF PHILOSOPHY

Advisor: Michael Garwood

October, 2023

*In loving memory of Lyra Belacqua Balboa, Ph.D. (ABD)*

*"All that is gold does not glitter,*
*Not all those who wander are lost;*
*The old that is strong does not wither,*
*Deep roots are not reached by the frost."*
*J.R.R. Tolkien*

# Abstract

Magnetic Resonance Imaging (MRI) possesses the unique ability to capture a wide range of physiological attributes with high spatial resolution. This flexibility has allowed researchers and medical professionals to not only study, but diagnose, an array of disease states and illnesses that previously required invasive means. However, despite its' tremendous advantages most of the world's population lacks ready access to this diagnostic tool, often having to travel great distances just to reach a scanner. MRI currently faces a severe inequity in both accessibility and utilization due to the high costs associated with obtaining, transporting, and maintaining a traditional scanner. Hence MRI is generally limited to the middle and upper classes in wealthier countries; creating a tremendous need for this diagnostic tool to be disseminated to regions with lower per capita income.

The primary goal of this work is to explore several approaches to the challenges of under-utilization and inaccessibility that the field of MRI faces. All of the techniques presented here have shown promise in improving the accessibility of MRI by either eliminating or replacing costly components without sacrificing on the diagnostic quality of the images. The first approach explored the feasibility of employing a low power, nonlinear gradient to perform slice selection and phase refocusing in a traditional spin-echo type sequence. Showing that it is not only possible to image in a permanent hyperboloidal gradient, but also observing the benefits to phase compensation and resolution, thus opening the door to exploring nonlinear encoding fields. The next approach sought to eliminate pulsed $B_0$ gradients in favor of radio-frequency (RF) based gradients. This approached utilized a nonlinear, spatially-varying RF field to encode information in a fast-spin echo sequence. As a proof of concept, only one dimension utilized this approach but the work can be easily extended to 2D. The final approach looked at the logistics of creating and implementing a portable MRI system. This required the design and installation of nonstandard hardware in all aspects of the imaging system; including a novel high temperature superconducting magnet, a multi-channel digital spectrometer, and a multi-channel gradient array capable of creating arbitrary encoding field.

# Contents

# List of Figures

# List of Tables

# Chapter 1

# Introduction

## 1.1 Motivation

Magnetic Resonance Imaging (MRI) is arguably one of the most powerful, non-invasive imaging modalities that has been developed. Its foundation lies in Nuclear Magnetic Resonance (NMR), the physical phenomena arising from interactions between certain atomic species and external magnetic fields. This unique foundation gives rise to the extreme versatility of MRI, allowing for applications ranging from material science to medicine.

This versatile modality enables medical professionals and researchers to non-destructively study the chemical properties of a living system. In fact, with minor variations to the radio-frequency (RF) pulse sequences specific information can be selected for without requiring damaging ionizing radiation, like conventional Computed Tomography (CT) and Positron Emission Tomography (PET). Not only does MRI improve upon the safety of CT/PET imaging techniques, but does so without sacrificing the diagnostic quality of the information acquired.

Recently MRI has experienced a period of exceptional growth, where researchers have continued to push the bounds of the field in pursuit of not only higher resolutions and stronger magnets, but also smaller, more portable systems. MRI is an extremely powerful tool diagnostic tool but it faces significant issues in accessibility due to the substantial financial burden to purchase, maintain, and operate such a device.

Several approaches have been proposed to address these inequities by focusing on the development of new technologies to reduce the overall cost and complexity of conventional imaging systems [1]–[4].

This pursuit of improving the accessibility and portability of MRI systems will be a central theme of the work presented herein. To accomplish this, first a brief discussion on the background necessary to understand MRI will be given, followed by a deeper dive into the more abstract approaches utilizing nonlinear encoding gradients, exotic RF pulse sequences, and finally an exploration of the non-conventional hardware created to produce images using the previously discussed techniques. This work does not replace traditional courses or books on the subject, so it is highly encouraged that the reader studies a brief selection of relevant publications [5]–[9].

## 1.2   Brief History of NMR and MRI

At its most fundamental level, NMR is a technique that exploits the interaction of certain atomic species with an externally applied magnetic field. This phenomenon only occurs when an atoms' nucleus has a nonzero nuclear spin arising from the presence of an odd number of protons and/or neutrons. There are many different isotopes that possess this quality, but the simplest and most abundant is $^1$H. When placed into an external magnet field, $^1$H will behave like a two-energy level system. This energy difference is due to the interaction between the magnetic moment of the nucleus and the external magnetic field, known as the Zeeman effect. In this configuration, the external magnetic field will begin to preferentially align the magnetic moments of $^1$H into one of the two energy states, either parallel or antiparallel, giving rise to a net magnetic moment. This system can then be manipulated through the application of RF pulses, causing the atoms to transition between the energy levels. This behavior was first observed in 1938 by Rabi et al., when he noted RF frequency-dependent energy absorption [10]. However, it wasn't until 1946 when two independent groups, led by Bloch and Purcell respectively, both directly detected the magnetic resonance after the application of a RF field [11]–[14].

At the time, the simplest approach to detect NMR spectra was through the use of continuous wave NMR. Due to hardware limitations, this approach utilized

a constant frequency RF field but swept the main polarizing field; resulting in the measured spectra as a function of resonance frequency. Later, Ernst and Anderson introduced a new approach that capitalized on the conjugate relationship between the time-domain and frequency-domain response of the spin system [15]. Their work utilized recent advances in RF technology to create short, pulsed RF pulses that were played out in the presence of a static polarizing field. The time-domain response of the system was measured and then used a Fourier transform to yield the frequency-domain spectra. Consequently, the complete spectrum could be acquired with only a small number of RF pulses; thus, greatly improving the speed and sensitivity of NMR compared to the previous continuous wave approaches.

Further expanding off of the work performed by Ernst and Anderson, Lauterbur was the first to realize the potential in utilizing these NMR techniques to generate images [16], [17]. In these pivotal works Lauterbur illustrated that an RF pulse, combined with a linear field gradient, allowed for the encoding of unique spatial information; thus, the foundation of MRI was established. Notably, Lauterbur discovered that the degree of localization was independent of the RF frequency, implying that the spatial resolution of the method was unaffected by the RF wavelength. Shortly thereafter, Hoult demonstrated the necessity of refocusing spins prior to signal detection in order to obtain high-quality images; thus creating the spin echo and setting the stage for modern MRI [18].

# Chapter 2

# Background

## 2.1 Classical Description of Magnetic Resonance

### 2.1.1 Qualitative Overview

This section will provide a general overview of classical magnetic resonance prior to diving into more complex concepts. Like most fields of science, MR continuously builds off of early concepts and techniques. The hope is by providing a brief overview of this foundation more nuanced approaches and techniques will be easier to understand when described in the rest of the work.

To begin, consider an object that is placed in an external magnetic field. This field will begin to align the magnetic moments within the sample such that a net magnetization is formed along the direction of the external field. The sample's effective magnetic moment is the sum of many smaller moments throughout the object, giving rise to the net alignment that can be observed. As the magnetic moment is the sum of these smaller components throughout the sample, the quantity of interest is the magnetization or the amount of magnetic moment per unit volume.

In order to make the magnetization detectable, it must be tipped away from the polarizing field; that is to say, having some component of its magnetization along the transverse plane. Initially the magnetization vector is aligned with the polarizing field, but as it begins to tip it can be viewed as a three-dimensional vector, with one component still parallel to the polarizing field and two additional components

orthogonal along the transverse plane. The magnitude of the transverse components is determined by how far the magnetization was tipped away from the polarizing field; with the angle between the magnetization and the polarizing field called the flip angle.

To achieve this tipping a radio-frequency pulse (RF) is played out through a resonant circuit transmitter, or RF coil, that creates a component of magnetic field that is perpendicular to the polarizing field. As the magnetization begins to tip away, it experiences a net torque causing it to precess around the external field. Interactions with neighboring spins will begin to cause the magnetization to slowly return to alignment with the polarizing field; thus, forming the process of relaxation. This precession of the magnetic moment gives rise to an oscillating magnetic field that can be easily inductively detected via Faraday's law [19]. To inductively detect this oscillation, a resonant circuit that is tuned to the frequency of precession acts as a receiver. This transmitter and receiver pair are typically the same circuit forming the foundation of the RF coils employed in MRI.

With the magnetization tipped away from the polarizing field, unique spatial information can be encoded through the use of linear field gradients, commonly referred to as gradients, as applied across the sample. The net result is the frequency of precession varies linearly as a function of position. The different frequencies can then be resolved computationally through the use of a Fourier transform with the appropriate number of encoded dimensions.

## 2.1.2  Origin of NMR Signal

Herein we expand upon the preceding qualitative overview and provide further detail on the fundamental physics that give rise to the signal measured in NMR. As previously stated, the fundamental quantity of interest is time evolution of the net magnetization. The net magnetization, $\mathbf{M}$, arises from the vector sum of all atomic nuclei within the object that possess a magnetic moment $\boldsymbol{\mu}$. However, only atomic nuclei with an odd number of protons and/or neutrons, and therefore a nonzero total angular momentum, will have a magnetic moment. This phenomenon arises from the intrinsic quantum property of nuclear spin, $\mathbf{S}$; however, this work is confined to a

classical description of isolated spin-$\frac{1}{2}$ nuclei like hydrogen, without further description of their quantum mechanics.

Starting from this postulate, a derivation of how nuclear spin gives rise to a nonzero nuclear magnetic dipole will be performed. To begin, it has been shown that the torque $\boldsymbol{\tau}$ on a magnetic dipole $\mathbf{m}$ in a uniform magnetic field $\mathbf{B}$ is described by the following equation [19],

$$\boldsymbol{\tau} = \mathbf{m} \times \mathbf{B}. \tag{2.1}$$

Assuming that a proton is a uniformly charged, rotating sphere, the magnetic dipole moment can be easily calculated as

$$\mathbf{m} = \frac{1}{2} \int_{V'} \mathbf{r}' \times \mathbf{J}(\mathbf{r}') \mathrm{d}^3 r', \tag{2.2}$$

where the primed coordinates correspond to the integration over the volume for a given current density, $\mathbf{J}$. Now consider an infinitesimal volume, $\mathrm{d}V'$, this equation simplifies to

$$\mathrm{d}\mathbf{m} = \frac{1}{2} \mathbf{r}' \times \mathbf{J} \mathrm{d}V'. \tag{2.3}$$

Now we can express the infinitesimal charge, $\mathrm{d}q$, and its contribution, $\mathrm{d}\mathbf{m}$, in terms of spherical coordinates. To begin, the charge of the proton is denoted as $e$, with its radius given by $R$, and having a rotational frequency of $\omega$,

$$\mathrm{d}q = \rho \mathrm{d}V' \qquad \text{(infinitesimal charge)} \tag{2.4}$$

$$\rho = \frac{e}{(\frac{4}{3}\pi R^3)} \qquad \text{(charge density)} \tag{2.5}$$

$$\mathrm{d}V = r^2 \sin(\theta) dr d\theta d\phi \qquad \text{(volume element)} \tag{2.6}$$

For a moving charge, the current density is given by

$$\mathbf{J} = \rho \boldsymbol{\omega} \times \mathbf{r}' \tag{2.7}$$

with $\boldsymbol{\omega}$ corresponding to the angular velocity of the rotating sphere. For simplicity, the direction of the angular velocity is chosen to be along the $\hat{z}$. Substituting this back into Eq. 2.3 and evaluating the double cross product gives a simpler equation for $\mathrm{d}\mathbf{m}$

$$\mathrm{d}\mathbf{m} = \frac{\rho}{2} r^2 \boldsymbol{\omega} - (\mathbf{r}' \cdot \boldsymbol{\omega}) \mathbf{r}' \mathrm{d}V' \tag{2.8}$$

with the position $\mathbf{r}'$ for a charge element at given radius, $r$, a polar angle of $\theta$, and an azimuthal angle of $\phi$ given by

$$\mathbf{r}' = r \sin\theta \cos\phi \hat{x} + r \sin\theta \sin\phi \hat{y} + r \cos\theta \hat{z}. \tag{2.9}$$

Given the previous equations, it is possible to integrate $\mathrm{d}\mathbf{m}$ over the volume $V'$. However, when integrating $\phi$ from 0 to $2\pi$, both $\hat{x}$ and $\hat{y}$ terms integrate to 0 due to the periodicity of sin and cos. After integrating over $\phi$ the equation becomes

$$\mathbf{m} = \pi \rho \omega \int_0^R \int_0^\pi r^4 (1 - \cos^2\theta) \sin\theta \, dr d\theta \hat{z}. \tag{2.10}$$

After evaluating the integrals, the magnetic dipole moment is given by

$$\mathbf{m} = \pi \rho \omega \frac{4R^5}{15} \hat{z}. \tag{2.11}$$

This equation can then be further simplified by substituting in Eq. 2.5,

$$\mathbf{m} = \frac{e}{5} \omega R^2 \hat{z}. \tag{2.12}$$

With this equation, it can be shown that the magnetic moment is directly proportional to the spin angular momentum of the proton. To begin, the dipole moment will be written in terms of its moment of inertia, $I = \frac{2}{5} m_p R^2$ [20],

$$\mathbf{m} = \frac{e}{2m_p} I\omega\hat{z} \tag{2.13}$$

$$\mathbf{m} = \frac{e}{2m_p}\mathbf{L} \tag{2.14}$$

$$\mathbf{L} = I\omega\hat{z}. \tag{2.15}$$

From here, it is clear that the magnetic moment is directly proportional to the spin angular momentum $\mathbf{L}$ with a proportionality constant of

$$\gamma = \frac{e}{2m_p}, \tag{2.16}$$

this proportionality constant is called the gyromagnetic ratio and typically labeled as $\gamma$. In practice, the expected value from Eq. 2.16 does not agree with the measured value and a scaling factor must be included. This falls out from the quantum mechanical nature of a proton. To account for this discrepancy, a scaling factor called the g-factor is introduced, thus $\gamma$ becomes

$$\gamma = g\frac{e}{2m_p}. \tag{2.17}$$

### 2.1.3  Equations of Motion

As previously stated, the time varying magnetization is the quantity of interest that gives rise to the detected signal in NMR. The physicist Felix Bloch was the first to present these phenomenological equations describing the macroscopic evolution of the bulk magnetization in both space and time. To derive these equations, we start with the rate of change of angular momentum,

$$\frac{d\mathbf{L}}{dt} = \boldsymbol{\tau}. \tag{2.18}$$

By substituting in Eq. 2.1 on the right hand side of the equation, the rate of change of angular moment is related to the magnetization and applied magnetic field by,

$$\frac{d\mathbf{L}}{dt} = \mathbf{m} \times \mathbf{B}. \tag{2.19}$$

Using Eq. 2.14 and Eq. 2.16, this equation can be further simplified to

$$\frac{d\mathbf{m}}{dt} = \gamma(\mathbf{m} \times \mathbf{B}). \tag{2.20}$$

Thus, the Bloch equation for a dipole precessing clockwise about $\mathbf{B}$, with an angular frequency is given by

$$\omega_L = \gamma B. \tag{2.21}$$

If the field in Eq. 2.20 is the main polarizing field, the angular frequency is described as

$$\omega_L = \gamma B_0. \tag{2.22}$$

This angular frequency is referred to as the Larmor frequency. However, it is important to note that the precession can occur about other applied fields. For example, if the effective field arises from an applied RF pulse, the angular frequency is called the Rabi frequency, given as

$$\omega_R = \gamma|\vec{B_1}|. \tag{2.23}$$

To fully account for the experimental behavior of the magnetization, relaxation effects must be introduced into these equations. Realizing this shortcoming, Bloch proposed to include exponential relaxation with two different characteristic times [12]. The first, $T_1$, denotes relaxation along the polarizing magnetic field; while the other, $T_2$, denotes relaxation orthogonal to the polarizing field. Thus the full macroscopic Bloch equations are

$$\frac{d}{dt}\begin{bmatrix} m_x \\ m_y \\ m_z \end{bmatrix} = \begin{bmatrix} -\frac{1}{T_2} & \gamma B_z & -\gamma B_y \\ -\gamma B_z & -\frac{1}{T_2} & \gamma B_x \\ \gamma B_y & -\gamma B_x & -\frac{1}{T_1} \end{bmatrix} \begin{bmatrix} m_x \\ m_y \\ m_z \end{bmatrix} + \begin{bmatrix} 0 \\ 0 \\ \frac{M_0}{T_1} \end{bmatrix} \tag{2.24}$$

A large polarizing magnetic field, $B_0$, generates longitudinal magnetization, $M_0$, which for any arbitrary nuclei is defined as

$$M_0 = (\gamma\hbar)^2 \frac{Nm_s(m_s+1)B_0}{3k_\mathrm{b}T}. \tag{2.25}$$

where $N$ corresponds to the number of spins per unit volume, $m_s$ is the spin quantum number, $k_\mathrm{b}$ is the Boltzman constant, $T$ is the temperature in Kelvins, and $\hbar$ is the reduced Planck's constant.

The bulk magnetization mentioned earlier, or the sum of the dipole moments per unit volume, is defined as

$$\mathbf{M} = \frac{1}{V}\sum_V \mathbf{m}. \tag{2.26}$$

This represents all of the spins that are aligned parallel to the polarizing field thus contributing to the net magnetization of the sample. When the magnetization is displaced from equilibrium by an external RF pulse, a component of the magnetization is placed perpendicular to $B_0$, along the transverse plane, i.e. $M_{xy} = M_x + iM_y$. It will begin to precess around $B_0$ at the Larmor frequency that can then be detected using an RF coil tuned to that Larmor frequency.

## 2.1.4 Transformation from Laboratory Frame to Rotating Frame

Often it is more useful to look at the spin dynamics from different frames of reference that have unique properties to simplify the physics. The most intuitive one corresponding to a frame that rotates with the same angular frequency as the Larmor frequency. To perform this transformation into a rotating frame, the previous equations describing the spin dynamics need to be modified to account for this constant frequency. For magnetic resonance specifically, an RF field oscillating at frequency $\omega$ is applied, with either linear or circular polarization, orthogonal to the field $B_0$. For simplicity consider just a linearly polarized RF field, defined in the laboratory frame as

$$\mathbf{B}_1 = B_1 \cos\omega(t)\hat{x} \tag{2.27}$$
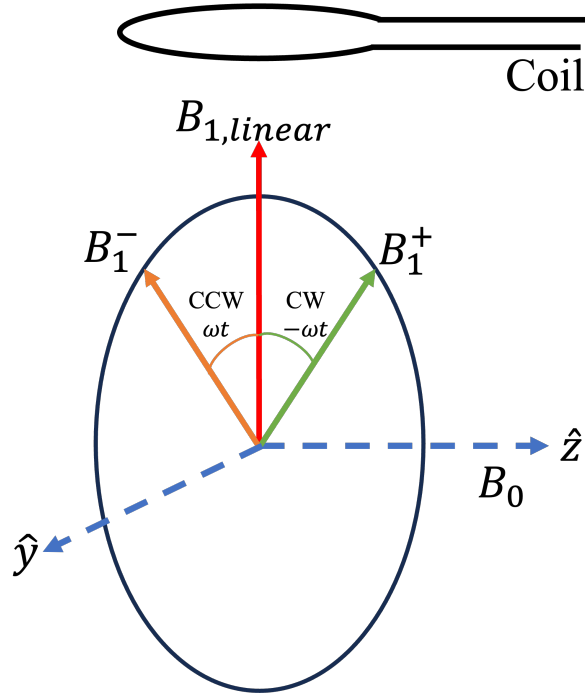
**Fig. 2.1.** $B_1$, Linear and Rotating RF Field. The decomposition of a linearly polarized field produced by a single transmit coil into two counter-rotating fields. The two fields rotate at the same frequency about the $\hat{z}$ axis albeit in different directions, with CW corresponding to clockwise and CCW being count-clockwise rotation.

The $B_1$ field from a linearly polarized transmit coil can be viewed as being composed of two counter-rotating fields, one that precesses along the same direction as the atomic nuclei's spin, denoted as $B_1^+$, and another along the opposite direction, denoted as $B_1^-$, Fig. 2.1. The $B_1^+$ field is of primary interest as it's used to excite spin, whereas $B_1^-$ is of interest when receiving signal. Now we can rewrite Eq. 2.27 as a superposition of these two counter-rotating magnetic fields, both at frequency $\omega$,

$$\mathbf{B}_1 = \frac{B_1}{2}\Big(\big(\cos(\omega t)\,\hat{x} + \sin(\omega t)\,\hat{y}\big) + \big(\cos(\omega t)\,\hat{x} - \sin(\omega t)\,\hat{y}\big)\Big). \tag{2.28}$$

By changing the frame of reference to a rotating frame, thus rotating about the $z$-axis with the clockwise component of $\mathbf{B_1}$ in Eq. 2.28, we determine

$$\mathbf{B}_1 = \frac{B_1}{2}\left((1 + \cos(2\omega t))\hat{x}' + \sin(2\omega t)\hat{y}'\right) \qquad (2.29)$$

The angular velocity of the rotating frame corresponds to

$$\mathbf{\Omega} = -\omega\hat{z}. \qquad (2.30)$$

When changing from a stationary frame to a rotating frame of reference with angular velocity $\mathbf{\Omega}$, ignoring relaxation, the magnetization can be expressed as [20]

$$\left(\frac{d\mathbf{M}}{dt}\right)_{rotating} = \left(\frac{d\mathbf{M}}{dt}\right)_{stationary} + \mathbf{M} \times \mathbf{\Omega} \qquad (2.31)$$

$$\left(\frac{d\mathbf{M}}{dt}\right)_{rotating} = \gamma\mathbf{M} \times \mathbf{B} + \mathbf{M} \times \mathbf{\Omega} \qquad (2.32)$$

$$\left(\frac{d\mathbf{M}}{dt}\right)_{rotating} = \gamma\mathbf{M} \times (\mathbf{B} + \frac{\mathbf{\Omega}}{\gamma}) \qquad (2.33)$$

Thus in the presence of both $B_1$ and $B_0$, this equation simplifies down to

$$\left(\frac{d\mathbf{M}}{dt}\right)_{rotating} = \gamma\mathbf{M} \times \frac{B_1}{2}\left((1 + \cos(2\omega t))\hat{x}' + \sin(2\omega t)\hat{y}' + \left(B_0 - \frac{\omega}{\gamma}\right)\hat{z}'\right). \qquad (2.34)$$

This equation can be further simplified by selecting the frequency $\omega$ of the RF field such that it equals the Larmor frequency, the term along $\hat{z}'$ cancels out and is often referred to as being on-resonance of the spins. This follows from $\mathbf{\Omega}$ acting as a fictitious field, only appearing in the rotating frame and affecting the magnetization as a function of time, $t$. It is also important to note that the periodic terms in this equation average to 0, due to the rapid oscillations that occur at $2\omega$. Incorporating these observations, Eq. 2.34 becomes

$$\left(\frac{d\mathbf{M}}{dt}\right)_{rotating} = \gamma\mathbf{M} \times \frac{B_1}{2}\hat{x}'. \qquad (2.35)$$

From this equation, one can see that the amplitude of the applied RF field in the rotating frame is half the amplitude of the applied field, i.e. $\frac{B_1}{2}\hat{x}'$. This is a result

of decomposing the original linear field into its' corresponding counter-rotating fields, with only the $B_1^+$ component rotating clockwise at the Larmor frequency significantly affecting the motion of the magnetization. Thus the other half of the amplitude is lost to the other rotating component, $B_1^-$.

As written Eq. 2.35 is valid only for on-resonance spins, but can generalized for any off-resonance, i.e. $\omega \neq \omega_L$, when expressed as

$$\left(\frac{d\mathbf{M}}{dt}\right)_{rotating} = \gamma \mathbf{M} \times \left(\frac{B_1}{2}\hat{x}' + \frac{(\omega_L - \omega)}{\gamma}\hat{z}'\right). \tag{2.36}$$

Stepping back, it is clear that in the rotating frame the magnetization precesses about the applied field. Whereas, in the laboratory frame the magnetization rotates away from the main polarizing field, while also precessing around it. This rotating and precessing that occurs simultaneously in the laboratory frame often obscures the spin dynamics that occur over time, especially when compared to the rotating frame. Thus for mathematical simplicity, the rotating frame is most often discussed.

## 2.2 Radiofrequency, AM and FM Pulses

### 2.2.1 Amplitude-Modulated

As previously discussed, in the rotating frame of reference, an on-resonance magnetization will rotate around an applied $B_1$ field. In the derivation of Eq. 2.35, a fixed amplitude pulse was assumed, often referred to as a hard pulse. However, this derivation still holds true for more complex, time-varying fields if the rate of the amplitude-modulation is slow compared to the Larmor frequency. With this assumption, the class of purely amplitude-modulated (AM) RF pulses was born. For simple AM pulses with a pulse duration of $T_{\mathrm{P}}$, the flip angle, or the total angle precessed about $B_1$ in the rotating frame, can be determined by

$$\theta = \gamma \int_0^{T_{\mathrm{P}}} B_1(t)dt. \tag{2.37}$$

This equation is valid for any angle $\geq 0$ and scales with the area of the AM pulse. In practice the two most discussed flip angles correspond to 90° and 180°. Assuming

that the magnetization is initially aligned along the main polarizing field, a 90° flip will tip the on-resonance magnetization onto the transverse plane. However, in the case of a 180° flip, the magnetization undergoes an inversion, effectively flipping the direction of the magnetization. This behavior can be useful after the magnetization has already been tipped away from the polarizing field as it would act as a refocusing pulse. Any off-resonance magnetization that has de-phased, due to experimental imperfections, can be refocused before signal acquisition. This refocusing is the foundation of a spin echo type sequence that effectively nullifies the effect of various inhomogeneities.

Some common AM pulses that are used to excite a band of frequencies in MRI are hard, sinc, and Gaussian pulses. Not only does each of these pulses have a unique amplitude-modulation function but the resulting transverse magnetization varies significantly between the pulses. These variations are shown in Fig. 2.2 as the transverse magnetization is plotted as a function of off-resonance frequency. From the figure, it is clear that the resulting transverse magnetization is different for each pulse, with the hard pulse producing large oscillations outside of the desired frequency band and the gaussian pulse performing the best. However, in practice sinc pulses are typically filtered using either a gaussian or a Hanning window [5] to minimize the oscillations observed in the standard sinc.
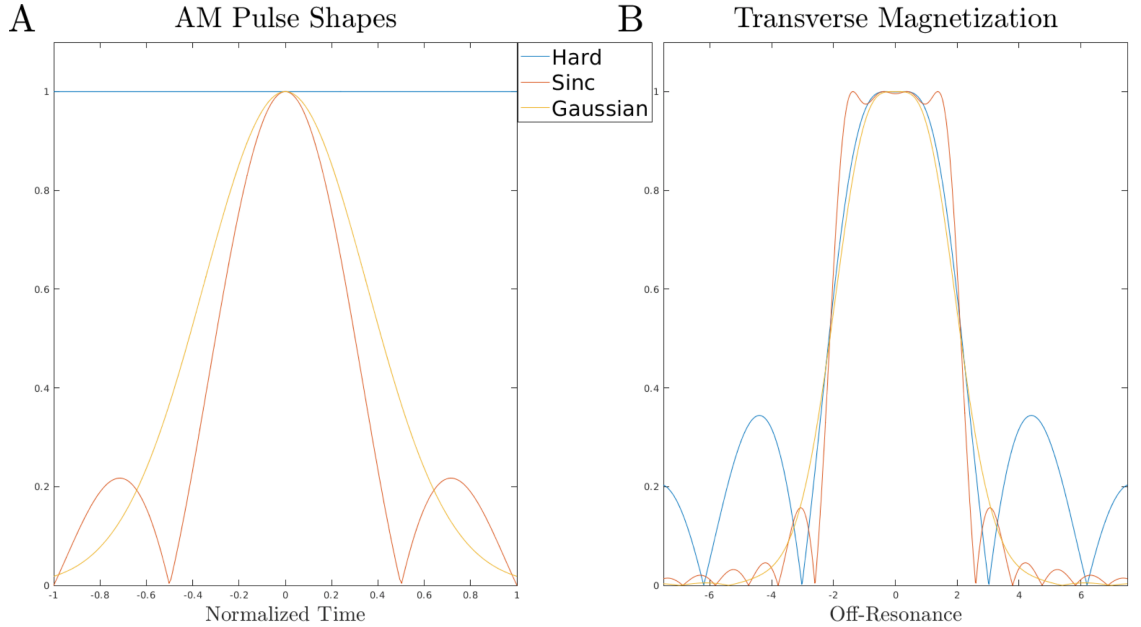
**Fig. 2.2.** Examples of three common amplitude-modulated pulses. A) The amplitude-modulation function is shown for a hard pulse, a gaussian pulse, and a sinc pulse as a function of normalized time. B) The resulting transverse magnetization as a function of off-resonance for each pulse. The peak power was selected such that each pulse produced a 90° excitation on-resonance. These results were simulated by numerically evaluating the previously derived Bloch equations.

A useful parameter that relates the duration of a pulse, $T_\mathrm{P}$, to its corresponding frequency bandwidth, $BW$, is the time-bandwidth product, $R = BW \cdot T_\mathrm{P}$. For purely amplitude-modulated pulses, $R$ is nearly constant, only slightly varying with changes to peak power, and therefore flip angle. As a consequence of this, to either increase or decrease the bandwidth of excitation a pulses' duration must be shortened or lengthened, respectively. However, from Eq. 2.37 for a fixed pulse shape, a shorter pulse requires more peak power to maintain the same flip angle.

## 2.2.2 Frequency-Modulated

As technology continued to evolve the ability to modulate the frequency of a pulse in time became possible, thus frequency-modulated (FM) pulses were born. FM pulses are unique compared to traditional AM pulses, in that rather than being

15

applied only on-resonance, the instantaneous frequency of the pulse is swept as a function of time. To accurately discuss this unique behavior a brief analysis of FM pulses will be presented. Using the notation put forth previously, the time-dependence of the frequency-modulation is given by $F_2(t)$, where as the amplitude-modulation is $F_1(t)$ [21]. Typically, the frequency- and amplitude-modulation functions are normalized such that $0 \leq F_1 \leq 1$ and $-1 \leq F_2 \leq 1$. Using this notation, a FM pulse is defined as

$$\omega_1(t) = \omega_1^{\mathrm{max}} F_1(t) \tag{2.38}$$

$$\Delta\omega(t) = AF_2(t) - \omega_c \tag{2.39}$$

where $\omega_1^{\mathrm{max}}$ corresponds to the peak amplitude of the pulse and $A$ corresponds to amplitude of the frequency modulation.

To better understand the behavior of frequency modulated pulses, it is often more intuitive to change references frames to one that is rotating at the same instantaneous frequency of the pulse, called the FM frame and denoted by $(x', y', z')$. Using this new reference frame, not only does the behavior of an adiabatic full passage pulse (AFP) become easier to describe, but this reference frame will be crucial for later discussions on RF encoding.

Suppose all of the magnetization is initially aligned along the $(z')$-axis, Fig. 2.3. As FM of the pulse is played out, the frequency sweep function initially starts far off resonance with a small $\omega_1$ along the $x'$ axis ($\Delta\omega(t) >> \omega_1^{\mathrm{max}}(t)$) and $\Delta\omega$ dominates along the $(z')$-axis. As the pulse evolves in time the effective $B_1$, denoted by $\boldsymbol{\omega}_{eff}(t)$, begins to tip away from the $z'$ axis until the $\Delta\omega$ component is zero, corresponding to the on-resonance condition. Eventually the frequency sweep will continue far below resonance, thus performing an inversion. The time-dependent off-axis angle is denoted by

$$\alpha(t) = \arctan\left(\frac{\omega_1^{\mathrm{max}} F_1(t)}{\Delta\omega(t)}\right) \tag{2.40}$$

Changing reference frames again to the $\boldsymbol{\omega}_{eff}(t)$ frame of reference, the effective

16

field is placed along the $z$-axis of the frame denoted by $(x'', y'', z'')$, Fig. 2.3. Now there are only two fields affecting the magnetization: the effective field and a fictitious field, $\frac{d}{dt}\alpha(t)$, shown in Fig. 2.3b. An adiabatic inversion is said to take place if the following condition is met

$$\gamma|\boldsymbol{\omega}_{eff}(t)| >> \left|\frac{d}{dt}\alpha(t)\right|. \tag{2.41}$$

In this equation the instantaneous angular velocity, $\frac{d}{dt}\alpha(t)$, must be significantly smaller than the sweep rate of $\boldsymbol{\omega}_{eff}(t)$. If this is true, then at all times the magnetization will maintain its' initial orientation relative to the effective field and is said to be adiabatic [21].
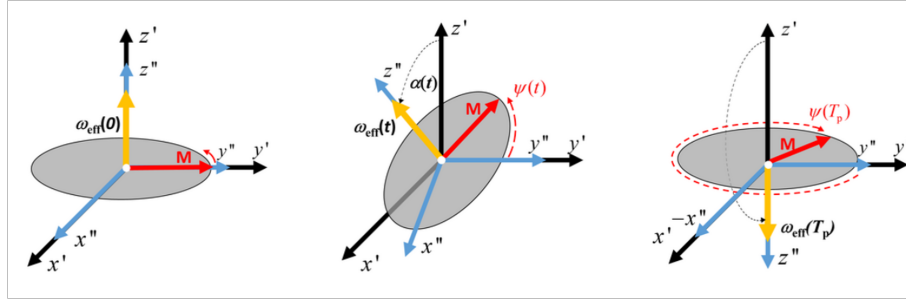


**Fig. 2.3.** Diagram demonstrating how magnetization follows the effective field of a frequency swept pulse, provided the adiabatic condition is met. A depiction of the trajectory of an arbitrary $\mathbf{M}$ and its phase accumulation throughout an AFP in a first $(x', y', z')$ and second $(x'', y'', z'')$ rotating frame of reference.

Adiabatic pulses are a unique class of pulses that are insensitive to variations in the magnitude of the peak $\omega_1^{max}$ amplitude when the adiabatic condition is met. In practice, this insensitivity stems from their ability to still perform an inversion, above a certain peak $\omega_1^{max}$ threshold, despite large variations in the range of peak pulse powers, as in the case of a surface coil. When the pulse is truncated such that the frequency offset $\Delta\omega = 0$, the pulse is referred to as an adiabatic half passage and can be used to perform excitations.

Some of the most common frequency-swept pulses in MRI are the hyperbolic secant, or HSn, pulses [21]–[23]. The amplitude- and frequency- modulation functions for HSn pulses are given by

$$F_1(\tau) = \text{sech}(\beta\tau^n) \tag{2.42}$$

$$F_2(t) = \int F_1(t)^2 d\tau \tag{2.43}$$

where $\beta$ is a dimensionless truncation factor, $\tau\epsilon[-1, 1]$ is a normalized time coordinate, and $n$ is a parameter that controls the flatness of the AM function. Typically, $\beta = \text{asech}(.01)$, which truncates the pulse at 1% of the peak power. The amplitude- and frequency-modulation functions for $n = 1$, 4, and 8 are shown in Fig. 2.4, as well as the resulting $M_z$ when the pulses are driven adiabatically for inversion. As $n$ is increased, a lower peak power is sufficient to achieve adiabaticity at the expense of a less smooth inversion profile as a function of off-resonance.
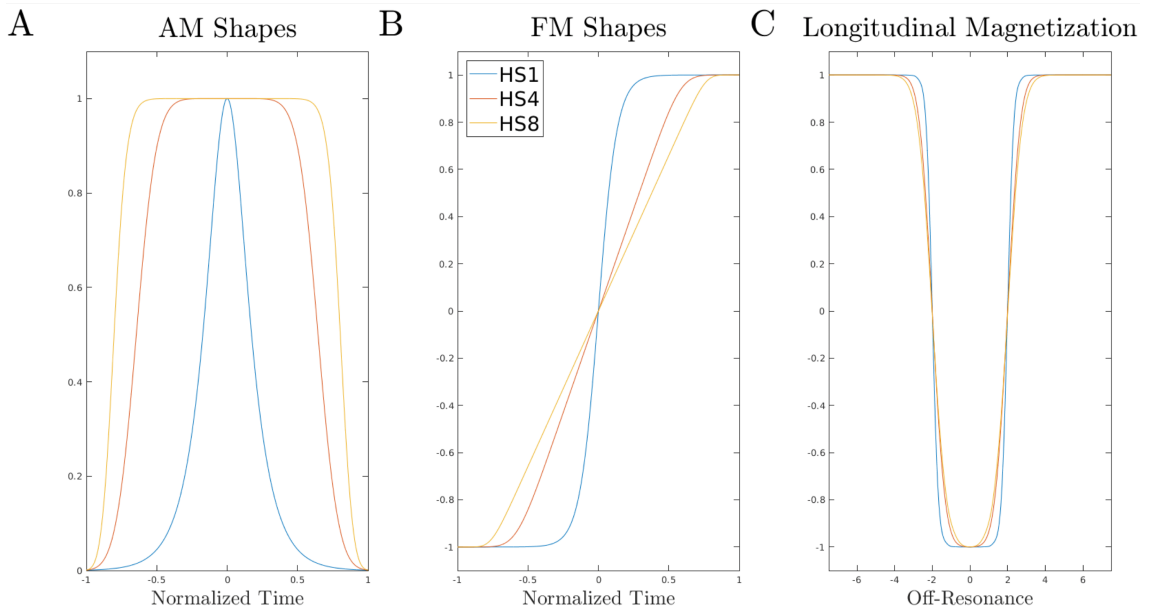


**Fig. 2.4.** Three example FM pulses, depicting a) the pulse amplitudes as functions of time, b) the pulse frequency modulations as a function of time, and c) the resultant longitudinal magnetization from each pulse when driven adiabatically. All pulses were simulated with the same bandwidth and duration.

### 2.2.3  Specific Absorption Rate (SAR)

With the advances presented in $B_1$ encoding techniques, a very important safety metric is the specific absorption rate (SAR). SAR is the measure of the amount of heating induced in a subject due to the applied RF pulses, which is of concern in $B_1$ encoding techniques. The units of local SAR are Watts per Kilogram for a 10-g volume of tissue, or more generally, energy per time, per mass. The SAR induced by an RF pulse is proportional to the average power of the pulse, which can be calculated by

$$\text{SAR} \propto \int_0^{T_\text{P}} |B_1(t)|^2 dt. \tag{2.44}$$

This equation provides a good estimate of the total power delivered during an RF pulse, however, it lacks several key properties that must be taken into account to have an accurate determination of SAR. For example, most commercially available finite-element based E&M software packages require not only a very accurate model of the coil, but also a realistic human equivalent phantom. The result is a 3D distribution of the SAR at a specific frequency, i.e. field strength, throughout the human equivalent phantom. This information is essential to ensure the safety of not only the RF coil used but also the imaging method as only the RF power delivered during a sequence is measured over the duration of a procedure.

### 2.2.4  Multi-dimensional RF Pulses

In contrast to the previous section, it is often desirable to tailor the excitation region to a 2D profile. To accomplish this the resulting transverse magnetization needs to be related to the initial RF waveform. Considering the simple 1D examples from Fig. 2.2, it is clear that the resulting excitation profile simply resembles its own respective Fourier transform of the initial RF pulse [5]. This result falls out from the fact that the magnetization is governed by RF frequencies near resonance; thus the response of the magnetization for a fixed frequency offset behaves according to the corresponding frequency content of the RF pulse. This idea was first proposed and demonstrated by Pauly et al., where they described this phenomenon using the

$k$-space formalism, assuming the flip angle is small [24]. The following will be a brief overview of Pauly et al.'s derivation but we also invite the reader to peruse the original publication [24].

In this limit, the longitudinal magnetization $M_z$ is assumed to be static, i.e.

$$M_z \approx M_0. \tag{2.45}$$

With this assumption, the equations of motion for the transverse magnetization simplifies down to

$$\frac{dM_{xy}}{dt} = i\gamma \mathbf{G}(t) \cdot \mathbf{x} M_{xy} + i\gamma B_1(t) M_0, \tag{2.46}$$

where $\mathbf{G}(t)$ are time varying gradient waveforms and $B_1$ is the applied RF field. Now the resulting transverse magnetization, $M_{xy}(\mathbf{x})$ can be easily solved for giving the following equation

$$M_{xy}(\mathbf{x}) = i\gamma M_0 \int_0^{T_\mathrm{P}} B_1(t) e^{-i\gamma \mathbf{x} \cdot \int_t^{T_\mathrm{P}} \mathbf{G}(s) ds} dt. \tag{2.47}$$

Defining a spatial frequency variable as

$$\mathbf{k}(t) = -\gamma \int_t^{T_\mathrm{P}} \mathbf{G}(s) ds, \tag{2.48}$$

and plugging this result into the previous equation gives us

$$M_{xy}(\mathbf{x}) = i\gamma M_0(\mathbf{x}) \int_0^{T_\mathrm{P}} B_1(t) e^{-i\mathbf{x} \cdot \mathbf{k}(t)} dt. \tag{2.49}$$

To further simplify this equation, suppose a weighting factor is defined along a given k-space trajectory $(S(\mathbf{k}))$ as

$$W(\mathbf{k}) = \frac{B_1}{|\gamma \mathbf{G}(t)|}, \tag{2.50}$$

then the excitation profile, $M_{xy}$, of the 2D pulse is simply given by

$$M_{xy}(\mathbf{x}) = i\gamma M_0(\mathbf{x}) \int_{\mathbf{k}} W(\mathbf{k}) S(\mathbf{k}) e^{i\mathbf{x} \cdot \mathbf{k}} d\mathbf{k}. \tag{2.51}$$

Therefore, from this result it is clear that the magnetization is just the Fourier transform of its respective weighted k-space trajectory, where the weighting is proportional to the $B_1$ field and inversely proportion to the rate at which k-space is traversed.

## 2.3    Acquisition and Image Encoding Methods

### 2.3.1    Signal Detection

It has been previously shown that there are various ways to produce transverse magnetization following an RF pulse, either in 1D or 2D. In the laboratory frame, the transverse magnetization will precess about the $B_0$ field while slowly relaxing. As the magnetization precesses, it will exert an electromotive force on the locally placed RF coil via Faraday's law

$$emf = -\frac{d}{dt}\Phi_M(t). \tag{2.52}$$

In this equation, the quantity of interest is the rate of change of the magnetic flux as expressed as

$$\Phi_M(t) = \int_S \mathbf{B}(\mathbf{r}, t) \cdot \hat{n} dS, \tag{2.53}$$

where the integral is performed over the surface $S$ defined by the RF coil. The derivation is outside of the scope of this work but a body of works are recommended for further explanation if desired [5], [19]. Using the results presented in these works, a simple equation for the time-dependent flux through a loop of wire is defined as

$$\Phi_M(t) = \frac{\mu_0}{4\pi} \int_V \mathbf{M}(\mathbf{r}') \cdot \beta_{receive}(\mathbf{r}') d^3 r'. \tag{2.54}$$

With $\beta_{receive}(\mathbf{r}') = \frac{\mathbf{B}_{receive}}{I}$, and $\mathbf{B}_{receive}(\mathbf{r}')$ corresponding to the magnetic field at a point $\mathbf{r}'$ from an induced current, $I$, the actual $emf$ measured is then

$$emf = -\frac{d}{dt} \int_V \mathbf{M}(\mathbf{r}', t) \cdot \beta_{receive}(\mathbf{r}') d^3 r'. \tag{2.55}$$

As only the transverse magnetization precesses, the dominant time-dependence in Eq. 2.55 stems from the precessional motion along the transverse place. It is important to note that, as the precession occurs at the Larmor frequency, the signal intensity is proportional to the Larmor frequency. Therefore, at larger magnetic fields a larger signal amplitude is received in the RF coil. Further, the detected quantity is not just the magnetization of the sample, but corresponds to the product the magnetization with the receive field.

## 2.3.2   Image Encoding, Standard Gradients

Now that the transverse magnetization is successfully detected and recorded, several methods will be presented that encode unique spatial information within the transverse magnetization. This will be either through the application of traditional pulsed $B_0$ gradients or $B_1$ based gradients. Both methods focus on modulating the resulting phase of the transverse magnetization and can be discussed using a similar formalism.

To begin, suppose that the transverse component of the receive field is denoted by $\beta_{xy}$. The measured signal in the laboratory frame is then given by

$$S_{\text{laboratory}}(t) = \int_V \beta_{xy}(\mathbf{r}) M_{xy}(\mathbf{r}, t) e^{-i\omega_c t} d\mathbf{r}, \qquad (2.56)$$

with the integral being performed over the 3D excited magnetization [5]. In practice, the acquired signal is demodulated by removing the $e^{-i\omega_c t}$ component from the equation. This corresponds to a transformation to a demodulated reference frame with the acquired signal now corresponding to

$$S_{\text{demodulated}}(t) = \int_V \beta_{xy}(\mathbf{r}) M_{xy}(\mathbf{r}, t) d\mathbf{r}. \qquad (2.57)$$

From this equation, the signal is the product of the receive field, $\beta_{xy}(\mathbf{r})$, and the magnetization, $M_{xy}(\mathbf{r}, t)$. This receive field plays a crucial role in parallel imaging techniques where the field itself can be used to encode unique information that can be leveraged during reconstruction [25], [26]. Under the framework presented here, the time-dependence of the magnetization $M_{xy}(\mathbf{r}, t)$ is contained only in the phase of

the magnetization. The phase is modulated using gradients (either pulsed $B_0$ or RF based) to impart a spatially dependent resonance offset, in turn yielding additional precession. The net result is a spatially varying dispersion of off-resonances that creates a unique phase across the object as a function of time. In conventional MRI, this phase is typically encoded linearly in space; however, nonlinear encoding schemes exist that provide some added advantages. These different nonlinear schemes will be discussed later; though the mathematical framework developed for traditional linear encoding provides a good foundation to help analyze the nonlinear methodologies.

For simplicity, consider purely linear pulsed $B_0$ gradients. The polarizing field can be expressed as $B_0(\mathbf{x}) = B_0 + \mathbf{G} \cdot \mathbf{x}$, with the resulting phase term given by $e^{-i\gamma \int_0^t \mathbf{G}(s) \cdot \mathbf{r} ds}$. The signal equation can then be expressed as

$$S(t) = \int_V M_{xy}(\mathbf{r}) e^{-i\mathbf{k}(t) \cdot \mathbf{r}} d\mathbf{r}, \qquad (2.58)$$

where

$$\mathbf{k}(t) = \gamma \int_0^t \mathbf{G}(s) ds. \qquad (2.59)$$

It is important to note that the k-space trajectory, $\mathbf{k}$, in this equation is different than the one previously presented in 2.2.4. The main difference stems from how the integration is performed, whether its evaluated over the remaining gradient or the gradient that has already occurred, with this equation referring to the latter. From Eq. 2.58, it is clear that the magnetization and measured signal form a Fourier pair, allowing for the magnetization, i.e. the object, to be recovered through the application of a Fast Fourier Transform (FFT) [27].

To fully reconstruct the acquired image using Eq. 2.58, several requirements must be met on not only the k-space trajectory but also on the sampling of the signal itself. In MRI, a discrete sampling of a continuous object is typically performed through the use of finite gradients and digital receivers. Both of these lead to a band-limited signal that only covers a narrow range of frequencies across the object, and thus have a finite bandwidth, $BW$. However to avoid any artifacts in the measured signal, the sampling frequency, $SW$, of the digital receivers must exceed twice the maximum frequency component of the acquired signal, i.e. $SW \geq 2 \cdot BW$. This requirement is referred to as the Nyquist criteria.

This criterion is important, as it prevents aliasing from occurring and distorting the reconstructed imaging. Since the signal is discretely sampled there are an infinite number of possible signals that can recreate the sampled data. Each is an identical replica of the lowest frequency signal that is modulated by a high frequency offset. These replica signals are referred to as sidebands of the main baseband. The spacing of the sidebands are calculated from $\text{FOV} = \frac{1}{\Delta k}$ and is referred to as the field-of-view (FOV). In this equation, $\Delta k$ is the spacing between discrete samples in k-space. The resolution is given by $\Delta x = \frac{1}{2k_{\max}}$, with $k_{\max}$ the maximum k-space value sampled.

## 2.3.3  Image Encoding, RF gradients

Another way to modulate the resulting phase of the transverse magnetization is through radio-frequency imaging (RFI) techniques. RFI was first demonstrated by Hoult in his work on rotating frame zeugmatography, but has been an active area of research with several groups expanding on his work [28]–[33]. As this is a rapidly evolving area of research, this section will focus on the recently developed $B_1$ phase encoding technique dubbed Frequency-modulated Rabi-encoded Echoes (FREE).

It was observed that when using an adiabatic full passage (AFP) as a refocusing pulse, the phase of the resulting transverse magnetization is a function of the temporal and spatial properties of the RF field, $B_1(r,t)$ [34]. This $B_1$-dependent phase is additive to the $\Omega$-dependent quadratic phase resulting from the FM sweep [35],[36]. The application of two AFP pulses with identical time-bandwidth products $(R)$ in a double spin-echo sequence leads to refocusing all of the magnetization and removes any $B_0$- and $B_1$-dependent phase factors.

By applying two AFPs with differing $R$ values, a residual $B_1$-dependent phase can be introduced into the resulting echo that is analogous to traditional phase encoding. The original FREE implementation employed a multi-shot double spin-echo (DSE) sequence with two HSn AFP pulses, where the phase imparted by one HS$n$ pulse of a given $R$-value, is modulated by a second HS$n$ pulse having a different $R$-value. The difference in the time-bandwidth product $(\Delta R = \Delta T_{\mathrm{p}} \cdot BW_{\Omega})$ of each shot causes a proportional change in the phase to be imprinted on the ensuing echo.

In a reference frame that rotates at the instantaneous frequency $\omega_{RF}(t)$, the

magnetization evolves about $\boldsymbol{\omega}_{\text{eff}}$ at an effective frequency dictated by the vector sum of the AM and FM functions

$$\boldsymbol{\omega}_{eff}(t) = \omega_1(t)\hat{x}' + (\omega_{RF}(t) - \omega_c)\hat{z}'. \tag{2.60}$$

In practice, these types of AFP pulses are implemented using a phase-modulated (PM) function, which is related to the FM function by

$$\phi(t) = \int_0^t (\omega_{RF}(\nu) - \omega_c)\mathrm{d}\nu. \tag{2.61}$$

In the analysis to follow, the variable $\phi$ is the $\omega_1^{max}$-dependent phase of the transverse magnetization produced by an AFP pulse in the FREE sequence.

## 2.3.4 Analytical Description of Adiabatic Rotation

A valuable tool to understand the behavior of an AFP inversion is through the mathematical framework of propagator analysis. In short, assuming the adiabatic condition is well satisfied, the action of an adiabatic pulse can be described by a set of pure rotations. These rotations can be expressed in matrix form that is then applied to an initial spin density to mimic the ideal behavior of an AFP. By applying these rotation matrices in the proper order it is possible to write an analytical expression describing the double spin-echo FREE sequence with two adiabatic $\pi$ pulses [35]. Starting with the same propagator previously defined

$$\begin{pmatrix} \cos(\psi - \phi)\cos(\Delta\alpha)\cos(\phi) - \sin(\psi - \phi)\sin(\phi) & \sin(\psi - \phi)\cos(\phi) + \cos(\psi - \phi)\cos(\Delta\alpha)\sin(\phi) & \cos(\psi - \phi)\sin(\Delta\alpha) \\ -\sin(\psi - \phi)\cos(\Delta\alpha)\cos(\phi) - \cos(\psi - \phi)\sin(\phi) & \cos(\psi - \phi)\cos(\phi) - \sin(\psi - \phi)\cos(\Delta\alpha)\sin(\phi) & \sin(\psi - \phi)\sin(\Delta\alpha) \\ \cos(\phi)\sin(\Delta\alpha) & \sin(\phi)\sin(\Delta\alpha) & \cos(\Delta\alpha) \end{pmatrix}, \tag{2.62}$$

with $\Delta\alpha$ being the net sweep angle of $\boldsymbol{\omega}_{eff}$, $\phi$ the initial phase of $\omega_{\mathbf{1}}$, and $\psi$ being the total nutation about $\boldsymbol{\omega}_{eff}$ given by $\int_0^{T_{\mathrm{P}}} |\boldsymbol{\omega}_{eff}(t')|\mathrm{d}t'$. Now for the case of a $\pi$ pulse, $\Delta\alpha = \pi$, the matrix simplifies from

$$U_\pi = \begin{pmatrix} -\cos(\psi-\phi)\cos(\phi) - \sin(\psi-\phi)\sin(\phi) & \sin(\psi-\phi)\cos(\phi) - \cos(\psi-\phi)\sin(\phi) & 0 \\ \sin(\psi-\phi)\cos(\phi) - \cos(\psi-\phi)\sin(\phi) & \cos(\psi-\phi)\cos(\phi) + \sin(\psi-\phi)\sin(\phi) & 0 \\ 0 & 0 & -1 \end{pmatrix} \quad (2.63)$$

to

$$U_\pi = \begin{pmatrix} -\cos(\psi-2\phi) & \sin(\psi-2\phi) & 0 \\ \sin(\psi-2\phi) & \cos(\psi-2\phi) & 0 \\ 0 & 0 & -1 \end{pmatrix} \quad (2.64)$$

To perform a sanity check, when two identical pulse are applied sequentially the resulting matrix should only have components along the diagonal. To perform this operation consider $U_\pi U_\pi$,

$$U_\pi U_\pi = \begin{pmatrix} -\cos(\psi-2\phi) & \sin(\psi-2\phi) & 0 \\ \sin(\psi-2\phi) & \cos(\psi-2\phi) & 0 \\ 0 & 0 & -1 \end{pmatrix} \cdot \begin{pmatrix} -\cos(\psi-2\phi) & \sin(\psi-2\phi) & 0 \\ \sin(\psi-2\phi) & \cos(\psi-2\phi) & 0 \\ 0 & 0 & -1 \end{pmatrix}. \quad (2.65)$$

After multiplying the matrix against itself, the product can then be simplified with the final result being the identity matrix,

$$U_\pi U_\pi = \begin{pmatrix} \sin^2(\psi-2\phi) + \cos^2(\psi-2\phi) = 1 & 0 & 0 \\ 0 & \sin^2(\psi-2\phi) + \cos^2(\psi-2\phi) = 1 & 0 \\ 0 & 0 & 1 \end{pmatrix}. \quad (2.66)$$

Now we can consider the more general case when the pulses are not identical. Supposing that the duration of the second pulse is increased by $n\Delta T_\mathrm{p}$ which has the effect of changing the $\boldsymbol{\omega}_{eff}$, and therefore the total amount of phase that is accumulated. Additionally, suppose that $\omega_1^{max}$ varies as a function of position across the sample. Incorporating these minor changes gives us

$$\psi(x,n) = \int_0^{T_\mathrm{p}+n\Delta T_\mathrm{p}} |\boldsymbol{\omega}_{eff}(x,t')| \mathrm{d}t' = \pm \int_0^{T_\mathrm{p}+n\Delta T_\mathrm{p}} \sqrt{\omega_1(x,t')^2 + \Delta\omega(\Omega,t')^2} \mathrm{d}t' \tag{2.67}$$

and therefore our matrix operation becomes

$$U_\pi U_\pi = \begin{pmatrix} -\cos(\psi_{T_{p,1}}-2\phi_1) & \sin(\psi_{T_{p,1}}-2\phi_1) & 0 \\ \sin(\psi_{T_{p,1}}-2\phi_1) & \cos(\psi_{T_{p,1}}-2\phi_1) & 0 \\ 0 & 0 & -1 \end{pmatrix} \cdot \begin{pmatrix} -\cos(\psi_{T_{p,n}}-2\phi_2) & \sin(\psi_{T_{p,n}}-2\phi_2) & 0 \\ \sin(\psi_{T_{p,n}}-2\phi_2) & \cos(\psi_{T_{p,n}}-2\phi_2) & 0 \\ 0 & 0 & -1 \end{pmatrix} \tag{2.68}$$

with $T_{p,n} = T_{p,1} + n\Delta T_\mathrm{p}$. Note that when $n = 0$ the two pulses are identical and the matrix multiplication once again simplifies down to just the identity matrix. The expanded version of Eq. (2.68) is given below,

$$U_\pi U_\pi = \begin{pmatrix} \sin(\psi_{T_{p,1}}-2\phi_1)\sin(\psi_{T_{p,n}}-2\phi_2)+\cos(\psi_{T_{p,1}}-2\phi_1)\cos(\psi_{T_{p,n}}-2\phi_2) & \sin(\psi_{T_{p,1}}-2\phi_1)\cos(\psi_{T_{p,n}}-2\phi_2)-\cos(\psi_{T_{p,1}}-2\phi_1)\sin(\psi_{T_{p,n}}-2\phi_2) & 0 \\ \cos(\psi_{T_{p,1}}-2\phi_1)\sin(\psi_{T_{p,n}}-2\phi_2)-\sin(\psi_{T_{p,1}}-2\phi_1)\cos(\psi_{T_{p,n}}-2\phi_2) & \sin(\psi_{T_{p,1}}-2\phi_1)\sin(\psi_{T_{p,n}}-2\phi_2)+\cos(\psi_{T_{p,1}}-2\phi_1)\cos(\psi_{T_{p,n}}-2\phi_2) & 0 \\ 0 & 0 & 1 \end{pmatrix} \tag{2.69}$$

These propagators only rely on the assumption that the two pulses are adiabatic. In fact, generality is maintained by keeping $\psi$, which can be calculated simply solving $\int_0^{T_\mathrm{p}} |\boldsymbol{\omega}_{eff}(x,t')| \mathrm{d}t'$.

### 2.3.5 Solving for Total Angle of Evolution

This method utilizes the analytical solution for $\int_0^{T_\mathrm{p}} |\boldsymbol{\omega}_{eff}(t')| \mathrm{d}t'$ found for an HS pulse [37]. This work provided a good foundation to build from, requiring minor changes to account for the position dependent $\omega_1^{max}(x)$ and the variable pulse duration, $n\Delta T_\mathrm{p}$.

We begin with the equation for the total nutation about $\boldsymbol{\omega}_{eff}$

$$\psi(t) = \int_0^{T_\mathrm{p}} |\boldsymbol{\omega}_{eff}(t')| \mathrm{d}t' = \pm \int_0^{T_\mathrm{p}} \sqrt{\omega_1(t')^2 + \Delta\omega(\Omega,t')^2} \mathrm{d}t' \tag{2.70}$$

In the rotating frame, with normalized time $(\tau = \frac{2t}{T_\mathrm{p}} - 1)$, the effective field of a HS pulse is described by

$$\boldsymbol{\omega}_{eff}(\tau) = \omega_1^{max} \operatorname{sech}(\beta\tau)\hat{x}' + (\Omega - A\tanh(\beta\tau))\hat{z}' \qquad (2.71)$$

As shown in Eq. 2.70, the vector sum of these two components gives rise to the effective field that the isochromats will follow during an adiabatic sweep. The resulting phase of the isochromats at the end of the pulse will be

$$\psi(\Omega, \omega_1^{max}) = \pm\frac{T_{\mathrm{p}}}{2}\int_{-1}^{1}\sqrt{(\omega_1^{max})^2 \operatorname{sech}^2(\beta\tau') + (\Omega - A\tanh(\beta\tau'))^2}\mathrm{d}\tau' \qquad (2.72)$$

At this point the the analytical solution mentioned above can be directly applied [37]. To make evaluating the integration simpler the terms depending on $\Omega$ and $\omega_1^{max}$ were separated and then summed as seen below.

$$\psi(\Omega, \omega_1^{max}) = \psi_1(\Omega) + \psi_2(\omega_1^{max}) \qquad (2.73)$$

$$\psi_1(\Omega) = \frac{AT_{\mathrm{p}}}{\beta}\ln\left(\frac{1}{\sqrt{A^2 - \Omega^2}}\right) - \frac{T_{\mathrm{p}}\Omega}{2\beta}\ln\left(\frac{A + \Omega}{A - \Omega}\right) \qquad (2.74)$$

$$\psi_2(\omega_1^{max}) = AT_{\mathrm{p}}\left(\frac{1}{\beta}\log(\omega_1^{max}) - 1\right) + \frac{T_{\mathrm{p}}}{2\beta}\sqrt{(\omega_1^{max})^2 - A^2}\cdot\tan^{-1}\left(\frac{2A\sqrt{(\omega_1^{max})^2 - A^2}}{-2A^2 + (\omega_1^{max})^2}\right) \qquad (2.75)$$

With this analytical solution, it is possible to incorporate the position dependent $\omega_1^{max}(x)$ and variable pulse duration, $n\Delta T_{\mathrm{p}}$ with $n \in [0, N-1]$. Incorporating these changes into Eqns.(2.72-2.75) gives us

$$\psi(x, n) = \pm\frac{(T_{\mathrm{p}} + n\Delta T_{\mathrm{p}})}{2}\int_{-1}^{1}\sqrt{(\omega_1^{max}(x))^2 \operatorname{sech}^2(\beta\tau) + (\Omega - A\tanh(\beta\tau))^2}\mathrm{d}\tau' \qquad (2.76)$$

$$\psi(x, n) = \psi_1(n, \Omega) + \psi_2(n, \omega_1^{max}(x)) \qquad (2.77)$$

$$\psi_1(n, \Omega) = \frac{A(T_{\mathrm{p}} + n\Delta T_{\mathrm{p}})}{\beta} \ln\left(\frac{1}{\sqrt{A^2 - \Omega^2}}\right) - \frac{(T_{\mathrm{p}} + n\Delta T_{\mathrm{p}})\Omega}{2\beta} \ln\left(\frac{A + \Omega}{A - \Omega}\right) \quad (2.78)$$

$$\psi_2(n, \omega_1^{max}(x)) = A(T_{\mathrm{p}} + n\Delta T_{\mathrm{p}})\left(\frac{1}{\beta}\log(\omega_1^{max}(x)) - 1\right) + \frac{T_{\mathrm{p}} + n\Delta T_{\mathrm{p}}}{2\beta}\sqrt{(\omega_1^{max})^2 - A^2} \cdot tan^{-1}\left(\frac{2A\sqrt{(\omega_1^{max})^2 - A^2}}{-2A^2 + (\omega_1^{max})^2}\right) \quad (2.79)$$

Eqns.(2.76-2.79) describe the phase at the end of single adiabatic HS pulse as a function of the spatially varying RF amplitude and pulse duration. Now to relate these equations to the time-bandwidth product (R) given the fact that $R = T_{\mathrm{p}} \cdot BW$ and that $BW = A$, and then simplifying further we see that

$$\psi_1(\Omega, n) = A^{-1}(R + n\Delta R) \cdot \left[\frac{A}{\beta}\ln\left(\frac{1}{\sqrt{A^2 - \Omega^2}}\right) - \frac{\Omega}{2\beta}\ln\left(\frac{A + \Omega}{A - \Omega}\right)\right] \quad (2.80)$$

$$\psi_2(\omega_1^{max}(x), n) = A^{-1}(R + n\Delta R) \cdot \left[A(\frac{1}{\beta}\log(\omega_1^{max}(x)) - 1) + \frac{1}{2\beta}\sqrt{(\omega_1^{max}(x))^2 - A^2} \cdot tan^{-1}\left(\frac{2A\sqrt{(\omega_1^{max}(x))^2 - A^2}}{-2A^2 + (\omega_1^{max}(x))^2}\right)\right] \quad (2.81)$$

Simply summing Eq. 2.80 and 2.81 gives the total nutation about $\boldsymbol{\omega}_{eff}$ for a HS pulse. It is now possible to plug these results into the previously derived propagator to get the full analytical solution for the double adiabatic HS pulse with spatially varying $\omega_1^{max}$ and variable pulse duration.

## 2.3.6 Solving for Encoding Steps

We now have the analytical expression for the total nutation about $\boldsymbol{\omega}_{eff}$ for a HS pulse. Using eqns. 2.80 and 2.81, it is possible to determine $\Delta k$ in terms of $\Delta R$ by considering the derivative.

Suppose we apply two HSn pulses, sequentially in time, with the second pulse differing by $\Delta R$. Using the previously derived equations, the resulting phase profile is simply the summation of 2.80 and 2.81.

$$\phi_{total}(\Omega, n, x) = \psi_1(\Omega, n) + \psi_2(\omega_1^{max}(x), n) \tag{2.82}$$

With the difference in phase between each shot given by

$$\Delta\phi = \phi_{total}(\Omega, n + 1, x) - \phi_{total}(\Omega, n, x) \tag{2.83}$$

$$\Delta k = \frac{\partial}{\partial x}[\phi_{total}(\Omega, n + 1, x) - \phi_{total}(\Omega, n, x)] \tag{2.84}$$

If we assume that $\Omega$ is not position dependent, then Eq. 2.81 is all that remains after taking the derivative with respect to position. Evaluating Eq. 2.84 after taking the derivative demonstrates the relationship between $\Delta k$ and $\Delta R$. These equations show the similarity between the phase modulation of $B_1$ gradients and that of traditional pulsed $B_0$ gradients. Further, the formalism presented here can thus be used to apply methodologies initially developed for $B_0$ gradients to $B_1$ based approaches [38].

# Chapter 3

# MRI exploiting frequency-modulated pulses and their nonlinear phase

This chapter has been accepted for publication in the Journal of Magnetic Resonance [36].

## 3.1  Introduction

In the early days of MRI, frequency-modulated (FM) pulses were not widely used in pulse sequences due to their limited versatility to produce the diverse types of spin manipulations required. The uses of FM pulses were restricted to spin inversion and $\pi/2$ excitation which are examples of point-to-point rotations, whereby the magnetization vector $\mathbf{M}$ is rotated from one orientation to another. Point-to-point rotations are generally less demanding than other types, like rotating a plane of dispersed vectors about an axis as needed for spin-echo formation (i.e., a refocusing pulse). Due to the manner in which point-to-point rotations take place, inversion or $\pi/2$ excitation can be performed very precisely with FM pulses even when the radiofrequency (RF) amplitude varies, provided the pulse satisfies the so-called adiabatic condition described below. Such spin manipulations with adiabatic FM pulses can be highly

beneficial in MRI, because MRI is often performed in conditions whereby the transmitter RF field $\mathbf{B}_1^+$ varies spatially [39]–[42]. Significant spatial variation of $\mathbf{B}_1^+$ is generally unavoidable in MRI due to the large size of objects imaged and the RF coil geometries used. Meanwhile at very high magnetic fields, wave-propagation effects also begin to significantly contribute to spatial variation of $\mathbf{B}_1^+$.

The most common FM pulses used for inverting $\mathbf{M}$ are based on the principle of adiabatic rapid passage, whereby the time-dependent pulse frequency $\omega_{\mathrm{RF}}(t)$ sweeps monotonically through a bandwidth (BW) for a duration that is much shorter than the spin's transverse relaxation time, T2. At the time of its introduction into NMR, the chirp pulse with its linear sweep was firmly established in radar [43], [44]. Later, from the field of coherent optics [45], [46] came the so-called hyperbolic secant (HS) pulse which uses amplitude- and frequency-modulation functions based hyperbolic secant and hyperbolic tangent, respectively [22], [47]. The HS pulse has become the most popular adiabatic rapid passage in MRI due its ability to invert magnetization uniformly in a sharply delineated bandwidth, despite large changes in the amplitude of the transmitter RF field, $B_1^+$ .

The process by which $\mathbf{M}$ changes its orientation during an adiabatic rapid passage can be most easily visualized in a reference frame that rotates with $\omega_{\mathrm{RF}}(t)$. In this so-called FM frame, a torque is exerted upon $\mathbf{M}$ by a time-dependent effective magnetic field $B_{\mathrm{eff}}(\mathrm{t})$, which is the vector sum of $\mathbf{B}_{\mathrm{eff}}(t)$ and the longitudinally-oriented time-dependent off-resonance field,

$$\Delta \mathbf{B}_0(t) = \gamma^{-1}(\omega_0 - \omega_{\mathrm{RF}}(t))z' \qquad (3.1)$$

where $\gamma$ is the gyromagnetic ratio. In a doubly rotating frame where the orientation of $\mathbf{B}_{\mathrm{eff}}(t)$ is stationary, it can be shown that the component of $\mathbf{M}$ that is initially aligned with $\mathbf{B}_{\mathrm{eff}}$ will remain approximately aligned with $\mathbf{B}_{\mathrm{eff}}$ throughout the pulse, provided the adiabatic condition is well satisfied during the pulse [39], [48], [49]. The latter condition can be expressed as

$$\gamma \mathbf{B}_{\mathrm{eff}}(t) >> \left| \frac{d\alpha}{dt} x \right| \qquad (3.2)$$

where $\alpha$ is the time-dependent angle that $\mathbf{B}_{\mathrm{eff}}$ rotates in the FM frame. Likewise,

under the adiabatic condition, the components of $\mathbf{M}$ that are initially perpendicular to $\mathbf{B}_{\text{eff}}$ will remain so during the pulse. In this manner, the transverse components of $\mathbf{M}$ can undergo an adiabatic $\pi$-rotation as needed to generate a spin echo. In the latter case, however, the phase of the transverse magnetization in the resultant spin echo varies quadratically as a function of $\omega_0$, which in the early days of MRI was considered an undesirable side effect since precious signal was sacrificed; hence, adiabatic rapid passage was not commonly used in spin-echo MRI sequences.

When the adiabatic condition is not adequately satisfied (e.g., when the pulse length is too short to satisfy 3.2), excitation of a given flip angle $\theta$ can be performed by a (non-adiabatic) full-passage sweep simply by setting the RF amplitude appropriately. In this case, however, sensitivity to spatial variation of $B_1^+$ persists, and like in the adiabatic condition, the resultant phase of the transverse magnetization is a nonlinear function of $\omega_0$.

In the early days of applying FM pulses in MRI, such nonlinear phase could not be compensated easily, but nowadays many methods exist to remove or even exploit the nonlinear phase produced by FM pulses. Examples include exploiting the nonlinear phase for recovering susceptibility-induced signal loss [50]–[53], reducing demand for high receiver dynamic range in 2D and 3D MRI [54], [55], and performing $B_1^+$ mapping [34].

The aim of this article is to present some old and new ways in which nonlinear phase can be compensated and exploited in MRI. We focus on gradient- and spin-echo MRI sequences, whereas emerging new imaging methods that exploit nonlinear phase for spatiotemporal encoding, like SPEN [56], [57], RASER [58], RASE [59], and STEREO [60], are not covered herein.

## 3.2   Nonlinear Phase: Some Things Old

Kunz was the first to analyze the use of FM pulses in spin-echo MRI and identified essential relationships between the $\pi/2$ and $\pi$ FM pulses that, to a first order approximation, eliminate the pulse-induced nonlinear phase in slice-selective spin-echo imaging [61]. Around this same time, a novel class of composite FM pulses was developed which combined multiple segments of the adiabatic rapid passage to cancel

the nonlinear phase of the individual segments [62]–[69]. Some of these composite FM pulses can perform rotations about an axis in a fixed-frequency rotating frame that is invariant despite changing the resonance offset, and as such do not impart nonlinear phase on the resultant transverse magnetization for a reasonable bandwidth of resonance frequencies, $\omega_0$. Unlike a conventional pulse, a composite FM pulse can rotate a plane of magnetization vectors about a specified axis despite large spatial variations of $B_1^+$, which can be advantageous for certain MRI applications. However, because they are composite pulses, these FM pulses are often longer than their adiabatic rapid passage counterparts, and thus, deposit greater RF energy. Moreover, these pulses include one or more large internal phase jumps which unfortunately destroy the capability to perform slice or slab selection in MRI, although some composite FM pulses developed subsequently overcame this shortcoming [70]–[73].

Another approach to compensate the nonlinear phase in spin-echo MRI involves using two identical adiabatic rapid passages spaced appropriately in time to generate a double spin echo [74]. In this way, the nonlinear phase produced by the first FM pulse is undone by the second FM pulse. Kunzs' formulation for chirp pulses achieved mutual cancellation of the nonlinear phase of $\pi/2$ and $\pi$ FM pulses in spin-echo MRI, and was extended later to HS and other FM pulses [37], [75], [76]. An advantage of these FM pulses in spin-echo MRI arises when the refocusing pulse is adiabatic and thus insensitive to spatial $B_1^+$ variation, for maximizing signal while minimizing unwanted image artifacts.

For the case of gradient-recalled echo (GRE) imaging, Pipe derived the first analytical description of the nonlinear phase and implemented a quadratic transformation to reconstruct GRE images in MR angiography [77]–[79]. In that groundbreaking work, excitation was performed with a chirp pulse, the simplest of all FM pulses since $\omega_{\mathrm{RF}}(t)$ sweeps only linearly while the RF amplitude is constant (i.e., unlike most other FM pulse, the RF amplitude is not modulated in the chirp). Pipe's work was later expanded upon with the derivation of analytic expressions for cases of excitation with the HS pulse [55], [80], [81]. As already mentioned, the characteristics of the slab (or slice) profile produced by the HS pulse are better than those of the chirp pulse, specifically the flatness of the baseband and the steepness of the transition regions. As compared with conventional amplitude-modulated pulses like the sinc pulse, an

advantage of FM pulses for 3D GRE imaging is the ability to excite a high bandwidth with lower peak RF amplitude. Due to their multiple favorable properties, HS pulses are nowadays frequently employed in 3D GRE sequences.

When acquiring either phase- or frequency-encoded data in the direction of the nonlinear phase, as occurs for example when an FM pulse is used for slab-selection in 3D MRI, this spatial dimension of the image can be reconstructed in the usual manner using only an inverse Fourier transformation [55]. In this case, no loss of signal occurs inside the selected slab when the number of k-space points acquired in that spatial direction is equal to or greater than the time-bandwidth product of the pulse, $R$ (i.e., the product of the pulse's bandwidth in Hz and duration in seconds). Alternatively, such spatially-encoded nonlinear phase can be removed prior to FT, as done in sweep imaging with Fourier transformation (SWIFT) [43], [82], [83]. In SWIFT, the quadratic phase is removed by performing a correlation operation, similar to that done in rapid scan correlation spectroscopy [84]. Likewise, when an odd number of FM pulses are used to form a spin echo, correlation can also be used to remove nonlinear phase, provided it is captured by some type of spatial encoding.

## 3.3   Nonlinear Phase: Some Things New

It is important to note that a HS pulse is a special case of the more general class of HSn pulses, in which $n = 1$, so it is commonly referred to as an HS1 pulse [85], [86]. The normalized amplitude- and frequency-modulated functions for HSn pulses are

$$\text{AM} = \text{sech}(\beta \tau^n) \tag{3.3}$$

$$\text{FM} = \int \text{sech}^2(\beta \tau^n) \mathrm{d}\tau \tag{3.4}$$

In these equations, $\tau$ corresponds to normalized time and $\beta$ is a truncation factor usually defined as $\text{sech}(\beta) = 0.01$ . By adjusting the parameter $n$ the steepness of the frequency sweep can be flattened to approach that of a chirp. As $n$ increases the transition region in the resulting excitation profile is smoothed and the required peak

power is reduced [87]. However despite changes to $n$, modulating the RF frequency in this manner produces a quadratic phase in the excitation profile.

FM pulses are historically described in the FM reference frame, as the physical mechanism of adiabatic pulses is more apparent from that perspective. However, the FM and phase-modulated (PM) descriptions are equivalent when the PM function is given by the integral of the FM function over time. In modern hardware, usually the PM version of the pulse is implemented; therefore the FM pulses will be described in terms of their corresponding AM and PM functions moving forward [48].

As first described by Pauly et al. [24], multidimensional small tip angle pulses can be described by a parameterized trajectory through excitation k-space in which the trajectory is determined by the integral of the applied gradients during the RF pulse. Building off of this work, Conolly et al. introduced a 2D selective adiabatic pulse that covers the entirety of excitation k-space in a single shot [88]. The pulse utilizes a series of selective sinc pulses played out during an oscillating echo-planar-type gradient train. Along the direction of the blipped gradient, the peak amplitude and phase are modulated according to that of an HS1 pulse [22]. By modulating the amplitude and phase along this blipped dimension, the pulse is able to maintain the advantages of the HS1 pulse, i.e., inverting the magnetization uniformly despite large changes in $B_1^+$.

Later, Dumez et al. improved upon this 2D pulse by replacing the amplitude-modulated (sinc) pulses with a frequency-modulated chirp pulse, leading to a multi-dimensional frequency-swept pulse [56]. Two chirp pulses are played out along both dimensions while maintaining the same echo-planar-type gradient train. This simple change allows for an increase in the bandwidth of the pulse along both dimensions but creates a 2D parabolic phase profile across the excitation. This work was described in physical space, rather than excitation k-space, thus providing little guidance in specifying pulse parameters.

The work performed by Connolly and Dumez et al. laid the foundation for more recent work that sought to utilize the advantages of a 2D-FM approach. In Jang et al. [89], the Cartesian trajectory was replaced by a parameterized spiral, while applying a rotationally symmetric 2D HSn weighting (Fig. 3.1). In this approach, an excitation k-space formalism provides the theoretical framework to describe the

behavior of the magnetization, both its magnitude and phase, as a function of space and time. It was shown that this type of pulse creates a region of maximum phase-coherence, in a spatiotemporal manner, that is translated along a spiral trajectory in physical space. As the area of maximum phase-coherence moves along this spiral, each isochromat experiences the gradient- and phase-modulation multiple times causing them to excite, dephase, and then rephase rather than being sequentially excited in time. Due to this unique spatiotemporal excitation method, the pulse does not ever become adiabatic as the RF amplitude is increased. However, when used for excitation, the resulting phase of $\mathbf{M}$ in the circular region is a parabolic function of spatial coordinates.
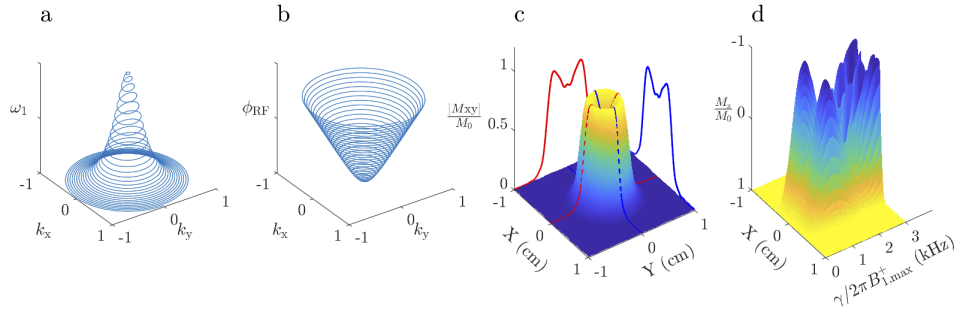


**Fig. 3.1.** The 2D FM pulse with a 28-turn spiral k-space trajectory of Jang et al. [89]. The pulse is shown as amplitude (a) and phase (b) functions of $k_x$ and $k_y$. The transverse magnetization's phase profile in physical space is determined by the shape of the phase modulation (b), resulting in a parabolic spatial-phase variation. The pulse excites a circular region with a central cusp that is readily visible in the cross sections shown (c). As the RF amplitude ($B_{1,\mathrm{max}}^+$) increases in order to produce larger flip angles the flatness of the excitation becomes even less uniform, as can be seen from a plot of the normalized longitudinal magnetization along one spatial dimension versus $B_{1,\mathrm{max}}^+$ (d). Simulation parameters were: pulse duration = 19.7 ms, time-bandwidth product ($R$) = 4.7, and for (c), peak RF amplitude ($\gamma B_{1,\mathrm{max}}^+/2\pi$ = 465 Hz.

Despite its non-adiabatic character, this 2D excitation pulse can be modified to accomplish a uniform excitation with spatially varying $B_1^+$. Previously, it was shown that by mapping the spatial $B_1^+$ profile and then using this to adjust the amplitude modulation according to the known 2D spatial trajectory of phase coherence,

a uniform flip angle can be achieved with inhomogeneous $B_1^+$ [89]. However, even when accounting for variable flip angle in this manner, the resulting excitation profile possesses a cusp in the center of the circular excitation region. This central imperfection occurs because the spatiotemporal trajectory of the frequency sweep abruptly terminates (or begins) at the center position.

Mullen et al. improved upon this previous work by replacing the spiral with the more traditional oscillating echo-planar gradient train and modulating the amplitude and phase in two dimensions according to an HSn pulse [90], [91]. In terms of the k-space trajectory, the amplitude- and phase-modulation functions are

$$\omega_1 = \omega_{1,\text{max}} \operatorname{sech}(\beta \mathbf{K}_f(t)) \operatorname{sech}(\beta \mathbf{K}_s(t)) \tag{3.5}$$

$$\Phi_{\text{RF}} = \frac{\pi R_f}{2\beta} \log(\cosh(\beta \mathbf{K}_f(t))) \pm \frac{\pi R_f}{2\beta} log(cosh(\beta \mathbf{K}_s(t))) \tag{3.6}$$

with $\mathbf{K}_{f,s}$ normalized by Eq. 3.7 to ensure $\mathbf{K}_{f,s} \in [-1,1]$ , according to Eq. [7] of Ref. [24],

$$k_{f,s} = \frac{\gamma}{2} \left| \int_0^{\text{T}} G_{f,s}(t') \mathrm{d}t' \right| \tag{3.7}$$

In these equations, $\beta$ corresponds to a truncation factor and $R_{f,s}$ corresponds to the time-bandwidth product along the fast and slow (blipped) dimensions, respectively. Simulations of this pulse (Fig. 3.2) were performed using the following parameters: 28 lines of excitation k-space, a pulse duration of 19.7 ms, time-bandwidth product of 10 ($R_f = R_s = 10$), with a peak RF amplitude ($\gamma B_{1,\text{max}}^+/2\pi$) of 653 Hz to achieve a $\pi/2$ flip angle. In practice the pulse duration of these 2D FM pulses will be longer; in these simulations the gradient slew rate was assumed to be infinite. Either the + or – in Eq. 3.6 may be used; here, the – sign was chosen.

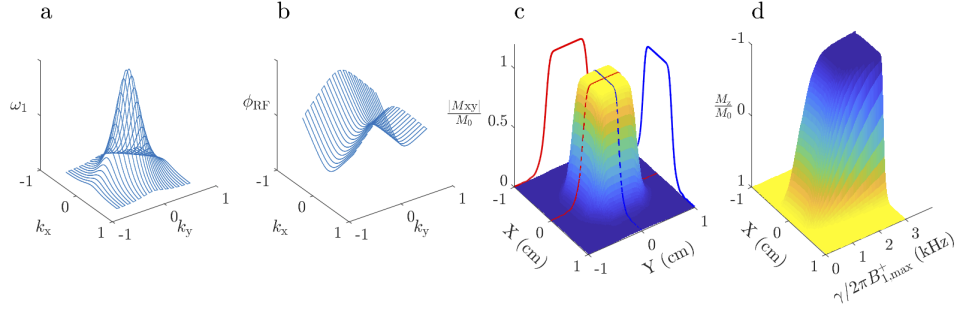**Fig. 3.2.** 2D FM pulse using a Cartesian k-space trajectory. The pulse is shown as amplitude (a) and phase (b) functions of $k_x$ and $k_y$. The resulting phase profile is a hyperboloid in physical space, due to the shape of the phase modulation (b). The pulse excites a rectangular region (c) with a flat top as can be seen from the cross sections shown. As the RF amplitude ($B_{1,\mathrm{max}}^+$) varies, the flatness of the profile persists as the flip angle increases to $\pi$ (d). Beyond this point, no changes in flip angle occur despite further increases in $B_{1,\mathrm{max}}^+$ because the threshold $B_{1,\mathrm{max}}^+$ value for satisfying the adiabatic condition has been reached. Note, the pulse also behaves adiabatically along the other spatial dimension not shown.

The general approach described above provides extensive flexibility to tailor RF pulses to meet the specific needs of an experiment. Two new 2D pulses described below involve further modifying the excitation k-space trajectory and altering the AM and PM functions along a given trajectory (i.e., by changing $\omega_1$ and $\Phi_{\mathrm{RF}}$).

## 3.3.1   Reducing pulse length with circular k-space sampling

Maudsley et al. proposed a modified sampling technique for magnetic resonance spectroscopic imaging in which a circular region of k-space was sampled using a bounded Cartesian grid [92]. This equates to modifying the oscillatory echo-planar gradient train to traverse within a circularly bounded region of space, thus only encoding information from within the circle. The same methodology of bounding k-space on readout can be applied to excitation k-space. By maintaining the same 2D amplitude- and phase-modulated functions but restricting the excitation k-space to within a circle defined by $k_{max}$, a square region can be excited with a shorter pulse duration. To test the validity of this approach, simulations were performed using the following parameters: 28 lines of excitation k-space, a pulse duration of 14.9 ms, time-

bandwidth product of 10 ($R_f = R_s = 10$), with a peak RF amplitude ($\gamma B^+_{1,\text{max}}/2\pi$) of 508 Hz to achieve a $\pi/2$ flip angle (Fig. 3.3).
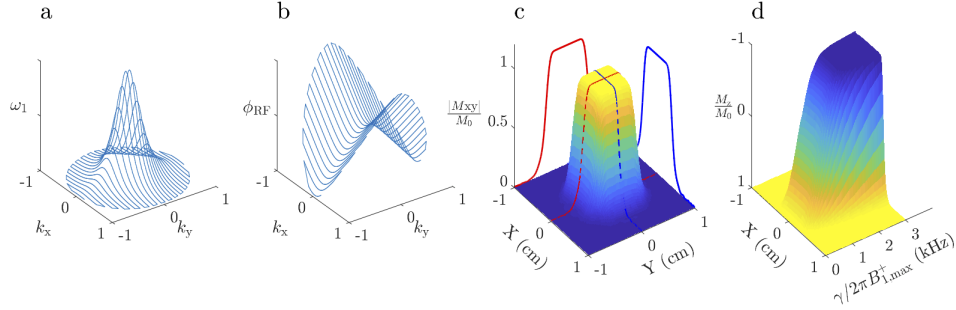


**Fig. 3.3.** 2D FM pulse using a bounded Cartesian k-space trajectory. The pulse is the same as that shown in Fig. 2, except a circular boundary has been applied to the Cartesian trajectory to shorten the pulse. Shown are the amplitude (a) and phase (b) functions of $k_x$ and $k_y$ and the excited rectangular region (c). As the phase-modulation function (b) is the same as the previous pulse, the resulting phase profile is a hyperboloid in physical space. As the RF amplitude ($B^+_{1,\text{max}}$) varies the flatness of the excitation persists, and at higher $B^+_{1,\text{max}}$ values the flip angle increases and approaches $\pi$ despite further increases (d). The pulse also behaves adiabatically along the other spatial dimension not shown.

By adjusting the Cartesian trajectory to be bounded by a circle, the pulse as designed herein retains all of the advantages of the 2D frequency sweep but covers 78.5 % the area of a standard Cartesian grid.

## 3.3.2 Uniform response in a circular region using Cartesian k-space

The other proposed method to tailor these RF pulses is to use rotationally symmetric amplitude-and phase-modulated functions while using a Cartesian trajectory, as described by Mullen et al. By incorporating the excitation k-space weighting of the pulse in Fig. 3.1 into Eqs. 3.5 and 3.6, it is possible to use the same Cartesian trajectory to excite a circular region with uniform flip angle. In terms of the k-space trajectory, the new amplitude- and phase-modulated functions are,

$$\omega_1 = \omega_{1,\text{max}} sech(\beta\sqrt{\mathbf{K}_f(t)^2 + \mathbf{K}_s(t)^2}) \tag{3.8}$$

$$\Phi_{\text{RF}} = \frac{\pi R_f}{2\beta} log(cosh(\beta\sqrt{\mathbf{K}_f(t)^2 + \mathbf{K}_s(t)^2})). \tag{3.9}$$

These equations show that only a slight modification is needed to change the excitation region from a square to a circle, while maintaining the same Cartesian trajectory. As compared to the original spiral 2D pulse of Jang et al. [89], this pulse behaves adiabatically and corrects for the cusp in the excitation profile.



**Fig. 3.4.** 2D FM pulse using a bounded Cartesian k-space trajectory. The pulse is the same as that shown in Fig. 2, except a circular boundary has been applied to the Cartesian trajectory to shorten the pulse. Shown are the amplitude (a) and phase (b) functions of $k_x$ and $k_y$ and the excited rectangular region (c). As the phase-modulation function (b) is the same as the previous pulse, the resulting phase profile is a hyperboloid in physical space. As the RF amplitude ($B_{1,\text{max}}^+$) varies the flatness of the excitation persists, and at higher $B_{1,\text{max}}^+$ values the flip angle increases and approaches $\pi$ despite further increases (d). The pulse also behaves adiabatically along the other spatial dimension not shown.

These pulses are unique in that two frequency sweeps are performed, resulting in two distinct excitation bandwidths; one corresponding to the oscillatory ($\mathbf{K}_f$) dimension and the other along the blipped ($\mathbf{K}_s$) dimension. The bandwidth along the oscillatory dimension is analogous to a traditional FM pulse, which can be large; however, along the blipped dimension, the bandwidth is determined by the number of segments and the duration of the oscillatory portion. By segmenting the Cartesian k-space trajectory of these 2D pulses and acquiring the segments in multiple shots,

41

Mullen et al. [90], [91] demonstrated an increased resilience to B0 inhomogeneity along both spatial dimensions of the pulse. The increased resilience is rooted in the decreased duration of each pulse segment, thereby increasing the segment BW. In addition, this pulse can compensate for inhomogeneities in a similar manner to the previous spiral pulse. Regardless of the excitation k-space weighting, this pulse can produce a uniform flip angle of any arbitrary choosing (i.e., from $\theta \ll \pi/2$ to $\pi$) and the produced phase profile varies nonlinearly in space (e.g., a parabolic or hyperbolic function) according to the shape of the PM function.

Table 3.1 and 3.2 lists several important characteristics of the adiabatic pulses presented in this work. These pulses are compared for two flip angles ($\pi/2$ and $\pi$ with a 1D HS as a baseline. The 2D adiabatic pulses have similar performance characteristics, however the circular weighted pulse generally performs better overall. From the RF amplitude ($B_{1,\max}^+$), it can be seen that the circular weighted pulse requires less power to perform the same rotation as the other pulse. This is indicative of the circular weighting more evenly distributing RF energy in time. Consequently the relative RF energy deposited ($E_{rel}$) is lower for this pulse at both flip angles. The bandwidths of each pulse were determined empirically from Bloch simulations. For the 2D pulses, the difference along each dimension becomes clear, with all of the 2D pulses having a very large BW along the fast dimension compared to the slow one. This discrepancy is further exemplified by examining the quality factory ($Q$) along these dimensions. This shows the need for trajectory segmentation [90], [91], [93], [94] of these 2D pulses to increase the BW of the pulse. However, segmentation comes at a cost to total experiment time as full acquisitions are required per pulse segment. Exploiting similar techniques from parallel imaging, it is possible to compensate for under-sampled acquisitions by treating the data from different pulse segments as if they originated from "virtual coils" [95]. The acquisition k-space for each pulse segment is under-sampled and parallel imaging techniques [96] are used to synthesize the unsampled data.

Table 3.1: Properties of adiabatic pulses corresponding to a Flip Angle $= \pi/2$.

| | Flip Angle $= \pi/2$ | | | |
|---|---|---|---|---|
| | 1D HS | 2D Cartesian | 2D Bounded Cartesian | 2D Circular Weighting |
| R | 10 | 10 | 10 | 10 |
| $T_\mathrm{p}$ (ms) | 5.0 | 19.7 | 14.9 | 19.7 |
| $\gamma B_1^{\mathrm{max}}/2\pi$ (kHz) | 0.38 | 0.73 | 0.70 | 0.64 |
| $\gamma B_1^{\mathrm{rms}}/2\pi$[b](kHz) | 0.16 | 0.13 | 0.15 | 0.12 |
| $E_{rel}$[c] | 1.00 | 2.62 | 2.53 | 2.22 |
| $\Delta\Omega_{90\%}^{\mathrm{f}}$ (kHz) | 1.70 | 12.62 | 12.51 | 13.59 |
| $\Delta\Omega_{90\%}^{\mathrm{s}}$(kHz) | - | 0.43 | 0.56 | 0.47 |
| $Q_{\mathrm{f}}$[d] | 10.32 | 94.08 | 82.6 | 109.9 |
| $Q_{\mathrm{s}}$[d] | - | 3.19 | 3.72 | 3.79 |

[b] is the root mean square (RMS) of the amplitude-modulation function.

[c] $E_{rel} = \frac{int_0^{T_\mathrm{p}}|B_1(t)|^2 dt}{int_0^{T_\mathrm{p}}\left|B_{1,\mathrm{HS}}(t)\right|^2 dt}$, where $B_{1,\mathrm{HS}}(t)$ is the amplitude-modulation function of the HS pulse.

[d] $Q_{\mathrm{f,s}} = \frac{\Delta\Omega_{90\%}^{fms}}{(\gamma B_1^{RMS}/2\pi)}$ , where $\Delta\Omega_{90\%}^{fms}$ corresponds to the effective bandwidth along a given dimension, and for flip angles of $\pi/2$ and $\pi$ these are defined as $M_z/M_0 < 0.2$ and $M_z/M_0 < -0.8$, respectively.

Table 3.2: Properties of adiabatic pulses corresponding to a Flip Angle $= \pi$.

| | Flip Angle $= \pi$[a] | | | |
|---|---|---|---|---|
| | 1D HS | 2D Cartesian | 2D Bounded Cartesian | 2D Circular Weighting |
| R | 10 | 10 | 10 | 10 |
| $T_\mathrm{p}$ (ms) | 5.0 | 19.7 | 14.9 | 19.7 |
| $\gamma B_1^{\mathrm{max}}/2\pi$ (kHz) | 0.90 | 1.66 | 1.60 | 1.45 |
| $\gamma B_1^{\mathrm{rms}}/2\pi$[b](kHz) | 0.39 | 0.31 | 0.35 | 0.28 |
| $E_{rel}$[c] | 1.00 | 2.44 | 2.37 | 2.04 |
| $\Delta\Omega_{90\%}^{\mathrm{f}}$ (kHz) | 1.50 | 13.84 | 13.67 | 14.74 |
| $\Delta\Omega_{90\%}^{\mathrm{s}}$(kHz) | - | 0.37 | 0.49 | 0.43 |
| $Q_{\mathrm{f}}$[d] | 3.90 | 45.06 | 39.49 | 52.76 |
| $Q_{\mathrm{s}}$[d] | - | 1.21 | 1.41 | 1.54 |

[a] Flip angle $= \pi$ corresponds to $M_z = -0.99M_0$

[b] is the root mean square (RMS) of the amplitude-modulation function.

[c] $E_{rel} = \frac{int_0^{T_\mathrm{p}}|B_1(t)|^2 dt}{int_0^{T_\mathrm{p}}\left|B_{1,\mathrm{HS}}(t)\right|^2 dt}$, where $B_{1,\mathrm{HS}}(t)$ is the amplitude-modulation function of the HS pulse.

[d] $Q_{\mathrm{f,s}} = \frac{\Delta\Omega_{90\%}^{fms}}{(\gamma B_1^{RMS}/2\pi)}$ , where $\Delta\Omega_{90\%}^{fms}$ corresponds to the effective bandwidth along a given dimension, and for flip angles of $\pi/2$ and $\pi$ these are defined as $M_z/M_0 < 0.2$ and $M_z/M_0 < -0.8$, respectively.

## 3.4   Nonlinear Phase: Compensation

Recently several groups have proposed different techniques to try to minimize the undesirable phase created by FM pulses. Building off of Kunz's double chirp spin-echo sequence, Cano et al. and subsequently Power et al. proposed a triple-pulse scheme to further compensate for any nonlinear phase [61], [97]. Cano et al. demonstrated that by adding an additional excitation pulse and replacing the chirps with adiabatic HSn pulses, it is possible to eliminate the severe sensitivity to inhomogeneity while selecting a rectangular region with a relatively flat phase [98]. These changes allow for good phase compensation, but at the expense of significantly increased average RF power deposition. Foroozandeh et al. proposed replacing the HSn pulses with chirp pulses in order to reduce the peak RF power and exploit the linear frequency sweep of the chirp pulse [99].

Chirp pulses are characterized by a linear relationship between time and frequency and therefore phase. Using this relationship, Foroozandeh et al. showed that by simulating the residual nonlinear phase created by a FM pulse, it could be compensated for by modifying the frequency sweep of the third excitation pulse. Incorporating this change into a CHORUS (CHirped, ORdered pulses for Ultra-broadband Spectroscopy) type sequence, they were able to mitigate the effect of resonance offsets and completely compensate for the residual nonlinear phase of the FM pulses [99]. Their pulse sequence maintains the insensitivity to $B_1^+$ of the earlier adiabatic triple-excitation [98], but can be driven to very large bandwidths thus providing robustness to $B_0$ inhomogeneities as well. They were able to achieve a very broadband excitation with a nearly flat phase, therefore almost completely compensating for the undesirable nonlinear phase of the FM chirp pulses.

As previously mentioned, Park and Garwood demonstrated several conditions in which the nonlinear phase created by the HSn pulse can be mitigated in spin-echo MRI [37]. Three different compensation schemes were proposed that resulted in nearly constant phase across the excitation. Extending this work, we propose a new method to compensate for the nonlinear phase by utilizing higher-order gradient fields to perform a spin-echo sequence.

With the advancement of new gradient technology, like multi-coil gradient arrays,

it is now possible to manipulate higher-order gradient fields in a similar manner to traditional linear gradients [100], [101]. Several groups have begun exploring different uses for higher-order gradients. Most of that work is focused on improving data readout rather than spin excitation. Zaitsev et al. proposed a 3D GRE sequence that utilizes a constant $x^2 + y^2$ to impart a known quadratic phase across k-space that can be exploited in parallel imaging type applications [102]. Using a similar constant $\gamma G_{z2}(z^2 - \frac{1}{2}(x^2 + y^2))$ gradient, we propose a new method to compensate for the nonlinear phase in a spin-echo type sequence that employs two identical 1D HSn pulses.
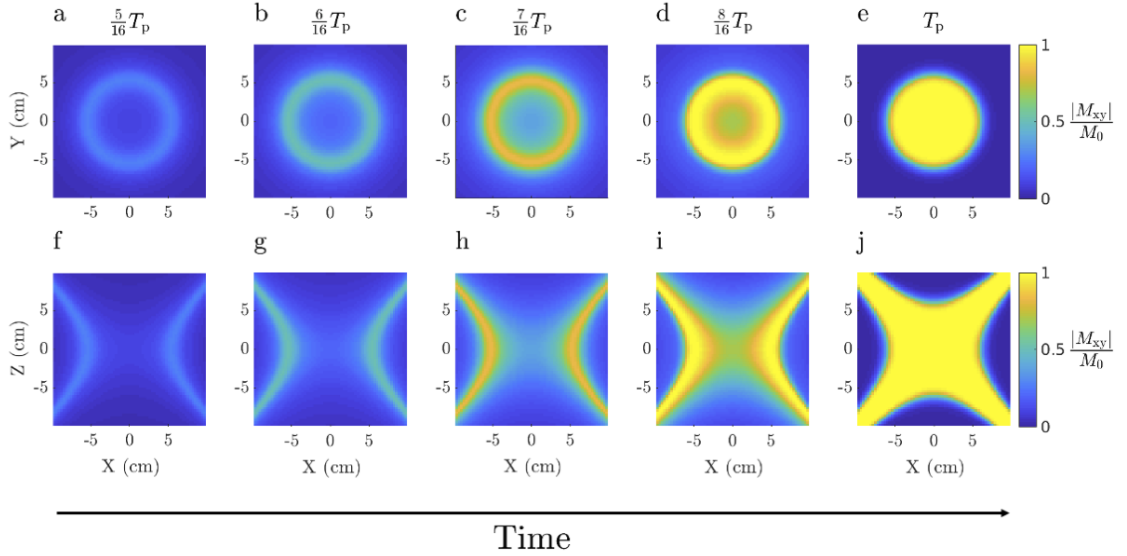


**Fig. 3.5.** The temporal progression of the spatiotemporal excitation is shown for the case of applying a standard HS1 pulse in the presence of a z2 shim, $\gamma G_{z2}(z^2 - \frac{1}{2}(x^2 + y^2))$. Each subplot shows a different time point during the RF pulse to illustrate how excitation progresses from the edge of the z2 field towards the vertex. Subplots (a) – (e) correspond to the xy plane centered at $z = 0$ and (f) – (g) to the xz plane centered at $y = 0$. This can be achieved by applying a standard z2 shim or by using special gradient coils (e.g., a multi-coil array).

We begin with a 3D spatially varying gradient field and transmitting a rapid passage pulse that excites isochromats in a spatiotemporal manner, such that excitation begins at the edges of the field and progresses towards the center (Fig. 3.5).

45

This unique spatiotemporal excitation is due to the pulse sweeping over isochromats further out in the field first before those closer to the center of the field. The region selected is determined by the bandwidth of the frequency sweep, the center frequency of the sweep, and the frequencies spanned by the z2 shim. As a result of the spatiotemporal excitation, the different isochromats have a unique time of resonance and begin accumulating phase at different rates depending on their relative position in the z2 shim. To facilitate the conceptualization of the effect of the nonlinear gradient on the final phase, consider only the effective linear gradient at each position in space and along $z = 0$. This is analogous to considering the derivative of a quadratic field at each point in space. The effective linear gradient is as follows:

$$G_{x^2,y^2} = -\frac{G_{z2}}{2}(x^2 + y^2), \qquad (3.10)$$

$$G_{\text{eff}} = -\frac{\partial}{\partial x \partial y}G_{x^2,y^2} = -\frac{G_{z2}}{2}(2x + 2y); \qquad (3.11)$$

where $G_{x^2,y^2}$ is the applied quadratic field, $\gamma G_{z2}$ is the effective gradient strength in Hz/cm2, and $G_{\text{eff}}$ is the effective linear gradient at each point in space. At the center of the quadratic gradient, $G_{\text{eff}}$ is essentially zero; thus, the pulse has no selectivity and easily excites all of this space. Although the quadratic phase imparted on the magnetization by the FM pulse is distributed across this entire region, the gradient is small in this (large) center region, and as a result, the phase is relatively constant there. In the radial directions $G_{\text{eff}}$ increases linearly and the limits of the excited region, as determined by the range of the frequency sweep, are delineated sharply due to the rapidly increasing steepness of the gradient. This behavior applies to even higher order gradients, beyond quadratic, although $G_{\text{eff}}$ will no longer vary linearly with space but will depend on the derivative of the applied gradient. In addition to altering the quadratic phase across the selected region, $G_{\text{eff}}$ determines the rate at which isochromats begin to dephase. Due to the spatiotemporal nature of FM pulses, isochromats around the center of the bowl, a region of small $G_{\text{eff}}$, can be excited last and then dephase slower than those along the edge of the bowl. This variable dephasing can be exploited to minimize the total dephasing across the selected region. Considering the benefits provided by the quadratic gradient and the spatiotemporal

46

nature of a FM pulse, it should be possible to minimize any nonlinear phase utilizing a standard spin-echo type sequence without modifying the timing or characteristics of the pulses.

### 3.4.1 Simulations

To test the validity of this approach, simulations were performed using an in-house Bloch simulator written in MATLAB (The MathWorks, Natick, MA). A 3D spin-echo sequence was created using two HS1 pulses, each with a time-bandwidth product of 10 and a duration of 5 ms (Fig. 3.6). The first HS1 pulse had a peak RF amplitude ($\gamma B^+_{1,max}/2\pi$) equal to 379 Hz to achieve a $\pi/2$ flip angle, and the second was set to 895 Hz to achieve a 99% inversion. EXORCYCLE was used to eliminate any non-refocused components of the transverse magnetization [103]. A constant $\gamma G_{z2}(z^2 - \frac{1}{2}(x^2 + y^2))$ gradient, with $\gamma G_{z2}$ set to 30 $Hz/cm^2$, was applied to simulate the presence of a z2 shim across a 19.2 $cm^2$ FOV at z = 0. The transverse magnetization was plotted 2.5 ms after the end of the second pulse. To simulate the effect that a static frequency offset (e.g., due to chemical shift) has on the excitation profile, five constant offsets were applied while keeping all other simulation parameters the same.

### 3.4.2 Results

From the simulation, it can be seen that a sharply delineated hyperboloid of various sizes is excited even with the constant resonance offsets applied (Fig. 3.7). To understand the affect a constant offset has on the excitation profile, first consider the 3D frequency distribution created by the z2 shim. Relative to the laboratory frame at magnet isocenter,

$$\omega(x, y, z) = \omega_0 + \gamma G_{z2}(z^2 - \frac{1}{2}(x^2 + y^2)) \qquad (3.12)$$

The isofrequency contours are defined by a hyperboloid with its vertex located at magnet isocenter (Eq. 3.12, Fig. 3.8). Applying a tailored RF pulse excites isochromats within the pulse BW, with the edge of the excited region defined by
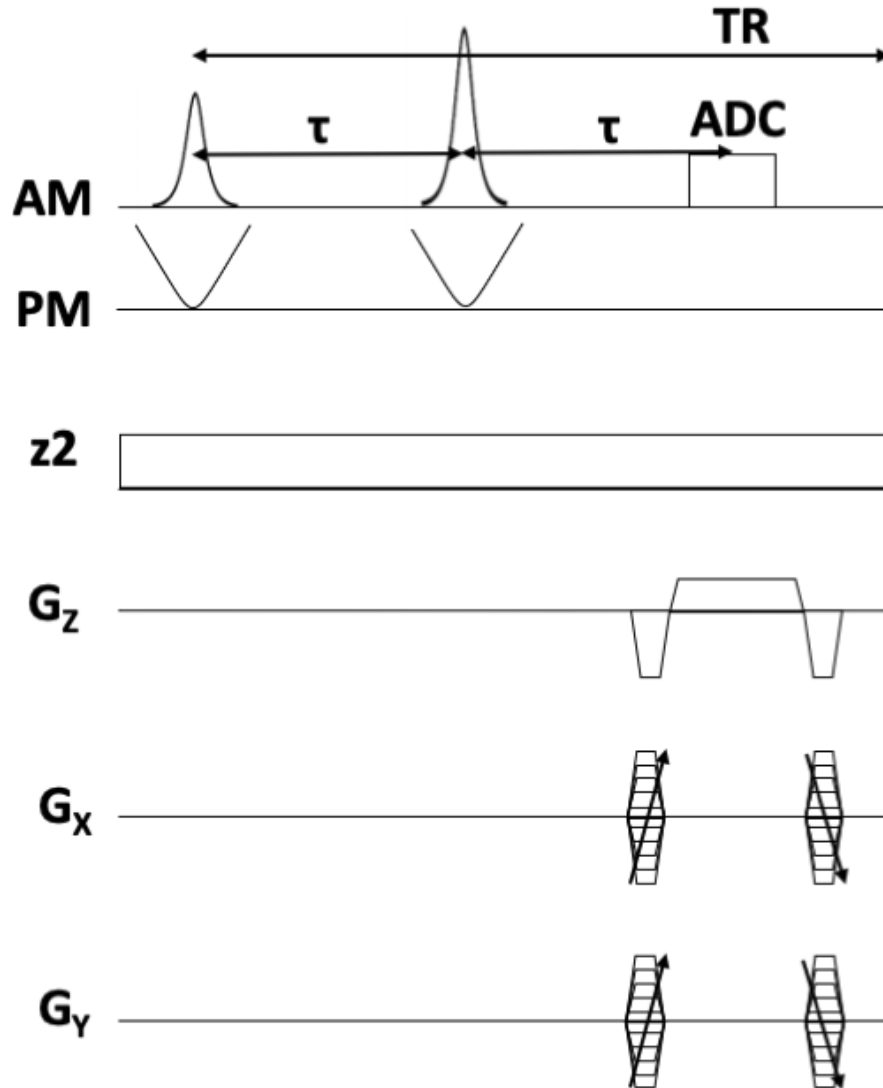
**Fig. 3.6.** Pulse sequence for exciting a circular region in the xy plane using a z2 shim. A phase-compensated spin-echo signal is produced in a circular region by applying two rapid passage pulses (in this case HS1 pulses) in the presence of a constant higher order gradient. The two pulses are identical, except for their RF amplitudes being set to produce $\pi/2$ and $\pi$ flip angles. The RF amplitude of the second pulse can be set higher than the adiabatic threshold level for achieving insensitivity to inhomogeneity.

contour lines corresponding to $\omega_c \pm BW/2$, where is the carrier frequency. The setting of $\omega_c$ determines the set of isofrequency contours excited by the pulse in physical space, and thus, the excitation profile. For example, consider the xy plane at $z = 0$. With no offset applied, the vertex of the bowl is located at magnet isocenter, with the frequency distribution decreasing quadratically in space. The RF pulse sequentially excites isofrequency contours until the lower limit of its BW is reached, resulting in a circular disk to be excited (Fig. 3.8 c). With a constant offset, the vertex is no longer located at the magnet isocenter and the position along the x- and y-axis corresponding to the lower limit of the bandwidth changes. As the offset approaches $BW/2$, some isofrequency contours are outside the range of frequencies excited, forming a hole or gap (Fig. 3.7 a,d).
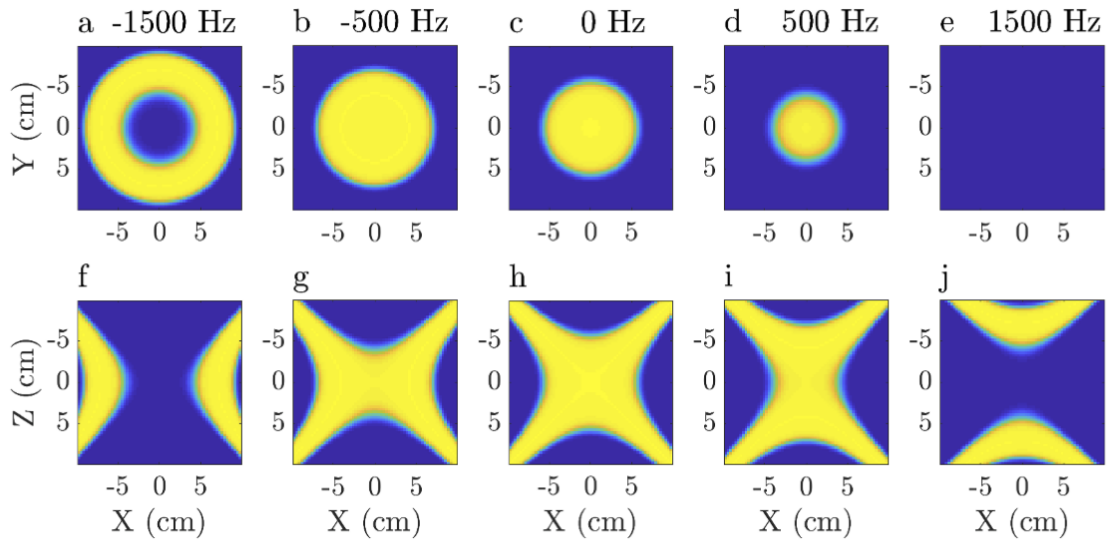


**Fig. 3.7.** Normalized transverse magnetization utilizing the z2 shim to excite a hyperboloid with five different constant offsets applied to the sequence shown in Fig. 3.6. The xy plane at $z = 0$ (a-e) shows the expansion and contraction as the bowl formed by the z2 shim is displaced. The xz plane at $y = 0$ (f-j) shows the saddle formed by the shim with the fingers extending out from the center forming the bowl along the xy plane. Subplots (a,e,f,j) show the regions of unexcited isochromats as the offset is larger than the BW of the RF pulse.

**Fig. 3.8.** The frequency distribution created by the z2 shim with five constant offsets applied. Contour plots showing 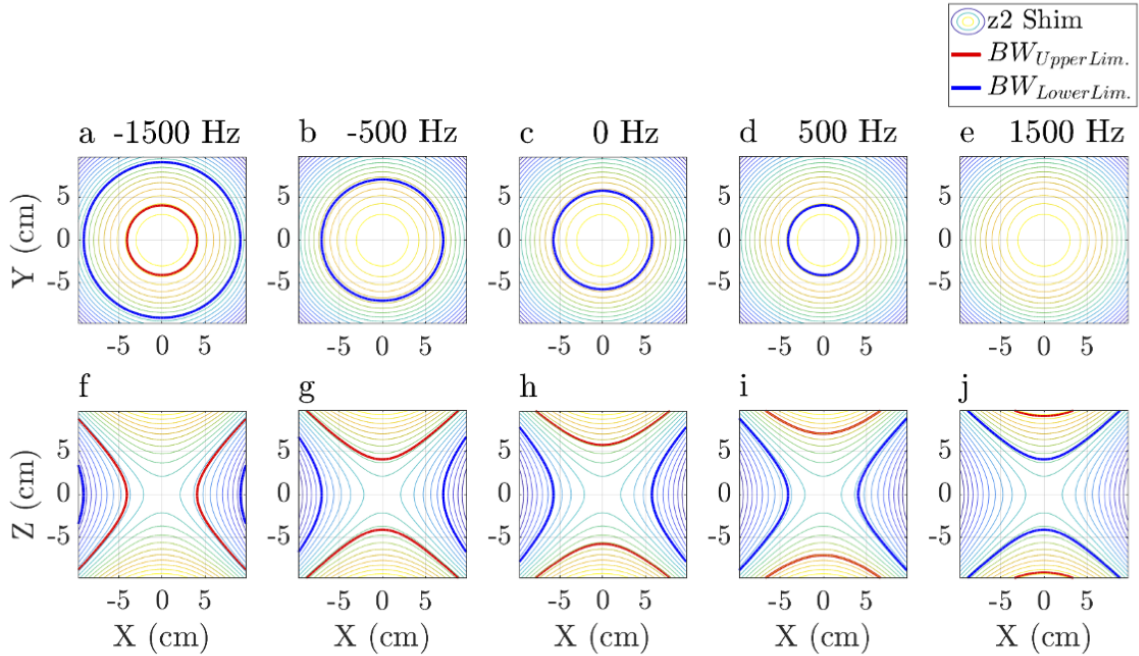the frequency distribution within the xy plane at $z = 0$ (a-e) and xz plane at $y = 0$ (f-j) are shown. To illustrate the region excited by the pulse, the upper and lower bandwidths of the pulse are drawn on the corresponding contour line. The pinching behavior is clearly visible in subplots (f-j) resulting in large regions of unexcited isochromats, contributing to the hole along the xy plane.

## 3.5   In Vivo Experiments

All experiments were performed with a Varian DirectDrive console (Agilent Technologies, Santa Clara, CA) interfaced with a 1.5T, 90 cm magnet (Oxford Magnet Technology, Oxfordshire, UK) and a clinical gradient system (model SC72, Siemens, Erlangen, Germany). Experimental verifications of the sequence were performed using the pulse parameters described in the simulations section. An IRB approved protocol was followed for human brain imaging of healthy volunteers after written, informed consent was obtained.

A T1-weighted 3D spin-echo sequence was created such that frequency-encoding

was along the z direction (the magnet bore) with phase encoding along x and y (the axial plane) to minimize distortions in the acquired image. To perform a T1-weighted spin-echo acquisition, the following sequence parameters were chosen: TR = 300 ms and TE = 19.2 ms, with readout bandwidth = 109 kHz. The flip angles were 135° and 180° to increase the steady-state longitudinal magnetization with the short TR and TE used. The 135° flip angle was chosen empirically to maximize SNR. The spatial resolution was 1.0 x 3.0 x 3.0 mm3 with FOV = 256 x 192 x 192 mm3. In order to create the higher order gradient necessary for the experiment, the coefficient of the standard z2 shim was fixed to approximately 30 Hz/cm2 across the desired 19.2-cm FOV for the duration of the sequence. To measure the applied z2 shim strength, a B0 map was generated by using data from a second acquisition performed with a 100 μs offset between the center of the spin and gradient echoes. Such a short offset was chosen due to the applied z2 shim, resulting in large frequency offsets within the brain.

The results show that it is possible to select a sharply demarcated volume shaped like a hyperboloid using only standard (linear) imaging gradients and a z2 shim (Fig. 3.9). The images show a circular region is selected in the axial plane, corresponding to z = 0, with minimal distortions. Considering the real and imaginary components, the signal intensity remains relatively invariant across both images, except at the extreme edges of the excited volume where the field from the z2 shim is steep (Fig. 3.9 a,d). Along the sagittal and coronal planes, the signal intensity pattern is more complex with banding occurring along the readout dimension (Fig. 3.9 (b,c,e,f)). These phenomena stem from the constant z2 shim applied throughout the imaging sequence. Further development in non-standard gradient hardware, like multi-coil gradient arrays [100], [101], show promise in being able to modulate a z2 field; thus eliminating the phase variation seen here. Further compensation of RF phase can be achieved by altering the parameters of the pulses, and several such methods have been presented in this work. In most cases however, the additional compensation possible with these methods can be realized only by increasing the minimum TE; which may be undesirable in T1-weighted spin-echo applications. For example, when using the conditions presented in reference [37] the minimum TE will be 1.5 times longer than that in the sequence proposed here. Moreover, in spin-echo applications
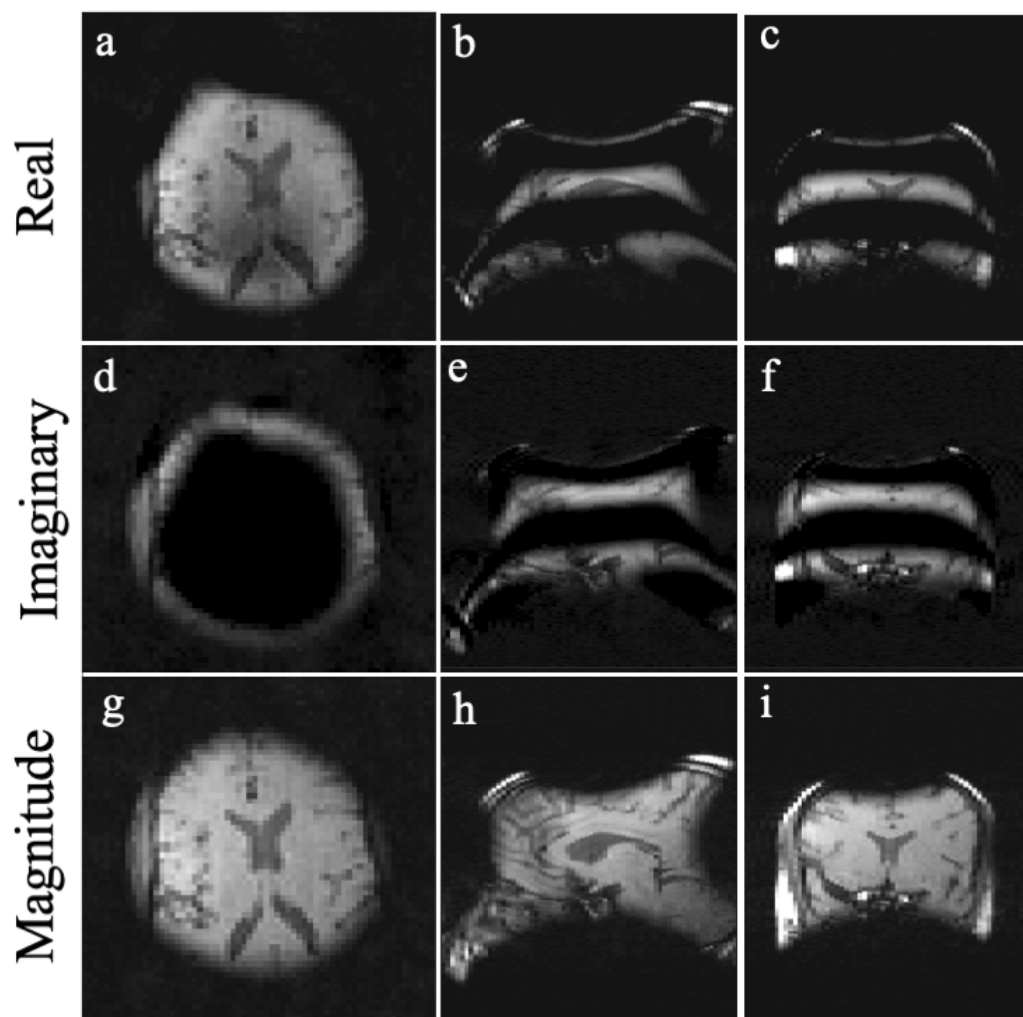
**Fig. 3.9.** Cross-sections of in vivo 3D MR images produced by selectively exciting a hyperboloid within a human brain using the sequence of Fig. 3.6. The axial views (a,d,g) have in-plane resolution of 3 mm2 (64 x 64 matrix), while the sagittal (b,e,h) and coronal (c,f,i) views have in-plane resolution of 1 mm x 3 mm (256 x 64 matrix). All slices shown are through iso-center. In the axial planes, which were acquired using 2D phase encoding, the signal intensity in the real component (a) is relatively invariant across the selected region; while the imaginary component (d) shows the greatest phase variation at the edge where the magnetic field change due to the z2 shim is steep. In the frequency-encoded (z) direction, the nonlinear field from the z2 shim causes phase variation in sagittal (b,e) and coronal (c,i) views not seen in the magnitude images (h,i).

requiring reduced field-of-view, comparable phase compensation would require using dual echoes in each spatial dimension, substantially increasing the minimum TE and SAR.

## 3.6  Conclusions

Methods and applications of FM pulses to attain resilience to nonuniform magnetic fields in MRI continue to expand. As discussed herein, FM pulses belonging to the rapid passage class of pulses, like HSn pulses, have the ability to produce a sharply demarcated baseband; and as such are optimal for slice- (or slab-) selective excitation and inversion. For many applications FM pulses can also be exploited to minimize multiple undesirable effects from $B_0$ inhomogeneity and chemical-shift displacement, which require the use of high bandwidth pulses.

A common misconception is that FM pulses usually deposit large amounts of RF energy (SAR); however, as predicted from theory and simulations, the SAR of rapid passage pulses is not significantly different from other pulses when comparing them at a given bandwidth. Moreover as compared to conventional AM pulses, FM pulses can produce a bandwidth of excitation or inversion that is much larger using a given amount of peak RF power.

Despite the advantages FM pulses provide, their widespread use has been slowed by the perceived disadvantage of the nonlinear phase created during excitation and refocusing. Historically, the nonlinear phase represented a loss in signal during acquisition, therefore FM pulses were generally avoided in standard MRI. To overcome this limitation, extensive work has been performed to develop different methods to remove or even exploit this nonlinear phase. Several of these methods have been presented in this article with techniques ranging from double spin echoes to sequences employing nonlinear gradients. These techniques allowed for further implementation of FM pulses on clinical systems where they have become a staple in some standard imaging protocols. There now exist a wide variety of shapes and classes of FM pulses to fulfill the demands of clinical MRI, with new FM pulses and applications continuing to emerge.

# Chapter 4

# Fast spin-echo approach for accelerated B1 gradient–based MRI

This chapter has been published as a manuscript in the journal Magnetic Resonance in Medicine [104] and selected for the ISMRM Young Investigator I.I. Rabi Award.

## 4.1 Introduction

Despite the tremendous advantages MRI provides, most of the global population lacks access due to the high costs to obtain, transport, and maintain the associated infrastructure of a conventional scanner. Recently, several different groups have focused on addressing inequities in MRI accessibility and its underutilization by developing new technology that reduces the overall cost and complexity of conventional imaging systems [2]–[4], [94]. One proposed method seeks to replace traditional $B_0$ gradients in favor of new radiofrequency (RF) based techniques to perform similar spatial encoding. The elimination of conventional $B_0$ gradients would provide several important advantages[2]–[4], [94], [105] while also decreasing the overall size and cost of a conventional scanner. Further improvements to the portability could be had by coupling

these new emerging radiofrequency imaging (RFI) techniques with scanners operating in the mid to low field strengths ($< 1.5$ T). After RFI was first demonstrated by Hoult in his cardinal work on rotating frame zeugmatography, several groups have expanded on his work to develop new imaging techniques like Transmit Array Spatial Encoding (TRASE)[28], Bloch-Siegert spatial encoding technique (BS-SET)[29], and $B_1$ selective techniques[30]–[33].

At these low fields, these RFI based techniques become significantly more viable as the specific absorption rate (SAR) constraints are reduced. Moreover, modeling of $B_1$ encoding fields for the purposes of conducting RFI techniques with array coils and parallel transmission (pTx) becomes more straightforward at lower fields, since the RF wavelength is long relative to the dimensions of the imaged object[28], [105]–[110]. The recently developed RFI technique called FREE (Frequency-modulated Rabi Encoded Echoes) improves upon previously developed RFI methods by providing robustness to resonance offset, which becomes increasingly problematic as MRI magnets are made more compact, due to increased $B_0$ inhomogeneity [107], [111]–[113]. FREE achieves resilience to $B_0$ inhomogeneity by exploiting a pair of frequency-modulated (FM) adiabatic full passage (AFP) pulses in a double spin echo configuration. By applying AFP pulses with a spatially-varying RF field, $B_1^+(r)$, FREE has shown that spatial information can be encoded within the bandwidth of the pulse, that is robust to resonance offsets. However, to encode spatial information, the original FREE technique utilized a multi-shot (MS) approach, much like conventional phase encoding, where one point of k-space was acquired per TR. Although this multi-shot approach provided proof of concept, FREE's clinical viability is lacking because acquisition times are long, and acceleration is not easily achievable.

In this work, we present a new multi-echo (ME) version of FREE with a fast spin echo (FSE) approach, where multiple echoes are collected during a single shot[114]. This new sequence leverages the acceleration of conventional FSE approaches, but eliminates the need for conventional $B_0$ gradients to perform phase-encoding. Simulations show that multiple echoes can be acquired during a single shot and produce comparable images to conventional FREE in a quarter of the time.

## 4.2 Theory

### 4.2.1 Background on FREE

The original article on FREE presented a multi-shot double spin echo (DSE) approach (Figure 4.1) in which the time-bandwidth products ($R = T_{\mathrm{p}} \cdot BW$) of the two AFP pulses were modulated in the presence of a spatially-varying RF transmit field, $B_1^+(r)$[113]. In this configuration, the initial spatially-varying phase created by the first pulse was partially refocused by the application of an additional pulse. By modulating the differences in the $R$ values of each respective pulse, an approximately linear spatial variation in the magnetization phase can be imprinted in the acquired echo. Acquiring an array of echoes in this manner was shown to be analogous to that of conventional phase encoding where one k-space point along the FREE dimension was acquired per shot. In principle any AFP pulse can be used to perform FREE, however the family of hyperbolic secant (HSn) pulses was chosen for their superior performance across large bandwidths and general widespread clinical use[22], [35], [36].
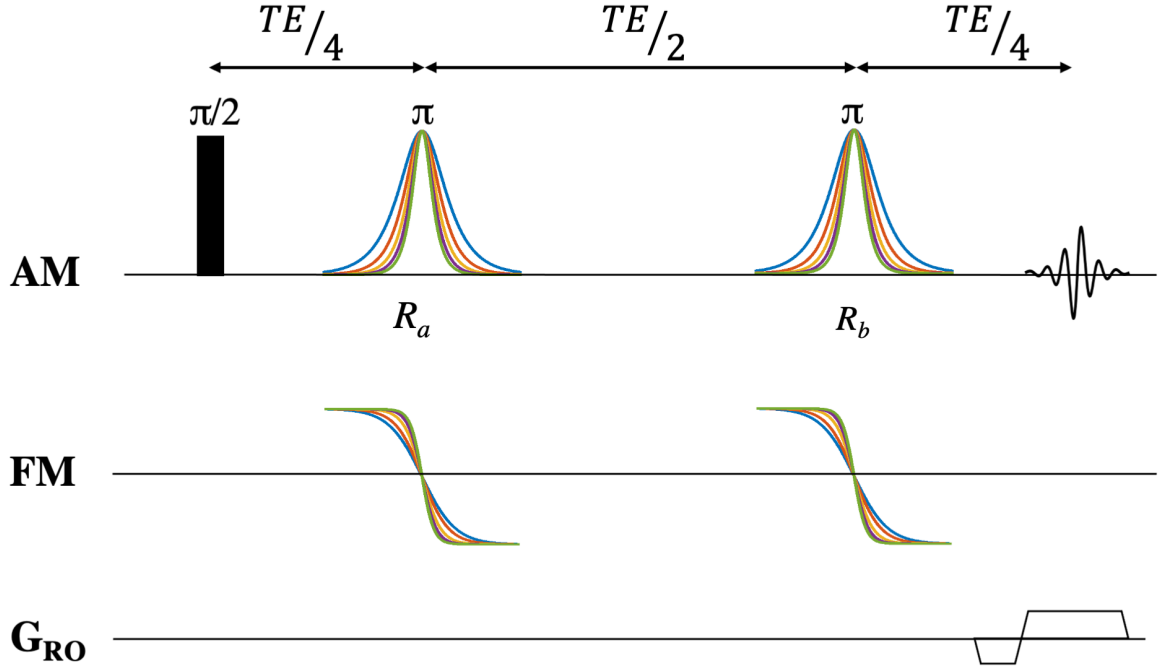
**Fig. 4.1.** Originally proposed multi-shot FREE sequence. Modulating the $R$ values of the two AFPs (denoted as $R_a$ and $R_b$) imprints an approximately linear phase in the resulting echo. This $B_1^+$-dependent phase was shown to be analogous to traditional phase encoding but can be achieved without the use of pulsed $B_0$ gradients. The initial excitation pulse can be any pulse such as adiabatic half passage, a square pulse, or a $B_1^+$-selective pulse, depending on the experimental setup.

Traditionally HSn pulses are described by their amplitude and frequency modulation functions (AM and FM, respectively). The AM and FM functions, in angular velocity, for any HSn pulse are written as

$$\omega_1(\tau, r) = \omega_1^{\max} \operatorname{sech}(\beta\tau^n) \tag{4.1}$$

$$\omega_{\mathrm{RF}}(\tau) = \omega_c + A \int \operatorname{sech}^2(\beta\tau^n)\mathrm{d}\tau \tag{4.2}$$

where $\omega_1^{max}$ is the peak spatially-varying Rabi frequency in $rad/s$; $\tau$ is the normalized pulse duration given by $\tau = 2\tau/T_{\mathrm{p}} - 1$, for $t \in [0, T_{\mathrm{p}}]$; $\omega_c$ is the center frequency of the frequency sweep; $A$ is the frequency-sweep cutoff in $rad/s$; $\beta$ is a unitless truncation

factor set such that $\mathrm{sech}(\beta) = 0.01$, and $n$ is the order of the HS pulse which controls the flatness of the AM function[35], [36].

From the rotating frame of reference, the bulk magnetization vector evolves about an effective field vector, $\mathbf{B}_{\mathrm{eff}}$, created by the time evolution of the applied AM and FM functions for a given pulse. The frequency vector around which the bulk magnetization evolves, $\omega_{\mathrm{eff}} = \gamma \mathbf{B}_{\mathrm{eff}}$, is assumed to be constant across space, only varying in time. However, by introducing a spatially-varying $B_1^+$, this is no longer the case. To capture this behavior the equation for the effective field becomes

$$\omega_{\mathrm{eff}}(\tau, r) = \omega_1^{\mathrm{max}}(\tau, r)\hat{\mathbf{x}}' + (\omega_{\mathrm{RF}}(\tau) - \omega_c)\hat{\mathbf{z}}' \tag{4.3}$$

Thus, at the end of an applied pulse, the spatially-dependent phase accrued is given by

$$\Psi(r) = \pm \frac{T_{\mathrm{p}}}{2} \int_{-1}^{1} \|\omega_{\mathrm{eff}}(\tau, r)\| \mathrm{d}\tau \tag{4.4}$$

where the sign is determined by the direction of applied frequency sweep. In practice, $\omega_{\mathrm{eff}}$ must be evaluated numerically, especially for higher order HS pulses. For the previous MS-FREE sequence, the net phase can be expressed as the difference of the resulting phase produced by each AFP pulse,

$$\Delta\Psi(r) = \frac{T_{\mathrm{p},b}}{2} \int_{-1}^{1} \|\omega_{\mathrm{eff},b}(\tau, r)\| \mathrm{d}\tau - \frac{T_{\mathrm{p},a}}{2} \int_{-1}^{1} \|\omega_{\mathrm{eff},a}(\tau, r)\| \mathrm{d}\tau \tag{4.5}$$

This framework can be extended to analyze any FREE type of sequence including a new multi-echo type sequence.

## 4.2.2 New Multi-Echo FREE sequence

To increase the clinical practicality of the previously described FREE sequence, a new accelerated multi-echo version is presented herein. This new sequence has its foundations in traditional FSE, but replaces the conventional phase encoding gradients with new RF-based gradients. To achieve this acceleration, the proposed sequence modifies the MS-FREE with the addition of alternating AFP pulses to

augment the phase of later echoes approximately linearly, thus acquiring new points in k-space.

There are several different pulse modulation schemes that can be employed to encode spatial information in FREE-type sequences. The different modulation schemes determine how and when different parts of k-space are sampled during an imaging experiment and are typically chosen such that the center of k-space is sampled during the middle of an acquisition.

To minimize the extent to which large $R$-valued pulses are used, the encoding scheme proposed for the new ME sequence employs a multi-shot, inwards-outwards sampling pattern to acquire both halves of k-space (Figure 4.2). The ME-FREE sequence is different from conventional FSE in that both halves of k-space are simultaneously sampled during each shot. This is accomplished by reversing the frequency sweep direction of the AFPs, during both the echo train and the pair of initial pulses. As the sweep direction is modulated, the sampled k-space points flip about $k = 0$, analogous to performing the complex conjugate. In the simplest case when only acquiring one echo, the sweep direction of the initial pair of AFPs controls the side of k-space that is sampled during subsequent shots. Positive and negative k-space steps are denoted by superscript FM* and FM, respectively.
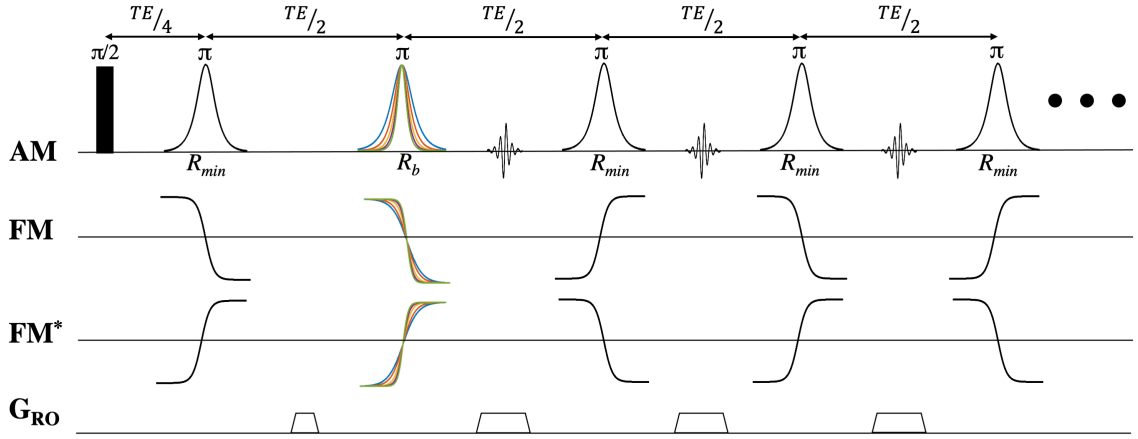
**Fig. 4.2.** Proposed multi-echo FREE sequence. The sequence only requires a standard $B_0$ gradient along the frequency-encoding dimension ($G_{RO}$). By having a spatially varying $B_1^+$ along an orthogonal dimension, a 2D image can be acquired. The phase difference created between the first pair of pulses ($R_b$ and $R_{min}$) controls the initial step size in k-space with the additional pulses adding a constant phase to further incrementally step in k-space. FM and FM* control the direction of the first step in k-space, where alternating the FM sweep direction during the echo train flips the sign of the acquired k-space point, like performing the complex conjugate.

In the proposed sequence, the center of k-space is acquired early in the imaging experiment with further k-space points being collected during the echo train. As with MS-FREE, the center of k-space corresponds to when the initial pair of AFP pulses have equal $R$ values and therefore refocuses any residual phase present in the subsequently formed echo. Building from this idea, the application of additional AFP pulses in a train can be used to further modulate the phase of subsequent echoes in a manner that is akin to FSE-type sequences. It is important to note that this type of approach allows for flexible control of when the center of k-space is sampled. This is accomplished by altering the modulation scheme of the first two AFPs in such a way that they achieve equal $R$ values during a later echo.

To control the amount of phase added to each echo and still maintain relatively small $R$-valued pulses, the train is comprised of AFPs of value $R_{min}$, but with alternating signs of the FM functions. By changing the direction of the frequency sweep throughout the train any additional pulses beyond the initial pair can add a fixed amount of phase. This added phase is proportional to the echo number and the

spatially-dependent phase produced by the shortest pulse, equivalent to $R_{min}$.

As the first pair of pulses continue to modulate, the initial phase is changed by $\Delta R \ (= \Delta T_{\mathrm{p}} \cdot BW)$, but the jumps produced by the train of AFPs remain constant, and thus, the gaps in k-space are filled. To prevent double sampling, $R_{max}$ must not exceed $2 \cdot R_{min}$ and $\Delta R$ must be set such that $\Delta R = \frac{R_{min}}{N_{Shots}}$. Upon combining these expressions, it can be seen that $R_{max} = 2 \cdot R_{min} - \Delta R$.

## 4.2.3 Analyzing Encoding of ME-FREE

To better understand the unique trajectory of the ME-FREE sequence and allow for the calculation of conventional imaging parameters, the previously described equations for FREE need to be modified to account for the additional phase imparted by the pulses during the echo train. Starting with Eq. 4.5, the phase difference between two AFPs can be extended to describe the sequence shown in Figure 4.2 with the net phase being a function of the modulated AFP pulse, $b$, and the echo number,

$$
\Delta\psi_{MultiEcho}(b, m_{Echo}, r) =
$$
$$
(\frac{T_{\mathrm{p},b}}{2} \int_{-1}^{1} \|\omega_{\mathrm{eff},b}(\tau, r)\| \mathrm{d}\tau - \frac{T_{\mathrm{p},min}}{2} \int_{-1}^{1} \|\omega_{\mathrm{eff},min}(\tau, r)\| \mathrm{d}\tau)
$$
$$
+ (m_{Echo} - 1)(\frac{T_{\mathrm{p},min}}{2} \int_{-1}^{1} \|\omega_{\mathrm{eff},min}(\tau, r)\| \mathrm{d}\tau)
$$

$$(4.6)$$

In this equation, $T_{\mathrm{p},b}$ corresponds to the pulse duration of the modulating pulse, $T_{\mathrm{p},min}$ and $\omega_{\mathrm{eff},min}$ refer to the minimum pulse duration and corresponding phase produced by said pulse, respectively, $m_{Echo}$ corresponds to the echo number such that $m_{Echo} \in [1, N]$, and $N$ is the total number of acquired echoes. Any number of acquired echoes greater than 0 is valid, and the equation above then simplifies down to MS-FREE when only one echo is acquired.

This equation describes the phase variation between corresponding shots and echoes as a function of space and thus is analogous to the conventional phase encoding term produced by the dot product of a given k-space trajectory with space. The

partial derivative with respect to space thus yields an equation that describes the k-space behavior of the ME-FREE sequence. Eq 4.6 and its subsequent derivatives form a powerful tool to analyze the encoding schemes produced by not only the ME-FREE sequence but any FREE sequence that relies on the phase difference produced by AFPs. The previously described filling order becomes clear when using these equations to model a 1D ME-FREE sequence comprised of four shots and acquiring three echoes per shots (Figure 4.3). The pulses chosen for simulation were: $AFPs = HS4$, $BW = 2kHz$, $R_{min} = 30$, $R_{max} = 52.5$, and $\Delta R = 7.5$. The non-ideal $B_1^+$ gradient of a single-loop surface coil was used to model the spatially-varying $B_1^+(r)$. The results show the effective acquisition order of k-space as the number of shots increases with three echoes acquired.
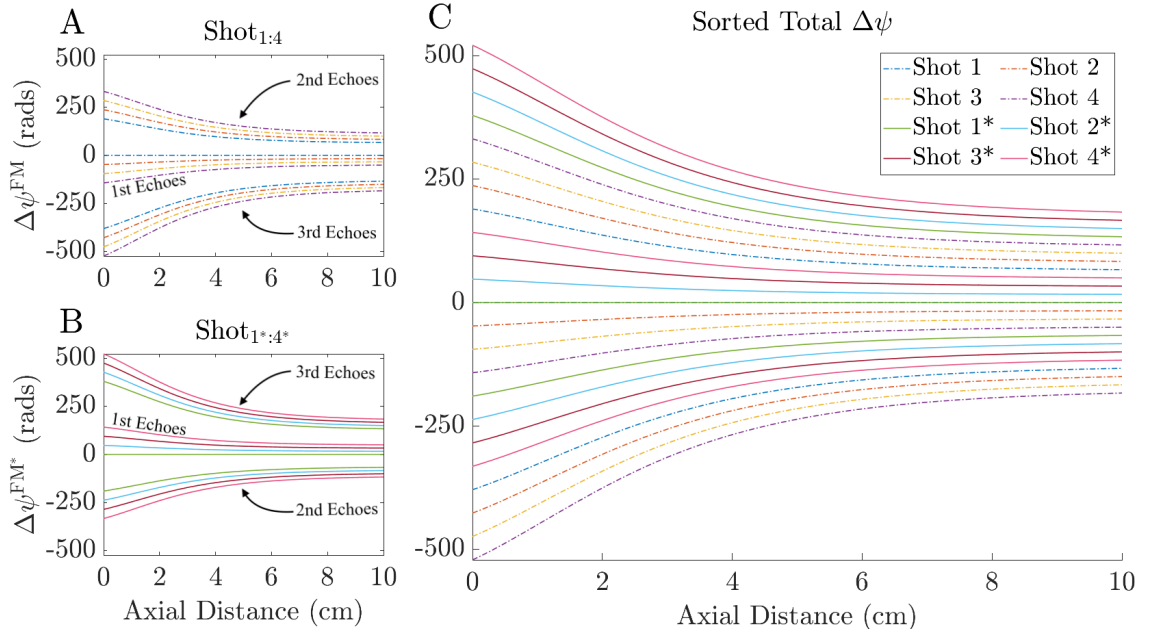
**Fig. 4.3.** To conceptualize k-space filling, plots show the spatial-dependence of the phase modulation in an 8-shot ME-FREE experiment, as implemented with a simple surface coil. The asterisks (*) denotes negative (complex conjugate) k-space. Three echoes are acquired per shot. To capture positive and negative k-space data the initial pair of AFPs are implemented with positive (A) or negative (B) frequency sweep directions, respectively. The initial pair of AFP in shots 1 and 1* have matching R values and thus perfectly refocus any phase in the first echo, corresponding to $k = 0$. The phase changes in the remaining echoes (each of which is produced by a single AFP pulse) by a fixed amount, $m_{Echo} \cdot \psi(r)$. In shots 2-4 and 2*- 4*, the absolute difference In R value increases between the initial pair of pulses, and thus the first echo steps away from $k = 0$ while the phase spacing between the remaining 2 echoes remains constant, although alternating in sign. It can be seen that as the k-space data from the different shots are combined the gaps in k-space are filled. The spatially-dependent $B_1^+$ on the axis of a realistic 10-cm surface coil was obtained from a CST simulation.

A byproduct of utilizing a train of AFPs is that the direction of the jump in k-space alternates between positive and negative values, depending on the step direction of the initial pair of pulses. Thus, to properly reconstruct an image the corresponding echoes must be sorted into their appropriate locations (Figure 4.3). These simulations show that the multi-echo FREE sequence can uniformly cover k-space

by incorporating traditional FSE techniques, but also illustrate possible methods to further accelerate image acquisitions. That is, by employing multiple receive coils, k-space could be under-sampled and reconstructed using conventional parallel imaging techniques[115]–[117].

## 4.3   Methods

### 4.3.1   Simulations of the Multi-Echo FREE sequence

To test the performance of the sequence, a Julia[118] based Bloch simulator was developed to study the 2D spin dynamics during the multi-echo FREE experiment. A grid of $512^2$ isochromats was initially considered with a sub-voxel averaging factor of 4 to give an effective grid of $128^2$ isochromats. It was assumed that a perfect $\pi/2$ excitation was initially applied to place all isochromats onto the transverse plane. To create a spatially-varying $B_1^+$, a 2D model of a single-loop, 10-cm elliptical surface coil with $\omega_1^{max}/2\pi\ (r_{min}) = 2.5$ kHz and $\omega_1^{max}/2\pi\ (r_{max}) = 0.2$ kHz was simulated using the commercial simulation package CST studio suite (Dassault Systèmes, Vélizy-Villacoublay, France), with a human equivalent phantom for 1.5 T [119]. This provided not only the spatially-varying $B_1^+$ but allowed for the quantification of the SAR. It was determined that, for this coil, 1 W of average input power had a maximum SAR 10-g volume of 1.71 W/kg. Several different simulations were performed utilizing HS4 pulses with varied parameters to adjust the adiabaticity of the pulses in the sequence (Figure 4.4). Three additional simulations were performed to investigate the effects of localized chemical shift and resonance offsets on the acquired images. These simulations utilized the same pulse parameters as in Figure 4.4D, except the first simulation had a 550 Hz offset added to the central lobes of the Shepp-Logan phantom to model the interaction between water and fat (Figure 4.5C), and a second simulation had constant resonance offsets added varying linearly between +/- 550 Hz in the y-direction (Figures 4.5D).
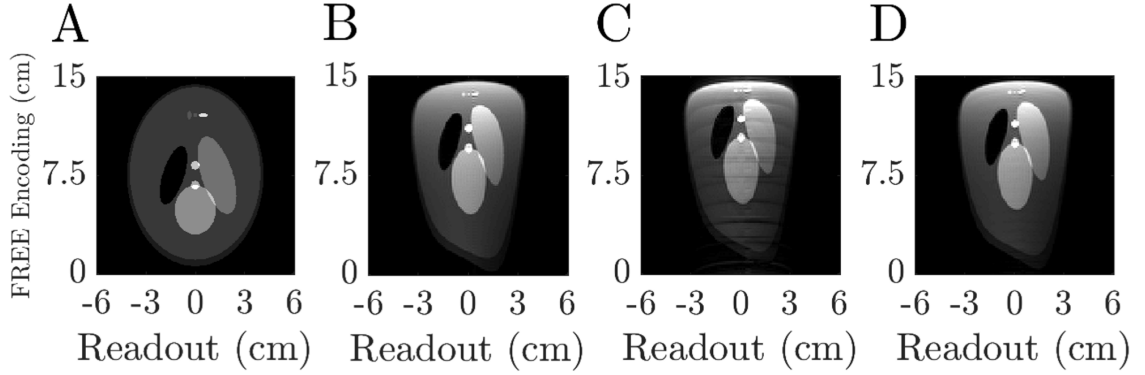
**Fig. 4.4.** Simulations of the ME-FREE sequence. A) The simulated object is the Shepp-Logan phantom. B) Simulation using the propagator previously described in Torres et al., which assumes the AFP pulses are fully adiabatic and thus each produces a perfect rotation about the effective field, $\omega_{\mathbf{eff}}$. C) A full Bloch simulation of the pulse sequence with a spatially-varying $B_1^+(r)$ transmit field and imperfect AFPs. The pulse parameters used in B) and C) were 10 shots, 6 echoes, $R_{min} = 35$, $R_{max} = 66.5$, $\Delta R = 3.5$, $BW = 4$ kHz. D) Using the same full Bloch simulation as for C), but with pulses that satisfied the adiabatic condition at a smaller $B_1^+$, while maintaining the same FOV. The parameters used for the simulation of improved adiabaticity pulses were: 20 shots, 3 echoes, $R_{min} = 30$, $R_{max} = 58.5$, $\Delta R = 1.5$, $BW = 2$ kHz. All simulations assumed a perfect $\pi/2$ excitation and utilized the same CST coil model for a single-loop, 10-cm elliptical surface coil with $\omega_1^{max}/2\pi$ $(r_{min}) = 2.5$ kHz and $\omega_1^{max}/2\pi$ $(r_{max}) = 0.2$ kHz and HS4 pulses. A standard frequency-encoding gradient was used along the readout direction. The image distortion resulting from the nonlinear $B_1^+$ gradient of the surface coil is apparent when comparing the original object (A) to the ME-FREE images (B-D). The importance of satisfying the adiabatic condition throughout the region of interest can be seen by comparing C) and D).
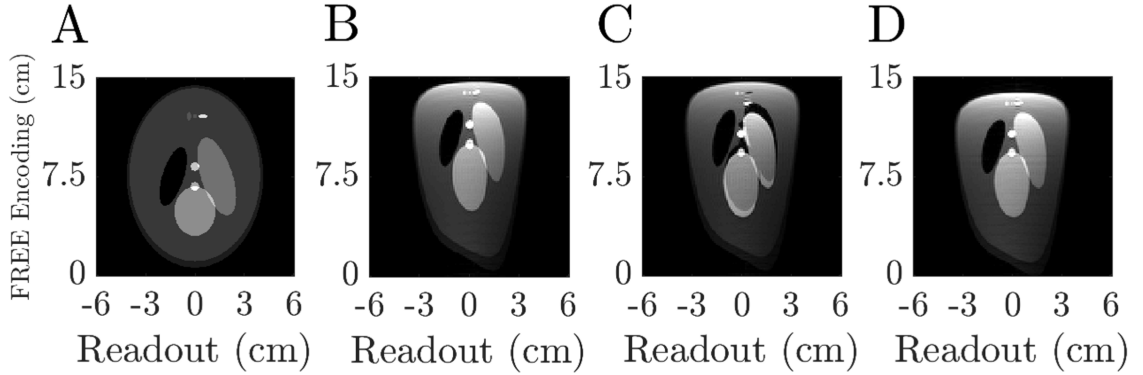
**Fig. 4.5.** Effect of various offsets on ME-FREE. A) The simulated object is the Shepp-Logan phantom. B) A full Bloch simulation of the pulse sequence with a spatially-varying $B_1^+(r)$ transmit field without the presence of any offsets. C) A localized resonance offset of 500 Hz was applied to the central lobes of the Shepp-Logan phantom to investigate the effect of different chemical-shifts in a object. D) A linearly varying resonance offset between +/- 500 Hz was applied across the object in the vertical direction. The pulse parameters for all simulations were identical to those used in Figure 4.4D, i.e. 20 shots, 3 echoes, $R_{min} = 30$, $R_{max} = 58.5$, $\Delta R = 1.5$, $BW = 2\text{kHz}$. All simulations assumed a perfect $\pi/2$ excitation and utilized the same CST coil model for a single-loop, 10-cm elliptical surface coil with $\omega_1^{max}/2\pi \left(r_{min}\right) = 2.5$ kHz and $\omega_1^{max}/2\pi \left(r_{max}\right) = 0.2$ kHz and HS4 pulses. A standard frequency-encoding gradient was used along the readout direction.

All simulations utilized a standard frequency-encoding gradient along the x-direction and were reconstructed using a fast Fourier transformation. To determine the imaging parameters of the simulation sequence, Eq. 4.6 was numerically evaluated, and its derivative was calculated to determine the FOV and pixel resolution along the ME-FREE encoding dimension which varies due to the nonlinear $B_1^+$ gradient of the surface coil (Figure 4.6).
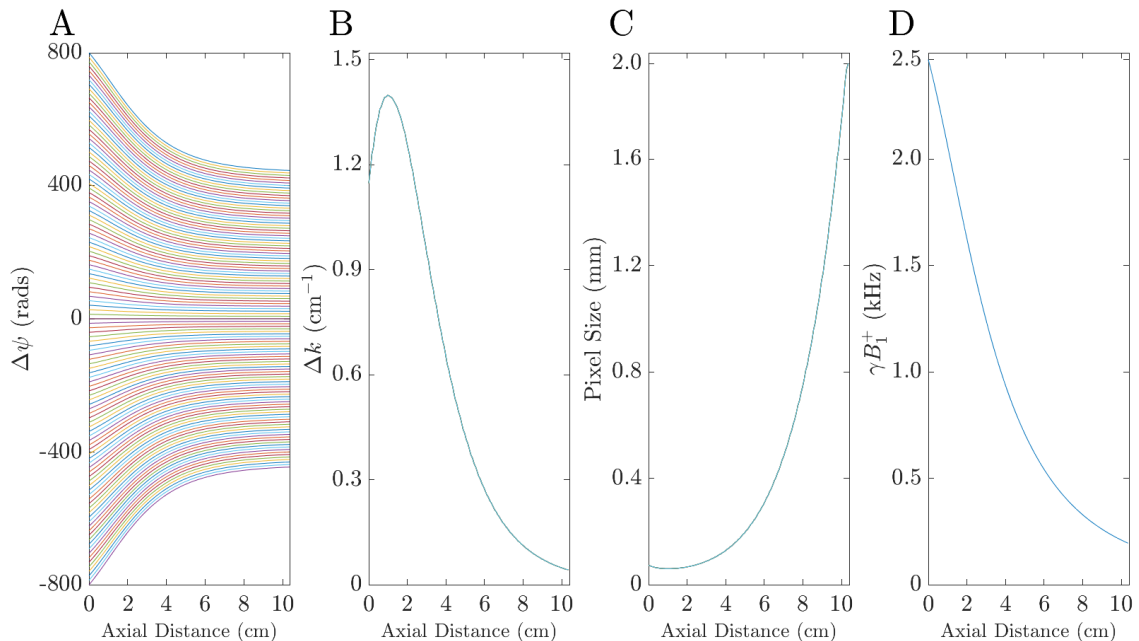
**Fig. 4.6.** Imaging conditions used in the simulation of the ME-FREE sequence utilizing HS4s. A) The total $\Delta\psi$ coverage after sorting and combining all the echoes. B) and C) The spatially-varying $\Delta k$ and the variability in resolution along the central vertical axis of the image. D) The $B_1^+$ transmit profile along the center axis of the coil. There is some inherent nonlinear encoding in the ME-FREE method, but it is heavily dominated by the nonlinear spatial variation of the surface coil used in the simulation. Pulse parameters were: 10 shots, 6 echoes, $R_{min} = 35$, $R_{max} = 66.5$, $\Delta R = 3.5$, $BW = 4$ kHz, and $AFPs =$ HS4. The $B_1^+$ transmit profile was generated using a CST simulation of a 10-cm single loop, elliptical surface coil such that $\omega_1^{max}/2\pi$ $(r_{min}) = 2.5$ kHz and $\omega_1^{max}/2\pi$ $(r_{max}) = 0.2$ kHz.

The simulations of the ME-FREE sequence illustrate the importance of satisfying the adiabatic condition throughout the regions of interest. The propagator-based simulation revealed that the proposed sequence would encode unique spatial information along the y-dimension, but this approach assumes perfect AFPs throughout the imaging volume and therefore includes no artifacts from the non-adiabatic regions of the $B_1^+$ field created by the surface coil. In the more realistic Bloch simulation, isochromats that experience non-ideal adiabatic conditions undergo a position-dependent flip angle that can lead to unique coherence pathways in later echoes. These simulations also illustrate the variable pixel resolution as a function of the axial distance from

the coil, with micron level spatial resolution occurring closer to the coil as compared to significantly larger pixels at depth.

## 4.3.2  In-Vivo Validation of the ME-FREE sequence

Data was acquired with a flexible CIERMag digital magnetic resonance spectrometer (DMRS)[120], configured for eight transmit and receive (Tx/Rx) channels. Each Tx channel can perform AM modulation in a four-quadrants approach with amplitude dynamics of 16 bits, along with FM (24 bits - 0.373 Hz resolution) and phase-modulation (PM) (14 bits - 0.088° resolution) capabilities. This DMRS was interfaced to a 1.5 T, 90-cm magnet (Oxford Magnet Technology, Oxfordshire, UK) with a clinical gradient system (model SC72, Siemens, Erlangen, Germany). The DMRS software was created and controlled by Python Magnetic Resonance Framework (PyMr), and the system has a specialized IDE (Integrated Development Environment) and ToRM-Console for creating MR sequences [121]–[125]. The magnet was initially designed to operate at 4 T, but was ramped down to 1.5 T without adjusting the passive shims of the system, leaving a relatively nonuniform $B_0$.

A single-loop elliptical surface coil with a major axis diameter of 9.65 cm and a minor axis diameter of 9.55 cm was utilized to create the spatially-varying RF fields necessary for all in-vivo imaging experiments. A protocol approved by the institution's institutional review board for imaging of healthy volunteers was followed, including obtaining written informed consent. Approximately 2.5 cm of thick padding was placed between the subject's head and the surface coil to reduce localized SAR and provide patient comfort. A $B_1^+$ map was acquired using the double angle approach from two phase encoded DSE images[126]. The power of the initial excitation pulse was doubled between the images to allow calculation of the flip angles and corresponding $B_1^+$ map. It was determined that the peak value of $\omega_1^{max}/2\pi$ was 6 kHz corresponding to the posterior edge of the brain.

A modified ME-FREE sequence was created that utilized HS4 pulses to acquire 4 echoes per shot (Figure 4.7). In total, 34 shots were collected to fully sample k-space with 18 shots per initial FM sweep direction, including 2 additional dummy shots. To improve the phase stability around $k = 0$, the acquisition scheme was

modified to begin at $k = \pm 1$ by increasing the $R$ value of the first AFP pulse to $R_{min} + \Delta R$. Averaging of the three redundant k-space points was performed in post processing. The $R$ values used were incremented from $R_{min} = 10$ to $R_{max} = 19.375$ with $\Delta R = 0.625$. All pulses had a $BW$ of 3.5 kHz and the FOV was set to 7 cm by numerically evaluating Eq. 4.6 with the known $B_1^+$ map. An undistorted ME-FREE image was generated via a coordinate transform and Jacobian scaling approach[38] that utilized the acquired $B_1^+$ map and Eq. 4.6 (Figure 4.8).
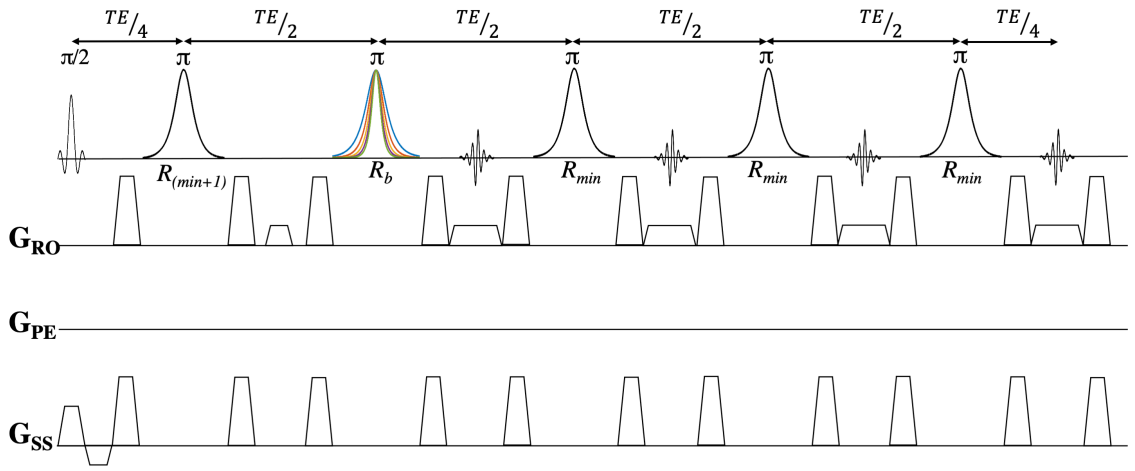


**Fig. 4.7.** ME-FREE imaging sequences used for in-vivo imaging. Shown is a single shot in which 4 echoes are collected. The sequence begins at $k = \pm 1$, depending on the sign of the frequency sweeps (not shown). No gradients were utilized along the phase-encoding dimension, instead the phase was augmented by the combination of a spatially-varying $B_1^+$ transmit field and the time-bandwidth products of the AFPs. As the magnitude of $R_b$ increases from $R_{min}$ to $R_{max}$ (as indicated by the different durations of the second AFP pulse in the sequence), the initial k-space point shifts from negative to positive crossing $k = 0$ during the second shot. Pulse parameters were: 16 shots, 4 echoes, $R_{min} = 10$, $R_{max} = 19.375$, $\Delta R = 0.625$, $BW = 3.5$ kHz, and $AFPs =$ HS4. The $B_1^+$ transmit profile was created by a 10-cm elliptical surface coil such that $\omega_1^{max}/2\pi(r_{min}) \approx 7.4$ kHz at the scalp.
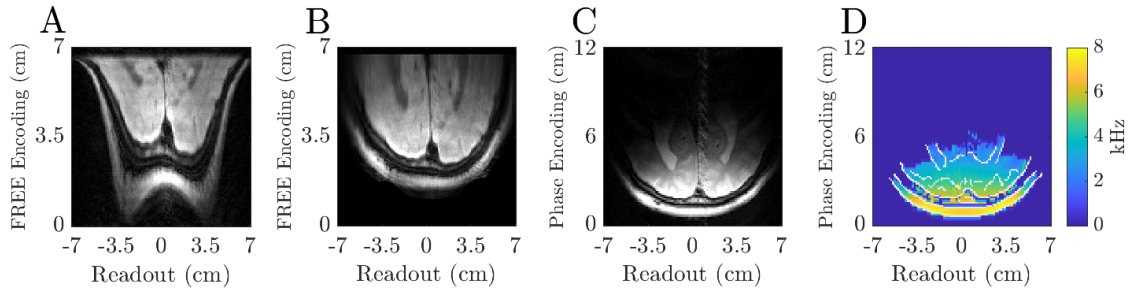
**Fig. 4.8.** ME-FREE utilizing the modified sequence as described in Figure 4.7. A) Multi-echo FREE image with FREE $B_1^+$ phase encoding performed along the y-direction. The image was reconstructed using standard FFT after the k-space data were sorted. B) A distortion corrected ME-FREE image utilizing a coordinate transform and Jacobian scaling type approach. C) A conventional DSE image acquired with $B_0$ phase-encoding gradients. D) $B_1^+$ map acquired using the double angle method from two conventional DSE images. The outline of prominent structures in the brain was overlaid on the $B_1^+$ map to give a better sense of the spatial variation across the brain. Pulse parameters for the sequences were: ME-FREE with 16 shots, 4 echoes, $R_{min}$ of 10 to $R_{max}$ of 19.375, and a FOV of 7 by 14 cm. The DSE used a matching pair of AFP pulses having $R = 10$ and a FOV of 12 by 14 cm. Both sequences used pulses with a fixed $BW = 3.5$ kHz, and $AFPs = $ HS4. The $B_1^+$ transmit profile was created by a 10-cm elliptical surface coil such that $\omega_1^{max}/2\pi(r_{min}) = 6$ kHz at the posterior edge of the brain.

For comparison a conventional DSE image was acquired using traditional phase encoding techniques and AFP pulses with a fixed $R$ value of 10. Both DSE and ME-FREE utilized a 1-ms 5-lobe sinc pulse to select a 4.5-mm axial slice. All sequences utilized a readout bandwidth of 80 kHz, an acquisition duration of 1.6 ms, and a $TE/4 = 9.25$ ms. All ME-FREE images were acquired with a matrix size of 125 by 128 with a FOV of 7 by 14 cm. No additional filtering was done to the sampled k-space prior to reconstruction. To study the different types of contrast possible with the ME-FREE sequence, three different TR values were used (2.5, 4.5, and 5.5 s) and an inversion pulse was added to create a FLAIR-type sequence[127] (Figure 9). The FLAIR sequence had $TR = 10$ s, $TI = 2.8$ s, and an HS4 pulse ($R = 10$, $BW = 3.5$ kHz) was used to perform the inversion. All other pulse parameters were fixed between sequences.

## 4.4 Results

### 4.4.1 Results of In-Vivo Multi-Echo FREE Sequence

In contrast to the previously described simulations, all the imaging experiments were performed with a slice-selective sinc pulse transmitted with the surface coil to select a 4.5-mm axial slice through the visual cortex of a healthy human brain. The acquired ME-FREE images utilized the spatially-varying $B_1^+$ of the surface coil to encode spatial information along the y-direction; thus, allowing for the removal of conventional $B_0$ gradients along that dimension. Distortions arising from the use of a nonlinear $B_1^+$- gradient are illustrated in a comparison of an undistorted ME-FREE image and a DSE image acquired using conventional phase encoding gradients (Figure 4.8A,C). Using the acquired $B_1^+$ map and Eq. 4.6, an undistorted ME-FREE image was generated illustrating that the distortions arising from the use of a nonlinear $B_1^+$- gradient can be corrected (Figure 4.8 B).
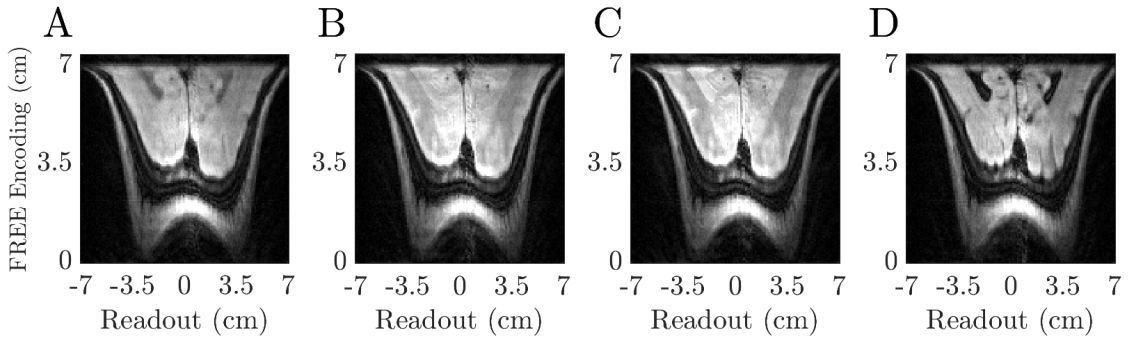


**Fig. 4.9.** A demonstration of creating different contrasts with ME-FREE. Imaging utilized the same pulses and $B_1^+$ as in Figure 4.8 but with various $TR$ values and slight modifications to collect different types of contrast. All images have a matrix size of 125x128 (FREE x RO). A) $TR = 2.5$ s, average power delivered $= 2.9$ W, and total duration $= 1.5$ min. B) $TR = 4.5$ s, average power delivered $= 1.6$ W, and total duration $= 2.7$ min. C) $TR = 5.5$ s, average power delivered $= 1.3$ W, and total duration $= 3.3$ min. D) FLAIR image with a $TR = 10$ s and $TI = 2.8$ s, average power delivered $= 0.8$ W, and total duration of 6 min. As the $TR$ increases, the contrast gradually shifted to a more T2-weighted image with the ventricles transitioning from dark to bright with each progressive image. With the addition of an inversion pulse to nullify CSF signal, a T2 FLAIR image can be readily acquired using this approach.

Several additional images were acquired to study the different types of contrast achievable with the ME-FREE approach. All pulse parameters were held constant between images, but $TR$ was increased from 2.5 s to 5.5 s (Figure 4.9 A-C). With the increase in $TR$, the contrast gradually shifted to a more T2-weighted image with the ventricles transitioning from dark to bright with each progressive image. With the addition of an inversion pulse to nullify CSF signal, the ability to acquire a T2-FLAIR image with ME-FREE was also demonstrated (Figure 4.9D).
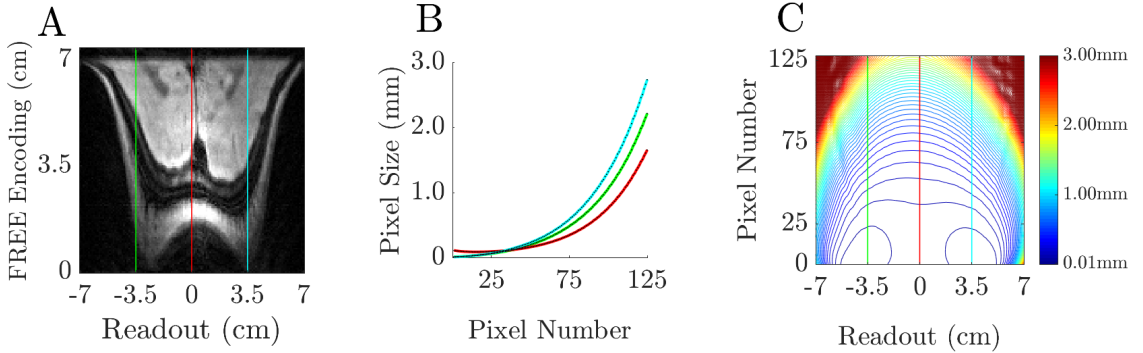


**Fig. 4.10.** Analysis of variable resolution. Using the framework presented in this work, a detailed analysis of the spatial variation of the pixel size was simulated for the ME-FREE image in Figure 4.8A. A) The three regions of interest correspond to the horns and along the central axis of the coil. B) Plots showing how the horns correspond to regions of very fine spatial resolution, dropping down to 10 $\mu$m in regions very close to the coil. As the axial distance from the coil increases, the resolution degrades following the inverse of the $B_1^+$ transmit field. C) A 2D contour plot showing the regions of constant resolution. At depth, the resolution continues to degrade as the transmit field drops off to infinity but any signals from these regions will be collapsed into a few pixels, resulting in a hyperintense signal at the edge of the reconstructed object. The pulse parameters: 16 shots, 4 echoes, $R_{min} = 10$, $R_{max} = 19.375$, $\Delta R = 0.625$, $BW = 3.5$ kHz, and $AFPs =$ HS4. The $B_1^+$ transmit profile was created by a 10-cm elliptical surface coil such that $\omega_1^{max}/2\pi$ was $\approx 7.4$ kHz at the scalp.

To further study the variable resolution of the ME-FREE image (Figure 4.10), Eq. 4.6 was evaluated using the CST generated $B_1^+$ map and pulse parameters from Figure 4.8. By comparing three traces through the resulting image, two in regions of very steep $B_1^+$ gradients and one along the center axis of the coil, the variable

resolution becomes obvious. The characteristic horns in the ME-FREE as well as in the original MS-FREE images correspond to regions of very steep $B_1^+$ gradients and thus regions of very high resolution in the y-direction[113].

## 4.5    Discussion

The multi-echo FREE sequence presented in this work has demonstrated the capability of not only eliminating a pulsed $B_0$ gradient but represents an improvement of the original FREE technique without compromising on its established advantages. At their core, all current FREE sequences rely on the unique properties of AFPs to achieve a spatially uniform inversion that can be exploited to encode spatial information. Broadband AFPs that satisfy the adiabatic condition can achieve inversion up to the bandwidth of the pulse, and thus, provide robustness to nonuniform $B_0$.

As expected, the sequence behaves optimally when the AFPs are operated fully within the adiabatic regime. From simulations utilizing ideal AFPs, no artifacts are present in the resulting image from the nonadiabatic regions of the transmit field. However, when considering non-ideal AFPs, as used in the Bloch simulation, significantly more artifacts appear across the resulting image from the AFP's imperfect inversion due to the spatially-varying $B_1^+$. As seen in the simulations, one possible solution to minimize any potential artifacts is to increase the adiabaticity of the pulses used. The two simplest approaches are either to increase the duration of the pulses while fixing the $BW$, or increase the peak power to ensure the pulse has sufficient power to be adiabatic across the region of interest. Another benefit of the ME-FREE sequence leverages the AFP's inherent ability to invert a wide bandwidth of isochromats in the presence of some constant offset, like a chemical-shift or resonance-offset. By utilizing a train of AFPs in a spin-echo like configuration, spins having off-resonance frequencies contained in the bandwidth of the adiabatic pulse experience an inversion and thus their different evolution phases are refocused. However, as with the original multi-shot FREE, the resulting acquired image is shifted along the FREE-encoded dimension. To further improve the ME-FREE resilience to offsets, the $BW$ of the pulses used should be increased to expand the adiabatic region where a good inversion occurs.

The original multi-shot FREE implementation utilized the longer pulse approach; where the pulses behaved more adiabatically at lower peak $B_1^+$, but at the cost of significantly greater average power delivered during the imaging sequence. In contrast, the multi-echo implementation presented here utilized shorter pulses and had a larger peak power, thus achieving comparable results but with only a fraction of the average power delivered. For example, the original multi-shot FREE had an average power delivered of 3.6 W to collect a 64 x 128 image matrix (= FREE $\times$ Readout) with a $TR = 3$ s, whereas the average power delivered by the new multi-echo FREE was 2.9 W for a 125 x 128 matrix with $TR = 2.5$ s. This value for the ME-FREE sequence corresponds to a local 10-g SAR of 5.0 W/kg at the hottest spot closest to the coil. Even considering the smallest $TR$ sequence, a safety factor of 2 was maintained as compared to the limits set forth for normal operating conditions of a local transmit coil used on a human head. This safety factor can be further increased by pairing the multi-echo technique with a lower field strength magnet ($< 1.5$ T).

In addition to significant reduction in average power delivered and thus SAR, the multi-echo technique was also able to collect an image in significantly less time. As compared to the original FREE implementation, the multi-echo sequence achieved comparable spatial resolution with an acceleration factor of 3.9. This acceleration factor represents a good foundation, especially compared to the previous sequence; however further acceleration can be achieved by incorporating more advanced imaging techniques, like parallel receive and partial Fourier.

With the benefits of a reduction in total scan time and in average power delivered, a more thorough analysis was performed to explore the types of contrast possible within this sequence. As the sequence was implemented, $TE$ was relatively long with the center of k-space being acquired during the second shot of each FM and FM*. However, it was still possible to acquire a variety of contrasts. For example, by increasing $TR$ at a fixed $TE$, the contrast gradually shifted to a more T2-weighted image with the ventricles transitioning from dark to bright, as expected. To further study the clinically relevant contrast, an inversion pulse was added before the initial excitation to create a FLAIR sequence. In this configuration, a FLAIR image only required 6 minutes to collect a 125 by 128 image, therefore making the sequence clinically viable, particularly in future implementations deploying parallel imaging.

To better understand the distortions that occur along the y- (coil-axis) direction, an analysis of the resolution was performed on a ME-FREE image using the previously presented framework, Eqn. 4.6. Using a simulated CST coil and the qualitative $B_1^+$ map, the spatially-varying pixel resolution was calculated for the resulting image. Three specific regions were considered for further analysis, specifically along the center of the coil and through the prominent horns that appear in the images. These regions illustrate a feature of FREE-based techniques; namely, that the spatial resolution is directly related to the gradient of the $B_1^+$ transmit field. The horns correspond to regions close to the surface coil loop where a large gradient is present in the transmit field, resulting in micron level spatial resolution. Because the transmit field amplitude decreases approximately with the inverse of the axial distance squared, the spatial resolution quickly decreases into regions where the pulses, both the excitation and AFPs, no longer behave appropriately.

This unique behavior illustrates an advantage of combining FREE-based techniques with a nonlinear $B_1^+$ field to perform spatial encoding. By having a spatially-variable resolution and $\Delta k$ vary across the ROI, it is possible to selectively sample regions with steep $B_1^+$ field at extremely high resolutions without needing to acquire the entire image at such fine resolution. The benefit of this variable sampling is evident in the acquired in-vivo images, where the total FOV along the ME-FREE dimension was set to 7 cm while maintaining regions of extremely high spatial resolution without any wrapping. To take advantage of this native high resolution, the reconstruction technique used to correct the acquired ME-FREE images utilized a zero-padding type approach before performing distortion and sensitivity correction[38]. The resulting image benefits from the high spatial resolution along the vertical dimension in regions of steep $B_1^+$, while further from the coil the voxels become larger, and the object becomes heavily blurred.

This spatially-varying resolution could be exploited using alternative coil geometries to produce more favorable transmit fields. All the experiments performed in this work utilized a single surface coil to produce the spatially-varying $B_1^+$ field. By exploring alternative coil geometries and techniques, it may be possible to produce a steep roughly linear $B_1^+$ amplitude across different regions in the ROI, thus further minimizing artifacts and potentially enabling selective zoom imaging with very high

spatial resolution. Alternatively, pTx type implementations could allow for the use of shallower $B_1^+$ gradients that cover the entire ROI, thus allowing for a reduction in the SAR.

Several different groups have proposed similar techniques exploiting unique coil geometries to create more favorable fields for encoding spatial information without $B_0$ gradients[128], [129]. For example, TRASE employs specific coil modes to produce a linear phase gradient with a uniform $B_1^+$ amplitude. With this configuration, TRASE plays out trains of block refocusing pulses alternating between the different coil modes to encode single points in k-space. However, ME- and MS-FREE sequences are not constrained by the need for such complex hardware and only require a coil to produce a spatially-varying $B_1^+$ field of sufficient power for the AFPs.

As presented in this work, the FREE-type sequence initially required the use of two additional pulsed $B_0$ gradients to perform slice selection and frequency encoding. However, a possible extension of this work would be to eliminate the additional pulsed $B_0$ gradients by employing the use of $B_1$ selective pulses[30]–[33]. Not only would this allow for the removal of an additional gradient but would expand the versatility of the sequence allowing for multi-slice acquisition schemes that are necessary to improve the sampling efficiency.

## 4.6  Conclusion

The multi-echo FREE technique presented in this work has demonstrated not only the capability of further eliminating pulsed $B_0$ gradients but also accelerated image acquisition of FREE-based sequences. These aspects present crucial advancements in not only the development of low-cost, portable MRI systems, but represent an important step towards improving the clinical feasibility of the systems and sequence.

## 4.7 Alternative: Iterative Model-Based Image Reconstruction of RF gradient-based MRI

The work presented in this section illustrates an alternative approach to preforming image correction for FREE based images. It has been presented as an abstract at ISMRM 2022 but remains an active area of research at the time of writing [130].

### 4.7.1 Introduction

Recent advancements in radiofrequency imaging (RFI) utilizing $B_1$ gradients to encode spatial information have shown the potential to produce images of equal or better quality than conventional MRI1. While there are distinct advantages to RFI based methods, advanced reconstructions techniques must be employed to correct the image distortions caused by nonlinear $B_1$ and $B_0$ inhomogeneities. To overcome these distortions, we propose a new reconstruction technique based on an iterative approach utilizing a full Bloch simulation and receiver coil sensitivities.

### 4.7.2 Methods

The recently developed RFI method called FREE (Frequency-modulated Rabi-Encoded Echoes) encodes spatial information in a manner resembling rotating frame zeugmatography [107], except the magnetization rotates about a time dependent $\mathbf{B}_{eff}(t)$ during an adiabatic sweep [21], [36], [85]. However, image distortions due to nonlinear $B_1$ and $B_0$ inhomogeneity were observed in FREE acquisitions that utilized Fourier-based image reconstruction techniques.

To overcome limitations in reconstruction, we propose utilizing an iterative first-order proximal gradient method to solve the regularized linear inverse problem of the form $||\mathbf{A}x - \mathbf{y}||_2^2 + \lambda\Omega(x)$ where $\mathbf{A}$ represents the encoding matrix determined via full Bloch simulation with known field inhomogeneities and the receive coil sensitivities [131], [132].

Initial in-vivo experiments were previously performed on a 1.5 T, 90-cm Oxford magnet with a Siemens gradient system utilizing a multi- shot FREE double spin-

echo sequence [113]. Two additional phantom simulations were performed with parameters comparable to previously acquired in-vivo data. These simulations focused on acceleration by under-sampling and the effect of performing FREE in a highly inhomogeneous $B_0$ field with a constant linear gradient. The first simulation considered FREE along two spatial dimensions with an acceleration factor of 4 and acquired on 8 separate receive channels. The latter considered the effect of a highly inhomogeneous static $B_0$ field and a permanent linear $B_0$ gradient producing 0.3 G/cm across a 5cm FOV [4].

### 4.7.3 Results

A comparison between FFT-based and the proposed model-based reconstructions is shown in Fig. 4.11. FREE spatial encoding was performed with the surface coil's (nonlinear) $B_1$ gradient in the vertical (y-axis) direction, while conventional $B_0$ frequency encoding was used in the horizontal (x-axis) direction. Images depict the occipital lobes of a healthy subject. By including the $B_1$ and $B_0$ inhomogeneity in the forward model much of the image distortion can be corrected using the proposed reconstruction approach.
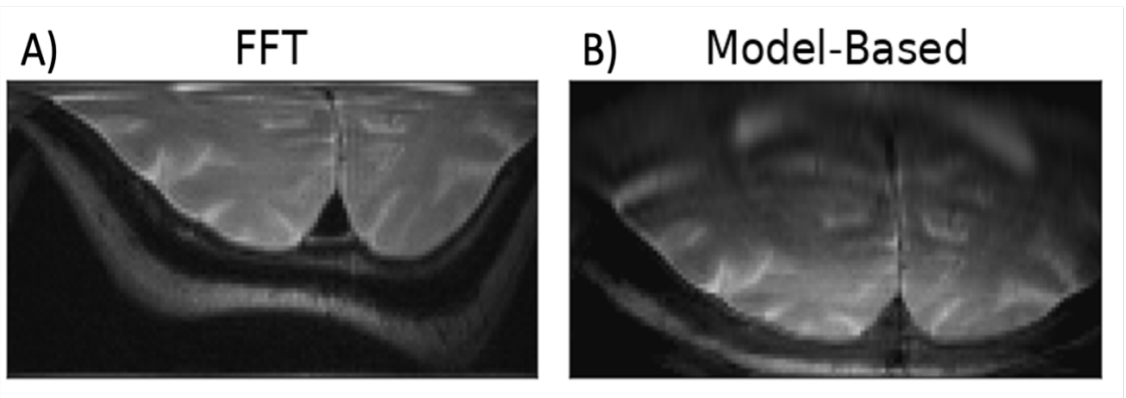


**Fig. 4.11.** A comparison of reconstruction methods. These images were acquired from a single surface coil placed 2.5 cm below the imaged object, using 1D FREE (y-axis) combined with 1D frequency-encoding (x-axis). The in-vivo image acquired using the double spin-echo FREE acquisition. Model-based reconstruction removes much of the distortion caused by the highly nonlinear $B_1$ gradient of the surface transmitter coil. The coil was positioned 2.5 cm posteriorly to the object.

Fig. 4.12 shows a reconstruction created from a Bloch simulation of a 2-dimensional double spin-echo FREE experiment, using identical surface coils along both dimensions. The data was acquired on 8 separate receive coils with an acceleration factor of 4 and random complex gaussian noise added. By incorporating the $B_1$ maps and receive coil sensitivity profiles into the forward model the distortions can be removed, and an alias free image can be recovered.
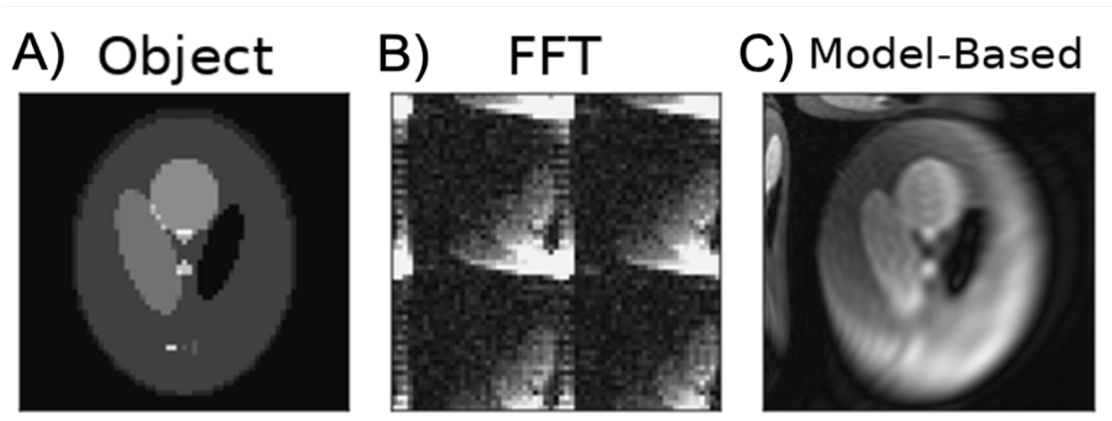


**Fig. 4.12.** Simulation of an accelerated 2D double spin-echo FREE sequence using two surface coils and 8 receive coils. The acquisition had an acceleration factor of 4 and the transmit coils were placed on the left-hand side and top of the object, respectively. Complex random gaussian noise was added to the simulated k-space data collected by each receive coil. Panel A) shows a ground truth image of the Shepp-Logan phantom that used in simulations. Panel B) show a standard FFT reconstruction. Panel C) shows the iterative model-based technique. Distortion correction was performed in post-processing by including the nonlinear $B_1$ and $B_0$ profiles into the forward model.

Finally, an extreme example (Fig. 4.13) shows the reconstruction from a Bloch simulation of the double spin-echo FREE experiment, using a surface coil for FREE (x-axis) and the calculated permanent $B_0$ gradient (y-axis) generated from a simulated passive shim set in a compact 1.5T head magnet. This result demonstrates that FREE, when combined with a permanent $B_0$ gradient for frequency encoding, can generate good images with $B_1$ and $B_0$ maps included in the forward model.
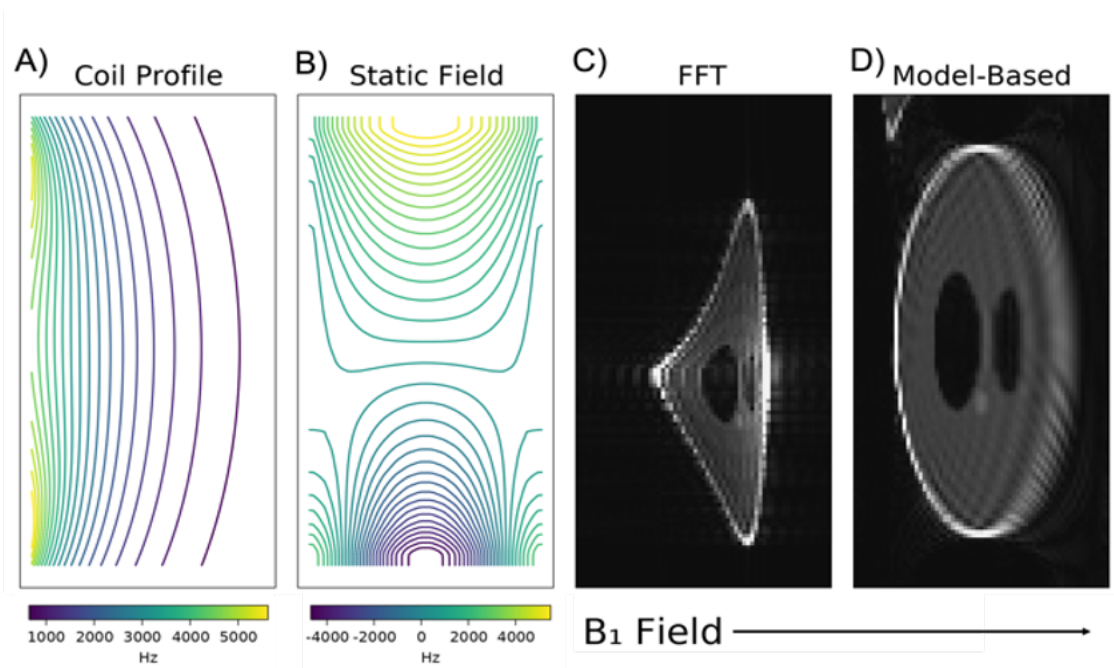
**Fig. 4.13.** Simulation of the double spin-echo FREE sequence using a surface coil and the permanent $B_0$ gradient of the passive gradient shim of the head-only magnet. Panel A) shows the nonlinear $B_1$ gradient produced by the surface coil placed on the left side, producing a $B_1$ gradient mainly in the horizontal (x) direction. Panel B) shows the static $B_0$ inhomogeneity of the permanent $B_0$ gradient, which is mainly in the vertical (y) direction. The right two panels show a standard FFT reconstruction and an iterative model-based technique, respectively. Distortion correction was performed in post-processing by including the nonlinear $B_1$ and $B_0$ profiles into the forward model.

## 4.7.4 Discussion

A primary limitation to model-based reconstruction is the need to accurately characterize the imaging system and address any mismatches between the encoding matrix and the physical experiment that can lead to artifacts in the reconstructed image. The latter can be challenging for some MRI methods that use traditional $B_0$ gradients for spatial encoding, since imperfections in $B_0$ gradients (eg, eddy currents) can be more difficult to model, whereas RF modulations typically have high fidelity. As such, RFI-based sequences that employ a $B_1$ gradient to perform spatial

encoding are highly reproducible. Moreover, the results herein show that at 1.5T a simple static Biot-Savart simulation is enough to adequately model the transmit coil profile. Incorporating this transmit profile into the encoding matrix led to significant improvement in the reconstructed image quality, especially compared to the traditional Fourier-based reconstruction. However at large distances from transmit coil, the object becomes heavily blurred as the strength of the $B_1$ gradient decreases.

When applied to accelerated FREE-based acquisitions with noise added, the proposed method reconstructs the highly distorted, aliased image while eliminating most of the artifacts. Despite these artifacts, the reconstructed image is significantly better than that of FFT-based methods. The reconstruction method was then applied to a simulation of an object in the presence of a highly inhomogeneous static $B_0$ field and a nonlinear surface coil. The resulting Fourier reconstructed image is highly distorted along both dimensions due to the presence of the nonlinear fields. However, by incorporating these fields into the encoding matrix, the proposed reconstruction method was still able to produce images that are relatively distortion-free.

### 4.7.5   Conclusion

Standard Fourier based reconstruction has often produced artifacts when used in conjunction with RFI based methods, limiting their adoption in clinical settings. However, the proposed reconstruction method presented here has shown that the artifacts can be eliminated and even accelerates acquisition. With these new tools, RFI based imaging methods become more clinically viable and should ultimately produce comparable images to conventional acquisitions.

# Chapter 5

# Technological Development of a Portable MRI

## 5.1 Introduction

The initial goal of this project was to build the first-ever 1.5 T portable human MRI scanner, requiring only the subject's head to be inside the magnet bore. This configuration is distinct and allows for the subject's shoulders to remain outside; thus, opening the door to innovative motor coordination studies. Furthermore, the system was designed with a built-in window for the subject to see out of. From a patient standpoint this would not only allow for the easement of claustrophobia related stress, but also allow for interactions with the outside world. From a technical standpoint these design requirements, coupled with making a transportable imaging system, presented unique challenges to not only produce the magnet but also the imaging system built around it. To accomplish these goals the new system utilizes completely custom hardware to allow for both portability and the acquisition of high-fidelity images for clinical use.

As this project was an international collaboration by several research organizations, a brief overview of several key areas will be presented and references will be provided expanding upon the hardware and techniques. The focus of this section is the system integration, the incremental testing of each subsystem, and the final sys-

tem testing. All of this leads up to capturing a 3D image within the system. As time of writing human approval has not been approved, but a brief discussion outlines the steps necessary and the future goals for the system.

## 5.2 Validation of Subsystems at UMN

As this project is a collaboration between several different international research institutions, it was essential to test each of the sub-assemblies before final assembly. Two of the most critical components of the imaging system were the digital magnetic resonance spectrometer (DMRS) and the Multi-Coil array (MC-array); together they form the necessary backbone for standard imaging operations on the portable MRI scanner [121], [133]. The DMRS is, in a sense, the 'brain' of the imaging system and has been previously tested in different applications [38], [104], [113]. These experiments acted as a good stress test for not only the hardware but also the software necessary to program the spectrometer. For these previous experiments a commercial Siemens gradient system was utilized to isolate the DMRS in a known environment for testing.

With the DMRS known to be functional, the next step was to integrate the MC-array gradient system into the existing hardware and software. This was accomplished by building a custom mounting structure that allowed for the MC-array to be placed into the isocenter of an un-shielded, un-shimmed Oxford 4 T magnet and ramped down to 1.5 T to mimic the field strength of the portable magnet, Fig. 5.1. With the MC-array in place, all of the necessary electrical and plumbing was then run. Modifications to the existing 3D sequences were made to properly trigger the Resonance Research Inc amplifier, creating the desired fields using 31 independent gradient coils [133].

**Fig. 5.1.** MC-Array Mounted inside an Oxford 1.5 T whole body Magnet. A custom holder was designed and built to secure the MC-array at the isocenter of the magnet. All of the necessary plumbing and electrical connections were installed in place to better replicate the final installation within the portable magnet.

The initial sequence chosen for testing was a 3D GRE, utilizing a proven 10-cm surface coil. As the MC-array utilizes 31 independently driven gradient coils to synthesize linear gradient fields, errors in the gradient tables can be difficult and non-intuitive to diagnosis [133]. The chosen initial sequence minimized potential complications with an implementation that was straightforward and easy to troubleshoot. A large cylindrical phantom was chosen as it provided sufficient loading for the RF coil while also spanning the entire FOV of the MC-array. The first acquired images utilizing the DMRS and the MC-array in conjunction are presented in Fig. 5.2. These results were promising in that the subsystems were able to work in conjunction with each other and produce an image utilizing the synthesized linear gradient fields; however, the performance of the system will need to be re-evaluated once the portable
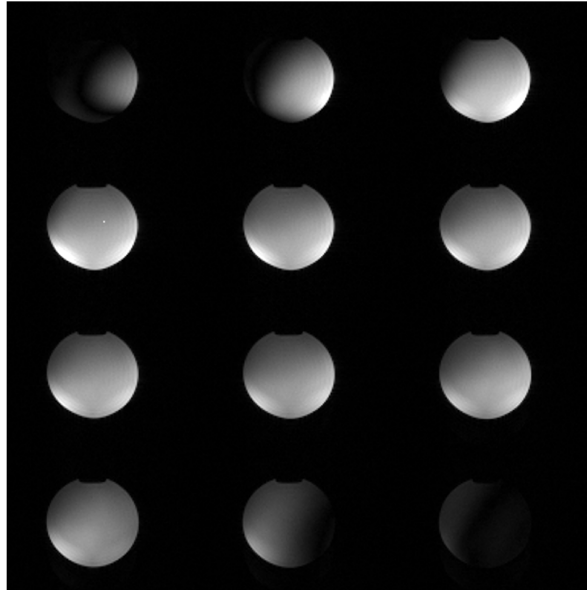
magnet has been delivered and installed.



**Fig. 5.2.** First MC-Array image acquired at the Center for Magnetic Resonance Research. 10-cm curved surface coil tuned for 1.5 T was place along the bottom of the MC-Array with a phantom inserted on top. A 3D GRE sequence was programmed on the DMRS to provide the necessary triggering signals required for the MC-Array amplifiers. The gradient tables were calculated to give a resolution of 2 x 2 x 2 mm and a corresponding FOV of 192 x 256 x128 mm.

## 5.3    Overview of the Magnet and Subsystems

The magnet designed for the project was based around the Yttrium barium copper oxide (YBCO) high temperature superconductor (HTS) material. This material is unique in that it does not require liquid helium to reach its critical temperature; which is much higher than conventional low temperature superconductors (LTS) materials. In fact, similar LTS materials like Niobium–Titanium (NbTi) have a critical temperature around 4.2 K at 1.5 T, significantly lower than YBCO at roughly 35 K [134]–[136]. This affords several key advantages compared to traditional LTS magnets. For example, an HTS magnet is the most compact superconducting magnet

implementation of a design, since high temperature operation permits the removal of bulky isothermal radiation shielding and large liquid cryogen baths that are typically required for LTS magnets. In addition, high-temperature operation only requires the use of a highly efficient single stage cryocooler; allowing for cool-down times as short as 1 - 2 days and tolerating 10's of watts of heat loaded into the magnet cryostat during steady-state operation. Lastly, HTS magnets seldom quench during normal operation, even when ramping to field following a thermal cycle or when interacting with gradient coil fields.



**Fig. 5.3.** Portable HTS magnet system installed at the Center for Magnetic Resonance Research. It was placed in front of a ramped down 4 T whole body scanner that utilized a low temperature superconductor and liquid helium to generate the main polarizing field. The silver hemisphere contains the HTS coils and generates the main polarizing field that a patient is raised into. The photo illustrates the stark contrast of the total size of the new portable scanner compared to the previous conventional system.

The portable scanner was delivered and installed at the University of Minnesota following extensive testing at Victoria University in Wellington, New Zealand. An

example of the necessary tests that were performed prior to shipping and delivery included the evaluation of the main polarizing field, initial placement of the passive shims, and validation of the various patient safety systems. Upon delivery the HTS magnet was incorporated into the existing hardware and software infrastructure to ensure that the magnet could be properly controlled and monitored, Fig. 5.3. As the HTS magnet is not a persistent magnet requiring a constant supply of current, proper monitoring of the temperature, pressure, and current is crucial to ensuring stability.

## 5.4 Mapping the homogeneity of the Main Field

To evaluate the uniformity of the main polarizing field at Center for Magnetic Resonance Research (CMRR), a Hall probe was mounted to a 3-axis translation stage and used to map the field. The region of interest was selected at the surface of an Adult male's brain to ensure maximum heterogeneity for neuro-imaging type applications. With the initial map collected, a loading scheme for the passive shim cassette was calculated and then installed. This process was repeated an additional two times to ensure that the loading was performed correctly and the final heterogeneity was acceptable, Fig. 5.4.
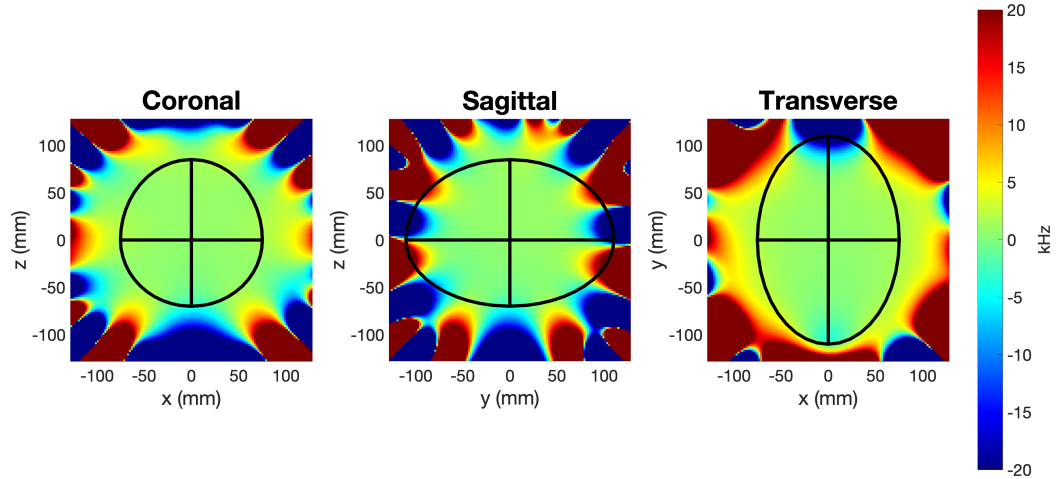
**Fig. 5.4.** Final measured $B_0$ inhomogeneity. After installation was finalized, the uniformity was measured using a 3D translation stage and a Hall probe. The region of interest, illustrated by the ellipsoid, corresponds a normal male subject's brain. Overall the inhomogenity within a 20 cm diameter spherical volume varies by 16 kHz, however, when considering a 10 cm diameter spherical volume this drops significantly to a variation of 1 kHz

The resulting field plots show a significant amount of field variation across the entire imaging volume, especially towards the end of the defined region of interest. For example, considering a diameter spherical volume (DSV) of 20 cm located at the center of the field plots, the field variation is 20khz. However, this is relative to the physical center of the magnet and not the center of the Additionally, several approaches have been presented that can perform well in highly inhomogeneous $B_0$ field [90], [137]. With the resulting field plots it is then possible to incorporate them into a model-based reconstruction type approach to perform any necessary distortion corrections.

## 5.5 First images acquired in complete system

With the final uniformity of the magnet known, the next step was to produce an image using all of the magnet subsystems in place and operating together. Up until this point, all of the subsystems have been thoroughly tested; however, this was the first time the portable HTS magnet was incorporated into the tests. At the time, it wasn't known how the MC-Array would interact with the internals of the magnet and whether it was even possible to acquire an image.

The initial imaging experiments utilized a flat 10-cm surface coil mounted onto a sheet of acrylic. This was then placed near the center of the magnet in a fairly homogeneous region of the $B_0$ field away from the MC-array to minimize the effects of any possible eddy currents. To provide a unique structure to image a lemon was chosen as the initial phantom, Fig. 5.5. This would not only present unique structures but also push the resolution of the MC-array. To account for this, the synthesized linear gradient needed to be regenerated to produce a fine enough resolution to resolve the internal features of the lemon. A 3D GRE sequence was developed and programmed to acquire an image with TE = 8 ms, TR = 55 ms, FOV of 90 x 67 x 96 mm, and a resolution of 0.7 x 0.7 x 2 mm.
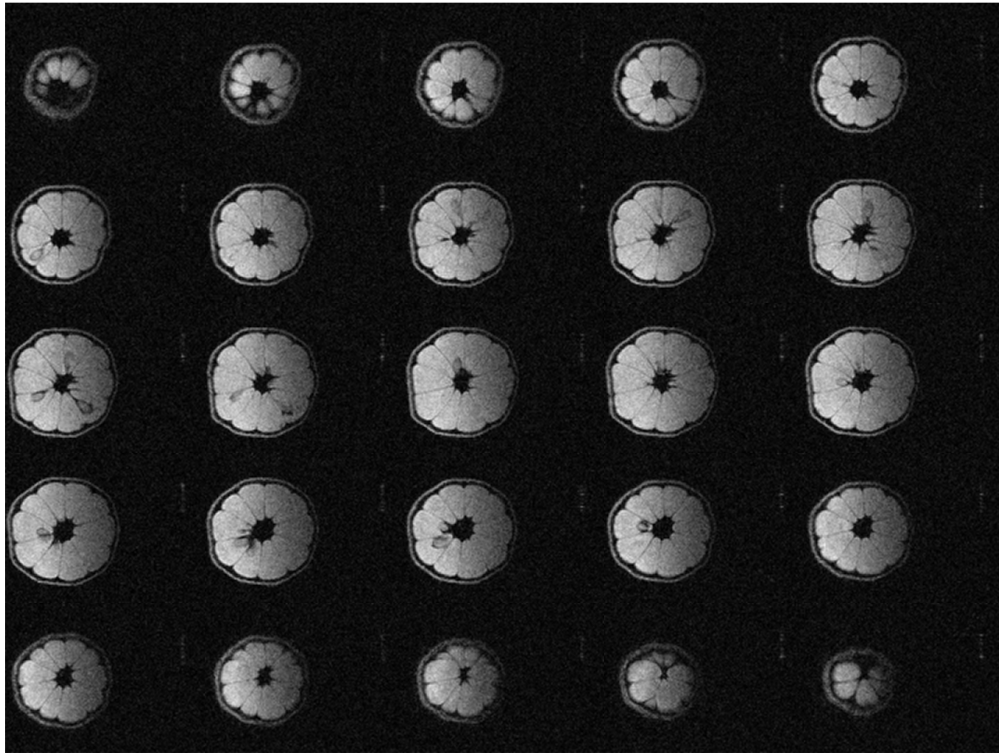
**Fig. 5.5.** First 3D image Acquired in the HTS Portable Scanner. A 3D GRE image of a lemon was acquired using a 10-cm surface coil placed inside the portable scanner. The MC-array gradients tables were modified to produce A 3D GRE sequence was developed and programmed to acquire an image with a TE = 8 ms, TR = 55 ms, FOV of 90 x 67 x 96 mm, and a resolution of 0.7 x 0.7 x 2 mm. Four averages were acquired to improve the SNR.

## 5.6 Path Moving Forward

Despite the completion of the initial system integration and the acquisition of some 3D data sets, more work and further system validation must still be performed. However, the results presented here represents an important milestone in the project as all of the necessary hardware and software have been assembled and tested as a complete imaging system. The next steps moving forward will focus on better characterizing the system and optimizing the acquisition methods to improve upon the

acquired images. This work will include measuring and correcting for any potential eddy currents, better mapping the main polarizing field, and expanding upon the image reconstruction techniques to better deal with any inhomogeneities that can be measured in the system.

# Chapter 6

# Future of Nonlinear Techniques and Portable MRI

The projects presented throughout this work occurred during a unique period in MRI, where an apparent schism is forming between the drive for higher field strengths and better resolution and the development of lower cost and portable imaging systems. At first glance, these two groups seem to be pursing very different goals; however, that could not be further from the truth. Both groups are looking for unique solutions via new methodology and hardware to develop a better imaging chain that is capable of pushing higher resolution and better patient care. Often the technology and methodology that is developed for either group can be readily applied to the other allowing for a mutual benefit.

This work has mainly been focused on developing techniques and hardware solutions for lower field applications but the underlying physics remain the same. In fact, there are potential improvements that could be made when applying these techniques at higher fields with more advanced commercial hardware, where the system has been extensively modeled and characterized. For example, not only could the resolution gains from nonlinear encoding approaches could be utilized in a clinical system, but the characterization of such a system would only improve the reconstruction methods presented herein. The implementation of such sequences would require only minor changes to the clinical setup as the methodologies are magnet invariant.

Conversely, with the advancements made throughout the imaging chain revisit-

ing lower field MRI can potentially reap the benefits in SNR. Fundamentally, more signal will always be present at higher-field strengths but by employing clever reconstruction techniques and imaging methods these limitations could be overcome. For instance, by employing physics informed neural networks it may be possible to combine the advantages of an iterative model-based reconstruction approach with a trained neural network; thus, potentially improving upon the SNR while leveraging the resolution benefits of nonlinear techniques. As clinical systems extensively model the imaging chain, it may be possible to get so called "real time" reconstruction of distortion-corrected images.

Beyond the implementation on clinical systems, the hardware developed specifically for the portable scanner represents an untapped area of exploration. The capability of 31 independent gradient coils to synthesize arbitrary gradient wave-forms in both space and time provides a unique opportunity to explore encoding sequences that have not been possible to implement previously. This could lead to new spatiotemporal encoding schemes where a hyperboloidal could be traversed along a spiral trajectory, encoding regions of very high spatial resolution. Due to the unique and flexible nature of the MC-array, significantly more simulations will need to be performed to better understand all of the possible gradients that can be synthesized using the 31 coils with the goal of creating waveform in real time. Significantly more computational work will need to be preformed to reach this goal but it would open the door to incorporating these models into the previously discussed reconstruction framework.

All of the technology and techniques presented in this work showcase a small percentage of the work being performed within the field of MRI. However, by utilizing knowledge gained from other areas we are scratching the surface at what is possible. This is only the beginning of exploration on this system but the future looks bright and promising.

# References

[1] A. E. Campbell-Washburn, R. Ramasawmy, M. C. Restivo, *et al.*, "Opportunities in interventional and diagnostic imaging by using high-performance low-field-strength mri," *Radiology*, vol. 293, no. 2, pp. 384–393, 2019.

[2] S. Geethanath and J. T. Vaughan Jr., "Accessible magnetic resonance imaging: A review," *Journal of Magnetic Resonance Imaging*, vol. 49, no. 7, e65–e77, 2019.

[3] A. Macovski and S. Conolly, "Novel approaches to low-cost mri," *Magnetic Resonance in Medicine*, vol. 30, no. 2, pp. 221–30, 1993.

[4] L. L. Wald, P. C. McDaniel, T. Witzel, J. P. Stockmann, and C. Z. Cooley, "Low-cost and portable mri," *Journal of Magnetic Resonance Imaging*, vol. 52, no. 3, pp. 686–696, 2020.

[5] E. Haacke, R. Brown, M. Thompson, and R. Venkatesan, *Magnetic Resonance Imaging: Physical Principles and Sequence Design.* John Wiley & Sons, Inc., 1999, ISBN: 9780471351283.

[6] A. Abragam, *Principles of Nuclear Magnetism.* Oxford University Press, 1967.

[7] B. Cowan, *Nuclear Magnetic Resonance and Relaxation.* Cambridge University Press, 1997.

[8] R. Shankar, *Principles of Quantum Mechanics.* Plenum Press, 1994, ISBN: 9780306447907.

[9] D. Hoult and B. Bhakar, "Nmr signal reception: Virtual photons and coherent spontaneous emission," *Concepts in Magnetic Resonance*, vol. 9, no. 5, pp. 277–297, 1997.

[10] I. Rabi, J. Zacharias, S. Millman, and P. Kusch, "A new method of measuring nuclear magnetic moment," *Physical Review*, vol. 53, pp. 318–318, 1938.

[11] F. Bloch, W. Hansen, and M. Packard, "Nuclear induction," *Physical Review*, vol. 69, pp. 127–127, 1946.

[12] F. Bloch, "Nuclear induction," *Physical Review*, vol. 70, pp. 460–474, 1946.

[13] F. Bloch, W. Hansen, and M. Packard, "The nuclear induction experiment," *Physical Review*, vol. 70, pp. 474–485, 1946.

[14] E. Purcell, H. Torrey, and R. Pound, "Resonance absorption by nuclear magnetic moments in a solid," *Physical Review*, vol. 69, pp. 37–38, 1946.

[15] R. Ernst and W. Anderson, "Application of fourier transform spectroscopy to magnetic resonance," *Review of Scientific Instruments*, vol. 37, no. 1, pp. 93–102, 1966.

[16] P. Lauterbur, "Image formation by induced local interactions: Examples employing nuclear magnetic resonance," *Nature*, vol. 242, pp. 190–192, 1973.

[17] P. Lauterbur and P. Grannell, "Nmr 'diffraction' in solids?" *Journal of Physics C: Solid State Physics*, vol. 6, pp. L422–L426, 1973.

[18] D. Hoult, "Zeugmatography: A criticism of the concept of a selective pulse in the presence of a field gradient," *Journal of Magnetic Resonance*, vol. 26, pp. 165–167, 1977.

[19] D. J. Griffiths, *Classical Electrodynamics*. Prentice Hall, 1999, ISBN: 9781108420419.

[20] J. Taylor, *Classical Mechanics*. University Science Books, 2005, ISBN: 9781891389221.

[21] M. Garwood and L. DelaBarre, "The return of the frequency sweep: Designing adiabatic pulses for contemporary nmr," *Journal of Magnetic Resonance*, vol. 153, pp. 155–177, 2001.

[22] M. Silver, R. Joseph, and D. Hoult, "Highly selective $\pi/2$ and $\pi$ pulse generation," *Journal of Magnetic Resonance*, vol. 59, pp. 347–351, 1984.

[23] A. Tannús and M. Garwood, "Adiabatic pulses," *NMR in Biomedicine*, vol. 10, no. 8, pp. 423–434, 1997.

[24] J. Pauly, D. Nishimura, and A. Macovski, "A k-space analysis of small-tip-angle excitation," *Journal of Magnetic Resonance*, vol. 81, pp. 43–56, 1989.

[25] M. Griswold, P. Jakob, R. Heidemann, *et al.*, "Generalized autocalibrating partially parallel acquisitions (grappa)," *Magnetic Resonance in Medicine*, vol. 47, pp. 1202–1210, 2002.

[26] K. Pruessman, M. Weiger, M. Scheidegger, and P. Boesiger, "Sense: Sensitivity encoding for fast mri," *Magnetic Resonance in Medicine*, vol. 42, pp. 952–962, 1999.

[27] W. Press, S. Teukolsky, W. Vetteringly, and B. Flannery, *Numerical Recipes: The Art of Scientific Computing*. Cambridge University Press, 2007, ISBN: 9780521880688.

[28] J. C. Sharp and S. B. King, "Mri using radiofrequency magnetic field phase gradients," *Magnetic Resonance in Medicine*, vol. 63, no. 1, pp. 151–161, 2010.

[29] R. Kartausch, T. Driessle, T. Kampf, *et al.*, "Spatial phase encoding exploiting the bloch-siegert shift effect," *MAGMA*, vol. 27, no. 5, pp. 363–71, 2014.

[30] L. K. Hedges and D. I. Hoult, "The techniques of rotating frame selective excitation and some experimental results," *Journal of Magnetic Resonance*, vol. 79, no. 3, pp. 391–403, 1988.

[31] D. I. Hoult, "Nmr imaging - rotating frame selective pulses," *Journal of Magnetic Resonance*, vol. 38, no. 2, pp. 369–374, 1980.

[32] J. Kaczyński, N. J. F. Dodd, and B. Wood, "Selective excitation in the rotating frame with hard pulses," *Journal of Magnetic Resonance*, vol. 100, no. 3, pp. 453–468, 1992.

[33] J. B. Martin, S. A. Srinivas, C. E. Vaughn, H. Sun, M. A. Griswold, and W. A. Grissom, "Selective excitation localized by the bloch-siegert shift and a $B_1^+$ gradient," *Magnetic Resonance in Medicine*, vol. 88, no. 3, pp. 1081–1097, 2022.

[34] Y. Lee, Y. Han, H. Park, H. Watanabe, M. Garwood, and J.-Y. Park, "New phase-based $B_1$ mapping method using two-dimensional spin-echo imaging with hyperbolic secant pulses," *Magnetic Resonance in Medicine*, vol. 73, no. 1, pp. 170–181, 2015.

[35] M. Garwood and L. DelaBarre, "The return of the frequency sweep: Designing adiabatic pulses for contemporary nmr," *Journal of Magnetic Resonance*, vol. 153, pp. 155–177, 2001.

[36] T. Froelich, M. Mullen, and M. Garwood, "Mri exploiting frequency-modulated pulses and their nonlinear phase," *Journal of Magnetic Resonance*, vol. 318, p. 106 779, 2020.

[37] J. Park and M. Garwood, "Spin-echo mri using $\pi/2$ and $\pi$ hyperbolic secant pulses," *Magnetic Resonance in Medicine*, vol. 61, pp. 175–187, 2009.

[38] P. Wang, T. Froelich, E. Torres, *et al.*, "Correcting image distortions from a nonlinear $B_1^+$-gradient field in frequency-modulated rabi-encoded echoes," *Magnetic Resonance in Medicine*, vol. 89, no. 5, pp. 2100–2108, 2023.

[39] M. Bendall and D. Pegg, "Uniform sample excitation with surface coils for in vivo spectroscopy by adiabatic rapid half passage.," *Journal of Magnetic Resonance*, vol. 67, pp. 376–381, 1986.

[40] M. Garwood, K. Ugurbil, A. R. Rath, *et al.*, "Magnetic resonance imaging with adiabatic pulses using a single surface coil for rf transmission and signal detection," *Magnetic Resonance in Medicine*, vol. 9, no. 1, pp. 25–34, 1989.

[41] C. Hardy, W. Edelstein, and D. Vatis, "Efficient adiabatic fast passage for nmr population inversion in the presence of radiofrequency field inhomogeneity and frequency offsets.," *Journal of Magnetic Resonance*, vol. 66, pp. 470–482, 1986.

[42] A. Johnson, M. Garwood, and K. Ugurbil, "Slice selection with gradient-modulated adiabatic excitation despite the presence of large $B_1$ inhomogeneities," *Journal of Magnetic Resonance*, vol. 81, pp. 653–660, 1989.

[43] J.-J. Dun and J. Delayre, "Impulse response magnetic resonance spectrometer - patent," no. US3975675A, 1976.

[44] J. Klauder, A. Price, S. Darlington, and W. Albersheim, "The theory and design of chirp radars," *Bell Syst. Tech. J.*, vol. 39, no. 4, pp. 746–808, 1960.

[45] S. L. McCall and E. L. Hahn, "Self-induced transparency by pulsed coherent light," *Physical Review Letters*, vol. 18, no. 21, pp. 908–911, 1967.

[46] S. L. McCall and E. L. Hahn, "Self-induced transparency," *Physical Review*, vol. 183, no. 2, pp. 457–485, 1969.

[47] M. S. Silver, R. I. Joseph, C. N. Chen, V. J. Sank, and D. I. Hoult, "Selective population inversion in nmr," *Nature*, vol. 310, no. 5979, pp. 681–683, 1984.

[48] M. Garwood and L. DelaBarre, "The return of the frequency sweep: Designing adiabatic pulses for contemporary nmr," *Journal of Magnetic Resonance*, vol. 153, no. 2, pp. 155–177, 2001.

[49] C. P. Slichter, *Principles of magnetic resonance*, 3rd, ser. Springer Series in Solid-State Sciences. New York: Springer-Verlag, 1990.

[50] Z. H. Cho and Y. M. Ro, "Reduction of susceptibility artifact in gradient-echo imaging," *Magnetic Resonance in Medicine*, vol. 23, no. 1, pp. 193–200, 1992.

[51] J.-Y. Chung, H. W. Yoon, Y.-B. Kim, H. W. Park, and Z.-H. Cho, "Susceptibility compensated fmri study using a tailored rf echo planar imaging sequence," *Journal of Magnetic Resonance Imaging*, vol. 29, no. 1, pp. 221–228, 2009.

[52] Y. M. Ro and Z. H. Cho, "A new frontier of blood imaging using susceptibility effect and tailored rf pulses," *Magnetic Resonance in Medicine*, vol. 28, no. 2, pp. 237–248, 1992.

[53] S. J. Wastling and G. J. Barker, "Designing hyperbolic secant excitation pulses to reduce signal dropout in gradient-echo echo-planar imaging," *Magnetic Resonance in Medicine*, vol. 74, no. 3, pp. 661–672, 2015.

[54] A. A. Maudsley, "Dynamic range improvement in nmr imaging using phase scrambling," *Journal of Magnetic Resonance (1969)*, vol. 76, no. 2, pp. 287–305, 1988.

[55] J.-Y. Park, L. DelaBarre, and M. Garwood, "Improved gradient-echo 3d mri using pseudo-echoes created by frequency-swept pulses," *Magnetic Resonance in Medicine*, vol. 55, pp. 848–857, 2006.

[56] J.-N. Dumez and L. Frydman, "Multidimensional excitation pulses based on spatiotemporal encoding concepts," *Journal of Magnetic Resonance*, vol. 226, no. Supplement C, pp. 22–34, 2013.

[57] Y. Shrot and L. Frydman, "Spatially-encoded nmr and the acquisition of 2d magnetic resonance images within a single scan," *Journal of Magnetic Resonance*, vol. 171, pp. 179–190, 2005.

[58] R. Chamberlain, J. Y. Park, C. Corum, *et al.*, "Raser: A new ultrafast magnetic resonance imaging method," *Magnetic Resonance in Medicine*, vol. 58, no. 4, pp. 794–799, 2007.

[59] J.-K. Ryu, S. Han, S.-H. Oh, J. Lee, S.-G. Kim, and J.-Y. Park, "A new ultrafast 3d gradient echo-based imaging method using quadratic-phase encoding," *Magnetic Resonance in Medicine*, vol. 82, no. 1, pp. 237–250, 2019.

[60] A. L. Snyder, C. A. Corum, S. Moeller, N. J. Powell, and M. Garwood, "Mri by steering resonance through space," *Magnetic Resonance in Medicine*, vol. 72, no. 1, pp. 49–58, 2014.

[61] D. Kunz, "Use of frequency-modulated radiofrequency pulses in mr imaging experiments," *Magn. Reson. Med.*, vol. 3, p. 377, 1986.

[62] M. R. Bendall, M. Garwood, K. Ugurbil, and D. T. Pegg, "Adiabatic refocusing pulse which compensates for variable rf power and off-resonance effects," *Magnetic Resonance in Medicine*, vol. 4, no. 5, pp. 493–499, 1987.

[63] P. A. Bottomley and R. Ouwerkerk, "Birp, an improved implementation of low-angle adiabatic (bir-4) excitation pulses," *Journal of Magnetic Resonance, Series A*, vol. 103, no. 2, pp. 242–244, 1993.

[64] S. Conolly, D. Nishimura, and A. Macovski, "A selective adiabatic spin-echo pulse.," *Journal of Magnetic Resonance*, vol. 83, pp. 324–334, 1989.

[65] M. Garwood, B. Nease, Y. Ke, R. de Graaf, and H. Merkle, "Simultaneous compensation for $B_1$ inhomogeneity and resonance offsets by a multiple-quantum nmr sequence using adiabatic pulses.," *Journal of Magnetic Resonance, Series A*, vol. 112, pp. 272–274, 1995.

[66] M. Garwood and Y. Ke, "Symmetric pulses to induce arbitrary flip angles with compensation for rf inhomogeneity and resonance offsets," *Journal of Magnetic Resonance (1969)*, vol. 94, no. 3, pp. 511–525, 1991.

[67] T. L. Hwang, P. C. van Zijl, and M. Garwood, "Broadband adiabatic refocusing without phase distortion," *Journal of Magnetic Resonance*, vol. 124, no. 1, pp. 250–254, 1997.

[68] R. S. Staewen, A. J. Johnson, B. D. Ross, T. Parrish, H. Merkle, and M. Garwood, "3-d flash imaging using a single surface coil and a new adiabatic pulse, bir-4," *Investigative Radiology*, vol. 25, no. 5, pp. 559–567, 1990.

[69] K. Ugurbil, M. Garwood, and M. Bendall, "Amplitude and frequency modulated pulses to achieve 90° plane rotations with inhomogeneous $B_1$ fields.," *Journal of Magnetic Resonance*, vol. 72, pp. 177–185, 1987.

[70] P. Balchandani, G. Glover, J. Pauly, and D. Spielman, "Improved slice-selective adiabatic excitation," *Magnetic Resonance in Medicine*, vol. 71, pp. 75–82, 2014.

[71] P. Balchandani, J. Pauly, and D. Spielman, "Slice-selective tunable-flip adiabatic low peak-power excitation pulse," *Magnetic Resonance in Medicine*, vol. 59, no. 5 @ 0740-3194, pp. 1072–1078, 2008.

[72] R. A. de Graaf, K. Nicolay, and M. Garwood, "Single-shot, $B_1$-insensitive slice selection with a gradient-modulated adiabatic pulse, biss-8," *Magnetic Resonance in Medicine*, vol. 35, no. 5, pp. 652–657, 1996.

[73] J. Shen and D. L. Rothman, "Adiabatic slice-selective excitation for surface coils," *Journal of Magnetic Resonance*, vol. 124, no. 1, pp. 72–79, 1997.

[74] S. Conolly, G. Glover, D. Nishimura, and A. Macovski, "A reduced power selective adiabatic spin-echo pulse sequence," *Magnetic Resonance in Medicine*, vol. 18, no. 1, pp. 28–38, 1991.

[75] H. Dyvorne, R. O'Halloran, and P. Balchandani, "Ultrahigh field single-refocused diffusion weighted imaging using a matched-phase adiabatic spin echo (mase)," *Magnetic Resonance in Medicine*, vol. 75, no. 5, pp. 1949–1957, 2016.

[76] D. Kunz, "Use of frequency-modulated radiofrequency pulses in mr imaging experiments," *Magnetic Resonance in Medicine*, vol. 3, pp. 377–384, 1986.

[77] J. G. Pipe, "Spatial encoding and reconstruction in mri with quadratic phase profiles," *Magnetic Resonance in Medicine*, vol. 33, no. 1, pp. 24–33, 1995.

[78] J. G. Pipe, "Analysis of localized quadratic encoding and reconstruction," *Magnetic Resonance in Medicine*, vol. 36, no. 1, pp. 137–146, 1996.

[79] J. G. Pipe, "Flow effects in localized quadratic, partial fourier mra," *Magnetic Resonance in Medicine*, vol. 41, no. 2, pp. 309–314, 1999.

[80] J. Zhang, M. Garwood, and J. Y. Park, "Full analytical solution of the bloch equation when using a hyperbolic-secant driving function," *Magnetic Resonance in Medicine*, 2016.

[81] J. Zhang, M. Garwood, and J.-Y. Park, "Erratum to: Full analytical solution of the bloch equation when using a hyperbolic-secant driving function (magn reson med 2017;77:1630-1638)," *Magnetic Resonance in Medicine*, vol. 79, no. 6, pp. 3274–3274, 2018.

[82] D. Idiyatullin, C. Corum, S. Moeller, and M. Garwood, "Gapped pulses for frequency-swept mri," *Journal of Magnetic Resonance*, vol. 193, no. 2, pp. 267–273, 2008.

[83] D. Idiyatullin, C. Corum, J. Y. Park, and M. Garwood, "Fast and quiet mri using a swept radiofrequency," *Journal of Magnetic Resonance*, vol. 181, no. 2, pp. 342–349, 2006.

[84] J. Dadok and R. Sprecher, "Correlation nmr spectroscopy," *Journal of Magnetic Resonance*, vol. 13, pp. 243–248, 1974.

[85] A. Tannus and M. Garwood, "Adiabatic pulses," *NMR in Biomedicine*, vol. 10, no. 8, pp. 423–434, 1997.

[86] A. Tannús and M. Garwood, "Improved performance of frequency-swept pulses using offset-independent adiabaticity," *Journal of Magnetic Resonance*, vol. 120, pp. 133–137, 1996.

[87] A. Tannús and M. Garwood, "Adiabatic pulses," *NMR in Biomedicine*, vol. 10, no. 8, pp. 423–434, 1997.

[88] S. Conolly, J. Pauly, D. Nishimura, and A. Macovsiu, "Two-dimensional selective adiabatic pulses," *Magnetic Resonance in Medicine*, vol. 24, no. 2, pp. 302–313, 1992.

[89] A. Jang, N. Kobayashi, S. Moeller, J. Vaughan, J. Zhang, and M. Garwood, "2d pulses using spatially dependent frequency sweeping," *Magnetic Resonance in Medicine*, vol. 76, pp. 1364–1374, 2016.

[90] M. Mullen, N. Kobayashi, and M. Garwood, "Two-dimensional frequency-swept pulse with resilience to both $B_1$ and $B_0$ inhomogeneity," *Journal of Magnetic Resonance*, vol. 299, pp. 93–100, 2019.

[91] M. Mullen, N. Kobayashi, and M. Garwood, "Corrigendum to: 'two-dimensional frequency-swept pulse with resilience to both $B_1$ and $B_0$ inhomogeneity'," *Journal of Magnetic Resonance*, vol. In press, 2019.

[92] A. A. Maudsley, G. B. Matson, J. W. Hugg, and M. W. Weiner, "Reduced phase encoding in spectroscopic imaging," *Magnetic Resonance in Medicine*, vol. 31, no. 6, pp. 645–651, 1994.

[93] C. J. Hardy and P. A. Bottomley, "$^{31}$P spectroscopic localization using pinwheel nmr excitation pulses," *Magnetic Resonance in Medicine*, vol. 17, no. 2, pp. 315–327, 1991.

[94] L. Panych and K. Oshio, "Selection of high-definition 2d virtual profiles with multiple rf pulse excitations along interleaved echo-planar k-space trajectories," *Magnetic Resonance in Medicine*, vol. 41, pp. 224–229, 1999.

[95] M. Mullen, A. Gutierrez, N. Kobayashi, J. Haupt, and M. Garwood, "Accelerated imaging with segmented 2d pulses using parallel imaging and virtual coils," *Journal of Magnetic Resonance*, vol. 305, pp. 185–194, 2019.

[96] M. A. Griswold, P. M. Jakob, R. M. Heidemann, *et al.*, "Generalized auto-calibrating partially parallel acquisitions (grappa)," *Magnetic Resonance in Medicine*, vol. 47, no. 6, pp. 1202–1210, 2002.

[97] J. E. Power, M. Foroozandeh, R. W. Adams, *et al.*, "Increasing the quantitative bandwidth of nmr measurements," *Chem Commun (Camb)*, vol. 52, no. 14, pp. 2916–2919, 2016.

[98] K. E. Cano, M. A. Smith, and A. J. Shaka, "Adjustable, broadband, selective excitation with uniform phase," *Journal of Magnetic Resonance*, vol. 155, no. 1, pp. 131–139, 2002.

[99] M. Foroozandeh, M. Nilsson, and G. A. Morris, "Improved ultra-broadband chirp excitation," *Journal of Magnetic Resonance*, vol. 302, pp. 28–33, 2019.

[100] J. Hennig, A. M. Welz, G. Schultz, *et al.*, "Parallel imaging in non-bijective, curvilinear magnetic field gradients: A concept study," *Magnetic Resonance Materials in Physics, Biology and Medicine*, vol. 21, no. 1-2, pp. 5–14, 2008.

[101] C. Juchem, S. Umesh Rudrapatna, T. W. Nixon, and R. A. de Graaf, "Dynamic multi-coil technique (dynamite) shimming for echo-planar imaging of the human brain at 7 tesla," *NeuroImage*, vol. 105, pp. 462–472, 2015.

[102] M. Zaitsev, G. Schultz, J. Hennig, R. Gruetter, and D. Gallichan, "Parallel imaging with phase scrambling," *Magnetic Resonance in Medicine*, vol. 73, no. 4, pp. 1407–1419, 2015.

[103] G. Bodenhausen, R. Freeman, and J. Keeler, "Suppression of artifacts in two-dimensional j spectra," *Journal of Magnetic Resonance (1977)*, vol. 27, no. 3, pp. 511–514, 1977.

[104] T. Froelich, L. DelaBarre, P. Wang, J. Radder, E. Torres, and M. Garwood, "Fast spin echo approach for accelerated $B_1$-gradient based mri," *Magnetic Resonance in Medicine*, vol. 89, pp. 2204–2216, 2023.

[105] D. Canet, "Radiofrequency field gradient experiments," *Progress in Nuclear Magnetic Resonance Spectroscopy*, vol. 30, pp. 101–135, 1997.

[106] F. Casanova, H. Robert, J. Perlo, and D. Pusiol, "Echo-planar rotating-frame imaging," *Journal of Magnetic Resonance*, vol. 162, no. 2, pp. 396–401, 2003.

[107] D. I. Hoult, "Rotating frame zeugmatography," *Journal of Magnetic Resonance (1969)*, vol. 33, pp. 183–197, 1979.

[108] U. Katscher, J. Lisinski, and P. Börnert, "Rf encoding using a multielement parallel transmit system," *Magnetic Resonance in Medicine*, vol. 63, pp. 1463–1470, 2010.

[109] P. Maffei, P. Mutzenhardt, A. Retournard, *et al.*, "Nmr microscopy by radiofrequency field gradients," *Journal of Magnetic Resonance Series A*, vol. 107, no. 1, pp. 40–49, 1994.

[110] A. Trakic, J. Jin, E. Weber, and S. Crozier, "Model for $B_1$ imaging in mri using the rotating rf field," *Comput Math Methods Med*, vol. 2014, p. 461 647, 2014.

[111] M. Garwood, T. Schleich, B. D. Ross, G. B. Matson, and W. D. Winters, "A modified rotating frame experiment based on a fourier-series window function - application to invivo spatially localized nmr-spectroscopy," *Journal of Magnetic Resonance*, vol. 65, no. 2, pp. 239–251, 1985.

[112] C. A. Meriles, D. Sakellariou, and A. Pines, "Broadband phase modulation by adiabatic pulses," *Journal of Magnetic Resonance*, vol. 164, no. 1, pp. 177–81, 2003.

[113] E. Torres, T. Froelich, P. Wang, *et al.*, "$B_1$-gradient–based mri using frequency-modulated rabi-encoded echoes," *Magnetic Resonance in Medicine*, pp. 1–12, 2021.

[114] J. Hennig, A. Nauerth, and H. Friedburg, "Rare imaging - a fast imaging method for clinical mr," *Magnetic Resonance in Medicine*, vol. 3, no. 6, pp. 823–833, 1986.

[115] M. A. Griswold, P. M. Jakob, R. M. Heidemann, *et al.*, "Generalized autocalibrating partially parallel acquisitions (grappa)," *Magnetic Resonance in Medicine*, vol. 47, no. 6, pp. 1202–10, 2002.

[116] K. P. Pruessmann, M. Weiger, M. B. Scheidegger, and P. Boesiger, "Sense: Sensitivity encoding for fast mri," *Magnetic Resonance in Medicine*, vol. 42, no. 5, pp. 952–962, 1999.

[117] D. K. Sodickson and W. J. Manning, "Simultaneous acquisition of spatial harmonics (smash): Fast imaging with radiofrequency coil arrays," *Magnetic Resonance in Medicine*, vol. 38, no. 4, pp. 591–603, 1997.

[118] J. Bezanson, A. Edelman, S. Karpinski, and V. B. Shah, "Julia: A fresh approach to numerical computing," *SIAM Review*, vol. 59, no. 1, pp. 65–98, 2017.

[119] P. Hasgall, F. Di Gennaro, C. Baumgartner, *et al.*, "It'is database for thermal and electromagnetic parameters of biological tissues," 2022.

[120] M. MJ, V. ELG, T. A, and inventors, "Universidade de são paulo, assignee.espectrômetro para uso em sistemas de ressonância magnética e sistemas de ressonância magnética," *Brazil Software Registry No. BR102015000624-1.*, 2015.

[121] S. DMDD, P. DC, L. GV, V. ELG, M. MJ, and T. A, "Magnetic resonance system configuration and editing tools," In: Proceedings of The IUPESM World congress on Medical Physics and Biomedical Engineering, pp. 667–668.

[122] P. DC, S. DHT, F. M, and et al., "Pymr: A framework for programming magnetic resonance systems," *Brazil Software Registry No. BR512019001829-0*, 2017.

[123] D. Pizetta, "Pymr: A framework for programming magnetic resonance systems." Ph.D. dissertation, 2018.

[124] T. A, P. DC, S. DMDD, *et al.*, "Torm-ide—integrated development environment for magnetic resonance applications.," *Brazil Software Registry No. BR512015001484-6*, 2015.

[125] T. A, P. DC, S. DMDD, *et al.*, "Subsistema multiplataforma para controle de aquisição, visualização e organização de dados de espectrômetro digital de rm: Torm console," *Brazil Software Registry No. BR512015001485-4.*, 2015.

[126] C. H. Cunningham, J. M. Pauly, and K. S. Nayak, "Saturated double-angle method for rapid $B_1^+$ mapping," *Magnetic Resonance in Medicine*, vol. 55, no. 6, pp. 1326–33, 2006.

[127] T. Okuda, Y. Korogi, I. Ikushima, *et al.*, "Use of fluid-attenuated inversion recovery (flair) pulse sequences in perinatal hypoxic-ischaemic encephalopathy," *Br J Radiol*, vol. 71, no. 843, pp. 282–90, 1998.

[128] Q. Deng, S. B. King, V. Volotovskyy, B. Tomanek, and J. C. Sharp, "$B_1$ Transmit phase gradient coil for single-axis trase rf encoding," *Magnetic Resonance Imaging*, vol. 31, no. 6, pp. 891–9, 2013.

[129] H. Sun, A. AlZubaidi, A. Purchase, and J. C. Sharp, "A geometrically decoupled, twisted solenoid single-axis gradient coil set for trase," *Magnetic Resonance in Medicine*, vol. 83, no. 4, pp. 1484–1498, 2020.

[130] T. Froelich and M. Garwood, "Iterative model-based image reconstruction of rf gradient-based mri," in *Proc. Intl. Soc. Mag. Reson. Med. 30*, (London, UK), May 2022.

[131] J. A. Fessler, "Optimization methods for mr image reconstruction (long version)," 2019. arXiv: `1903.03510 [eess.IV]`.

[132] A. Gutierrez, M. Mullen, D. Xiao, *et al.*, "Reducing the complexity of model-based mri reconstructions via sparsification," *IEEE Transactions on Medical Imaging*, vol. 40, no. 9, pp. 2477–2486, 2021.

[133] S. Theilenberg, Y. Shang, J. Ghazouani, *et al.*, "Design and realization of a multi-coil array for $B_0$ field control in a compact 1.5 t head-only mri scanner," *Magnetic Resonance in Medicine*, vol. 90, no. 3, pp. 1228–1241, 2023.

[134] B. J. Parkinson, R. Slade, M. J. D. Mallett, and V. Chamritski, "Development of a cryogen free 1.5 t ybco hts magnet for mri," *IEEE Transactions on Applied Superconductivity*, vol. 23, no. 3, pp. 4 400 405–4 400 405, 2013. DOI: `10.1109/TASC.2012.2235893`.

[135] R. A. Slade, B. J. Parkinson, and R. M. Walsh, "Test results for a 1.5 t mri system utilizing a cryogen-free ybco magnet," *IEEE Transactions on Applied Superconductivity*, vol. 24, no. 3, pp. 1–5, 2014. DOI: `10.1109/TASC.2013.2283660`.

[136] B. Parkinson, "Design considerations and experimental results for mri systems using hts magnets," *Superconductor Science and Technology*, vol. 30, no. 1, p. 014 009, 2016. DOI: `10.1088/0953-2048/30/1/014009`.

[137] M. Mullen and M. Garwood, "Contemporary approaches to high-field magnetic resonance imaging with large field inhomogeneity," *Progress in Nuclear Magnetic Resonance Spectroscopy*, vol. 120-121, pp. 95–108, 2020.